# Study of Interface Plasmon in Low-dimensional Silicon Nanostructures

# 低維硅納米結構表界面等離激元之研究

WANG, Xiaojing

王笑靜

A Thesis Submitted in Partial Fulfillment
of the Requirements for the Degree of
Doctor of Philosophy
in
Physics

The Chinese University of Hong Kong
September 2010

UMI Number: 3483330

All rights reserved

INFORMATION TO ALL USERS
The quality of this reproduction is dependent upon the quality of the copy submitted.

In the unlikely event that the author did not send a complete manuscript
and there are missing pages, these will be noted. Also, if material had to be removed,
a note will indicate the deletion.

UMI 3483330
Copyright 2011 by ProQuest LLC.
All rights reserved. This edition of the work is protected against
unauthorized copying under Title 17, United States Code.

ProQuest LLC
789 East Eisenhower Parkway
P.O. Box 1346
Ann Arbor, MI 48106-1346

Thesis/Assessment Committee

Professor NG, Hang Leung Dickon (Chair)
Professor LI, Quan (Thesis Supervisor)
Professor WONG, King Young (Committee Member)
Professor DAI, Jiyan (External Examiner)

# Acknowledgement

During the period of this thesis study, I would like to dedicate my appreciation to my supervisor: Prof.Li Quan. Her guidance and scientific methodology leads me to the right way of the research and I am sure I will definitely benefit from the scientific training in her group for ever. I would like to thank the department of physics of the Chinese University of Hong Kong for giving the opportunity to make me study here. Thanks for Dr.Wang Juan and Dr.Jiao Yang for the academic help in the study. I also would like to appreciate the technicians in our Lab: Mr.Andrew Li and Mr.Yeung Man Hau. I also thank Prof.Duan Xiaofeng for the help when I study in CAS.

Thanks for all the friends I met here, I will always remember the time I spend with all of you. My family is always on my back no matter what situation I am in, I can not express my gratitude enough for my parents, brother and sister-in-law, and Ms.Wei Ze. Without you, I will never get to this point.

# Abstract

Surface/interface plasmons (SP/IP) are the plasmons confined at specific boundaries, describing the surface/interface charge density oscillation. They are generated when the scattered electromagnetic wave with its scattering vector component parallel to the boundary propagates along the surface/interface. Study of surface plasmon resonance in noble metals such as gold and silver nanoparticles have started decades ago, and recent interests are focused on the plasmonic properties of individual nanoparticles, as enabled by the size/shape control in the nanostructure growth and advances made in the characterization methodologies Besides the noble metals, semiconductor such as silicon also attracts much attention for its plasmonic behavior. The surface/interface plasmon resonance frequency of Si-based nanostructures occurs at relatively higher energies (compared to Au and Ag), making it a perfect system to be studied using electron energy loss spectroscopy (EELS) based techniques. When performed in a scanning transmission electron microscope (STEM), such a technique enjoys excellent spatial resolution, and can map the local plasmonic properties of individual nanostructures.

The plasmon excitation depends sensitively on not only the material dielectric properties but also the geometrical configurations of the material. In the present thesis

work, silicon-based nanostructures with planar, spherical, and cylindrical boundaries were investigated using both experimental and theoretical approaches, with focus on the plasmon oscillation originating from the Si/$SiO_2$ interface. The specimens employed include silicon/silica thin films, Si-core/$SiO_2$-shell nanoparticles with different aspect ratios and spherical-shaped nanoparticle chains, as well as Si-core/$SiO_2$-shell nanocables.

In this thesis study, the surface/interface plasmon excitations in different Si nanostructures were revealed through the EELS study in TEM/STEM. In the case of the planar boundary such as the wedge-like specimen, the spatially resolved EELS results disclose the dependence of the intensity and the position of the interface plasmon peak on the sample thickness. In the case of the Si-core/ $SiO_2$-shell nanoparticles, we found that the SP/IP peak will firstly red-shifts with the increase of the $SiO_2$ shell thickness and eventually levels off . As the aspect ratio of the Si nanoparticles increases, (from spherical particle to nanorod and nanowire), the SP/IP will split into two branches: transverse and longitudinal modes. We also found the intensity ratio of the transverse/longitudinal mode excitations depends on the diameter of the Si core size in the nanostructures. In the one-dimensional interacting Si nanoparticle chains, the Si nanoparticles were embedded in the $SiO_2$ shell, the splitting of the SP excitation into transverse and longitudinal modes was also observed. As the inter-particle distance reduces to several nanometers, the coupling of the IP excitation between the adjacent particles becomes significant, and results in the local field enhancement in-between the two particles. This is directly visualized using EFTEM imaging in TEM/STEM.

# 摘要

在過去的數年中，納米結構中的電學性質研究吸引了眾多注意力，這是因爲納米尺度內的性質和傳統體材料的性質已經大不相同。等離子震蕩描述材料內弱束縛的電子的集體行爲，這種震蕩的量子化定義爲等離激元。對于等離激元的學習能夠理解材料豐富的電子性質。等離激元可以由兩種方式激發：高能電子或光子。

表面/界面等離激元是局限在特定邊界范圍的等離激元，可以通過表面/界面電荷密度的震蕩來描述。其產生于當散射的電子波的波矢量具有平行于邊界傳播的分量時。對于貴金屬如金和銀的表面等離激元研究已經持續了幾十年，除了金和銀，半導體例如硅因爲其等離子特性也吸引了研究者的目光。 特別是，近年在硅納米材料的制備上的進展使得詳細研究硅納米結構的等離激元特性成爲可能，這些制備技術在形貌、尺寸和組分控制上均有重要進步。然而，和金銀相比，硅材料相對較高的表面/界面等離激元共振頻率使得利用傳統光學方法開展研究非常困難。基于此考慮，在掃描透射電子顯微鏡中進行的電子能量損失譜實驗是一種優秀的替代方法，因爲這種方法不但具有非常寬的能量探測范圍，而且擁有非常良好的空間分辨率。

等離子激發不但對于材料本身的介電性質非常敏感，而且對于幾何形狀也很敏感。在本論文學習中，基于硅材料的納米結構，例如擁有平面邊界，球型邊界，柱形邊界的結構通過實驗和理論進行了研究。我們著眼于硅和二氧化硅系統的表面/界面等離激元激發。實驗中用到的樣品包括硅/二氧化硅薄膜，殼層納米顆粒，納

米線，納米顆粒組成的鏈式結構等。

實驗中用到了裝備有 Gatan 電子能量損失譜儀的掃描透射電子顯微鏡。 空間分辨的電子能量損失譜用來闡釋電子作用距離，樣品尺寸和幾何形狀如何影響硅/二氧化硅系統的等離激元激發與震蕩。數值模擬也用來佐證以上因素如何影響。因爲掃描透射電子顯微鏡中電子入射速度接近光速，電磁場的遲滯效應可能會帶來實驗測量值和計算值的偏差。 因此在當系統尺寸大或入射電子能量高時，計算中可能需要考慮到這種效應。在一些結構中，考慮/不考慮相對論修正的計算結果的比較也說明了這種遲滯效應。

# Table of Contents

**Chapter 1. Introduction** **6**

**Chapter 2. Background: Interface Plasmon in Nanostructured Materials Excited by Fast Electrons** **10**

2.1 Classical dielectric theory 11

2.1.1 Dielectric function of Si 11

2.1.2 Dielectric theory of the material excited by fast electrons 12

2.2 Plasmonic properties studied using optical means and electron energy loss spectroscopy 17

2.2.1 Optical Method 17

2.2.2 EELS method 19

2.3 Research Status of SP/IP excitation in different Si nanostructures 20

**Chapter 3. Instrumentation : TEM/STEM and EELS** **23**

3.1 The conventional/scanning transmission electron microscope 24

3.1.1 Conventional TEM 24

3.1.2 Scanning TEM 27

3.2 Electron energy loss spectroscopy 31

3.2.1 EEL spectrometer 31

3.2.2 Spatially resolved EELS 32

3.2.3 Energy Filtered TEM 35

**Chapter 4. Interface plasmon excited on planar Si/SiO2 interfaces** **38**

4.1 Experimental results 38

4.1.1 Spectrum recording mode 38

4.1.2 General features in the spectrum taken at the imaging mode 39

4.1.3. Spatially resolved EELS taken at the Si/SiO2 interface 41

4.1.4 Thickness dependence of the plasmon oscillations 44

4.2 Simulation results 48

4.2.1 The simulation model 48

4.2.2 Non-relativistic consideration with zero impact parameter 50

4.2.3 Non-relativistic consideration with different impact parameter 51

4.2.4 Relativistic consideration with different impact parameter 52

4.2.5 Comparison between experimental and simulated results as a function of the impact parameter 55

4.3 Conclusion 56

**Chapter 5. Size Effect on the Interface Plasmon of Si/SiO2 Nanostructures 58**

5.1 General spectrum features of the Si/SiO2 core/shell nanoparticles 58

5.2 Effect of the Si core diameter on the interface plasmon oscillation 60

5.2.1 Experimental EELS results from core/shell nanoparticles with different Si core size 60

5.2.2 The simulation model 62

5.2.3 Relativistic criteria for Si nanoparticle 64

5.2.4 Simulation results and discussion 68

5.3 Effect of the SiO2 shell thickness on the interface plasmon oscillation 72

5.3.1 Experimental results 72

5.3.2 Simulation results and comparison with experimental ones 74

5.4 Conclusion 76

**Chapter 6. Interface Plasmon Excitation in Si/SiO2 Core/Shell Nanostructures with Different Geometrical Configurations 78**

6.1 The evolution of EEL spectra in the Si/SiO2 core/shell nanostructures 79

6.1.1 Comparison of the general features in EEL spectra between different nanostructures 79

6.1.2 Longitudinal mode and transverse mode 82

6.1.3 The evolution of EEL spectra as a function of aspect ratio and retardation effect 86

6.1.4 Spatial distribution of the SP/IP excitation with different aspect ratio 89

6.2 Interface plasmon oscillation in Si/SiO2 core-shell nanocables of different diameter 91

6.2.1 General features in EEL spectrum for Si/SiO2 nanocable 92
6.2.2 Experimental EELS results with different Si core size 93
6.2.3 Simulation results with different Si core size 94
6.3 Optical absorption properties of the Si nanostructures of different geometrical configuration—from nanoparticle to nanocable of small and large diameters 95
6.4 Conclusion and discussion 97
**Chapter 7. Interface Plasmon in Interacting Si Nanoparticle Chains 98**
7.1 Sample preparation and experimental setup 99
7.2 EEL spectrum in the Si chain nanostructures with different particle distances 100
7.3 Spatial distribution of the SP/IP excitations in the Si nanoparticle chains 108
7.4 Absorption property of the nanoparticle chain 112
7.5 Conclusions 113
**Chapter 8. Conclusion 115**
**Bibliography 118**

# Chapter 1. Introduction

The plasma oscillation is collective excitation of the weakly bonded electrons in the material, and the oscillation can be excited either by photons or high energy electrons passing by the material[1,2]. The resonance frequency of this plasmon is directly related to the density of states of free (weakly bounded) electrons in the solid. Therefore, study of the plasmonic properties provides abundant information on the electronic properties of the materials.

For an ideal case when material electrons can move freely, the system can be treated as electron gas. This is best represented by metal such as aluminum [3], in which the outer shell electrons can be considered as free electrons. Considering excitation by high energy electrons, when fast electrons pass through a thin metal foil, the apparent feature is caused by the plasmon oscillations in low energy loss region, which can be revealed by the electron energy loss spectrum (EELS)[4]. Besides the volume plasmon, surface/interface plasmons[5] refer to the plasmons confined at specific boundaries, describing the surface/interface charge density oscillation. They are generated when the scattered electromagnetic wave with its scattering vector component parallel to the boundary propagates along the surface/interface [6].

The plasmonics in metal has been investigated intensely under the framework of classical dielectric description [7-10], in which the Drude model was employed to describe the dielectric response of the solid. Mie theory[11] has been widely applied to calculate the inelastic scattering in small spherical particles, giving analytical solutions to the Maxwell's equations for the scattering of electromagnetic radiation. It was then extended to the configuration with cylindrical boundaries[12] .For semiconductors, the oscillation can be treated similarly to that in a metal—the valence electrons are considered as weakly bounded electrons, contributing to the generation of plasma oscillations when excited collectively by the external field[1]. Study of surface plasmon resonance in noble metals such as gold and silver nanoparticles[13-15] can be dated back to decades ago. Besides the noble metals, semiconductor such as Si also attracts much attention for its plasmonic behavior[16-17]. However, the relative higher surface/interface plasmon resonance frequency of Si-based nanostructures (when compared to Au and Ag) makes it rather difficult to be studied using conventional optical means. This is the reason why there is rare work done on the system of Si nanostructures in different geometrical configurations in previous years. While recent progress on the shape, size and composition controlled silicon nanostructures fabrication [18-20] make it possible to study their plasmonic properties in great detail. Electron energy loss spectroscopy (EELS) [4] performed in scanning transmission electron microscope (STEM) [24,25] provide a unique opportunity to study the plasmonic properties of Si-based nanostructures, due to its wide energy detection range, and more importantly, the excellent spatial resolution

that enables the very localized property investigation.

The objective of this thesis is to understand the surface/interface plasmon in different Si/SiO2 nanostructures, such as planar boundary in thin films, spherical boundaries in nanoparticles, cylindrical boundary in nanowires and nanorods, and interacting nanoparticle chains. We start from an introduction of fundamental dielectric theory to describe the Plasmon oscillation in chapter 2, in which the adopted simulation methodology is also explained. Chapter 3 illustrated the experimental apparatus and methodology. The experimental techniques used in the thesis study involve EELS in STEM, in particular, spatially resolved EELS and energy filtered imaging, all of which enable the study of surface/interface plasmon excitations in individual Si nanostructures.

In Chapter 4 the planar boundary was studied by using a wedge-like specimen. The dependence of the SP/IP on the thickness of the specimen was investigated experimentally. We found that relativistic effect should be considered in interpreting the experimental results. In Chapter 5, we move to Si/$SiO_2$ core/shell nanostructures with spherical interfaces. The EELS reveals a red-shift of the IP energy when the $SiO_2$ shell thickness increases. In Chapter 6, we increase the aspect ratio of the Si nanostructures from spherical particle to nanorods and eventually long nanowires. We have found the splitting of the IP into transverse and longitudinal mode when the aspect ratio of the Si nanostructure deviates from 1. Direct visualization of the IP distribution in different nanostructures is realized using EFTEM imaging. Based on

the understanding obtained in chapter 6, we further investigated the plasmonic properties in interacting Si nanoparticle chains in chapter 7. Strong coupling along the chain axial direction is visualized when the interparticle separation reduces to several nanometers. At last, a summary is given in the chapter 8.

# Chapter 2. Background: Interface Plasmon in Nanostructured Materials Excited by Fast Electrons

The description of the polarization response of the medium to the external field is usually characterized by a dielectric function $\varepsilon(\omega.q)$ , which is a function of frequency and wave vector.[2,6,25]. The dielectric function affects the physical properties of the solids significantly, such as the absorption and scattering. Therefore, one can deduce/understand the plasmonic properties of the materials by obtaining a good knowledge of its dielectric function. In this regard, we first introduce, in this chapter, the dielectric function of Si, followed by the classical dielectric response theory expressed in terms of the dielectric function of the material.

The dielectric response of a piece of material can be obtained by many means. Conventionally, optical methods can be used [29]. On the other hand, when the material is exposed to the fast electrons in an electron microscope, inelastic scattering will occur. The electrons of the material will be excited under the external electrical field, and the incident electrons will suffer from energy loss accordingly. By analyzing the profile of the energy lost electrons, one can also obtain the dielectric response of the

materials. As plasmon refers to the collective oscillation of free (weakly bounded) material electrons, such information is contained in the dielectric function of the material. We will compare the material plasmon oscillation excited by electrons to that excited by optical means in this chapter. The advantages of the electron excitation in this study will be discussed. Finally the research status of the surface/interface plasmon excitation in Si nanostructures will be illustrated.

## 2.1 classical dielectric theory

### 2.1.1 dielectric function of Si

As indicated before the dielectric function of the material depends on both the frequency $\omega$ and the wavevector $q$. The $q$ dependence of the dielectric function labels the dispersion characteristic of the dielectric medium. The calculation of $\varepsilon(\omega,q)$ of a Fermi gas described that the external perturbation leads to the interband transitions and change the electron state of the Fermi gas from the energy level $E_k$ to $E_{k+q}$ [28]. In this process the momentum $\hbar q$ is transferred. In this thesis, the local response approximation for homogeneous medium is adopted, thus the dispersion character is ignored. It means the dielectric function $\varepsilon(\omega,q)$ can be simplified to a spatially local response. Here $\varepsilon(\omega,r-r')=\delta(r-r')\varepsilon(\omega)$ and $\varepsilon(\omega)$ is independent on the wave vector, $r$ and $r'$ are the displacement of the source and filed point. Such conclusion is valid at optical frequency range [85].

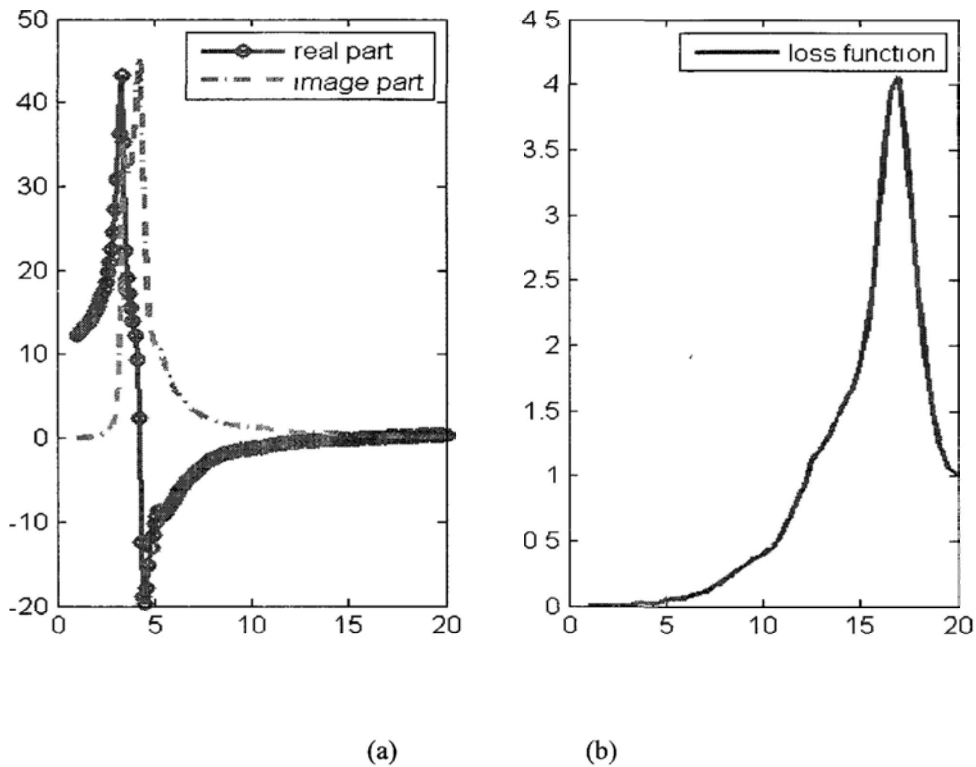


(a) (b)

Fig.1 (a)dielectric function and (b) loss function of Si

The dielectric function of Si[29] is shown in Fig.1. In Fig.1(a), real part and imaginary part are plotted respectively. In Fig.1(b), the loss function $-\mathrm{Im}[1/\varepsilon]$ [4] calculated from Fig.1(a) is given as well. In general, the dielectric function of material is complex valued functions of angular frequency. The real part is considered to contribute to the polarization of the material under the external field, the imaginary part determines the amount of absorption by the material[3].

### 2.1.2 dielectric theory of the material excited by fast electrons

The object of the dielectric response theory is to form quantitative description of a dielectric system under the influence of the external field. Under the assumptions of

classical dielectric response theory, the incident electron is defined as a particle following a fixed path, and the path will not be affected by the interaction between the incident electron and the dielectric medium. Secondly, only one electron interacts with the medium at one time, no successive incident electron will be involved into the interaction. In the field emission STEM, the validity of these approximations were proved and the spectrum can be obtained by convolution of the loss probability with the point distribution function (determined by the size of the probe and the spectrometer response function), if necessary[25].

Under the local dielectric response, and in a homogeneous medium the Maxwell's equation can be written as[6]:

$$\nabla \times \tilde{E}(r,t) = -\frac{\partial \tilde{B}(r,t)}{\partial t} \quad (2.1a)$$

$$\nabla \times \tilde{H}(r,t) = \tilde{J}(r,t) + \frac{\partial \tilde{D}(r,t)}{\partial t} \quad (2.1b)$$

$$\nabla \cdot \tilde{D}(r,t) = \tilde{\rho}(r,t) \quad (2.1c)$$

$$\nabla \cdot \tilde{B}(r,t) = 0 \quad (2.1d)$$

The transformation is introduced between time dependent and frequency dependent quantities:

$$A(r,\omega) = \int_{-\infty}^{\infty} dt \exp(i\omega t)\tilde{A}(r,t) \quad \text{and} \quad \tilde{A}(r,t) = \int_{-\infty}^{\infty} d\omega \exp(-i\omega t) A(r,\omega) \quad (2.2)$$

Thus the Maxwell's equations are rewritten as:

$$\nabla \times E(r,\omega) = i\omega B(r,\omega) \quad (2.3a)$$

$$\nabla \times H(r,\omega) = J(r,\omega) - i\omega D(r,\omega) \quad (2.3b)$$

$$\nabla \cdot D(r,t) = \rho(r,\omega) \quad (2.3c)$$

$$\nabla \cdot B(r,\omega) = 0 \quad (2.3d)$$

To decouple the electric and magnetic field the Hertz vector $\tilde{\Pi}(r,\omega)$ [6] is introduced. The question is then transformed to finding the solution of the Hertz vector:

$$[\nabla^2 + \frac{\varepsilon\omega^2}{c^2}]\tilde{\Pi}(r,\omega) = \frac{1}{i\omega\varepsilon(\omega)\varepsilon_0} J(r,\omega) \quad (2.4)$$

The solution of the Hertz vector can be divided into two parts: $\tilde{\Pi}_e(r,\omega)$ is due to the field generated by the moving electron itself, $\tilde{\Pi}_i(r,\omega)$ is due to the field produced by the induced charges. The electric field can be solved in terms of the solution to the Hertz vector $\tilde{\Pi}_i(r,\omega)$, thus the electron energy loss produced by the potential of the induced charge can be obtained. The result can be expressed as:

$$\Delta E = \frac{e}{2\pi} \int_{-\infty}^{\infty} dz \int_{-\infty}^{\infty} d\omega \exp(-i\omega z / v)[\frac{\partial}{\partial z}(V_i(r,\omega))] \quad (2.5)$$

in which $V_i(r,\omega)$ indicates the induced part of the solution of the electric potential. The total energy loss is related to the probability by

$$\Delta E = \int_0^\infty d\omega \hbar\omega \frac{dP(\omega)}{d\omega} \quad (2.6)$$

From equation (2.6) the loss probability can be obtained finally. Therefore the calculation of the spectrum is actually to find the solution of the electrostatic potential for an electron located in the dielectric medium. The theory has been applied to the particle geometries [17,30,31] and has been proved to be identical to the method of solving the screen interaction under the self-energy formalism [32,33].

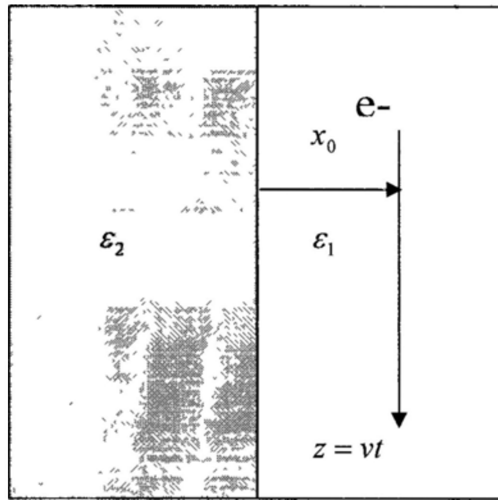


Fig.2 schematic description of the interface of planar boundary

Now we are taking one example considering the interface between two dielectric material with the dielectric functions $\varepsilon_1$ and $\varepsilon_2$, in a planar boundary configuration shown in Fig.2. The extended case such as spherical configuration, cylindrical configuration and interacting particle chain configurations, will be discussed in Chapter 5-7. In the Fig.2 $x_0$ is the distance between the trajectory of the electron and the interface, this value is defined as the impact parameter. We make the assumption that the electrons incident parallel to the interface of the two materials. The interface is along the *y-z* plane and the *z* direction is defined as the same as the incident

electrons'.

In the interface, the transform of the Hertz vector as functions of the wavevector along the interface ($q_y$ and $q_z$ ) is introduced[86]:

$$\tilde{\Pi}(r,\omega)=\int dq_y \int dq_z \exp[2\pi i(q_y y+q_z z)]\Pi(x,q_y,q_z,\omega) \qquad (2.7)$$

After the Hertz vector is obtained, the induced potential $V_t(r,\omega)$ can be solved by using the method introduced above. The solution can be substituted into equation (2.5) and the differential excitation probability under the non-relativistic limit can be expressed as :

$$\frac{d^2P}{d\omega dz}\approx\frac{e^2}{2\pi^2\varepsilon_0\hbar v^2}\{\mathrm{Im}\{-\frac{1}{\varepsilon_1}\}\{\ln(2\pi q_c v/\omega)-K_0(2\omega x_0/v)+\mathrm{Im}\{-\frac{2}{\varepsilon_1+\varepsilon_2}\}K_0(2\omega x_0/v) \qquad (2.8)$$

The volume plasmon term related to $\mathrm{Im}\{-1/\varepsilon_1\}$ and interface excitation related to $\mathrm{Im}\{-2/(\varepsilon_1+\varepsilon_2)\}$ appear at the same time. It means the dielectric function of the materials in both sides of the interface contribute to the interface plasmon excitation. The boundary condition required that the continuity of the tangential components of $E$ and $H$ parallel to the interface at the boundary must be satisfied. By considering the direction of the vector, $\varepsilon_1 E_1=-\varepsilon_2 E_2$ can be obtained. Therefore, the interface plasmon is characterized by $\varepsilon_1+\varepsilon_2=0$ under the situation of this semi-infinite planar boundary.

## 2.2 Plasmonic properties studied using optical means and electron energy loss spectroscopy

When the size of the material is decreased into nanometer scale, the size and the dimensionality confinement may influence the electromagnetic and optical properties of the material significantly.

The surface/interface plasmon can be excited by both electrons and photons, thus both optical and electron-based measurement can be used to obtain the material plasmonic properties. After Ritchie proposed the concept of surface plasmon in 1957, the optical method has long been the powerful technique to characterize and investigate the plasmonics properties[37].

### 2.2.1 Optical Method

In the noble metal particles, strong light absorption and scattering and great local-field enhancements occur at the plasmon frequency. The extinction can be directly observed though dark-field illumination scattering spectroscopy[87-89]. The dark-field spectroscopic technique allows us to record single-cluster spectra with little background.

1. The advantages of the optical method is as following:

The halogen or xenon lamp is used in the dark field optical method, and the specimen is immersed in the solution. Therefore the requirement of vacuum is not as

restrict as in electron related techniques, thus the vacuum instruments may be not necessary in this technique.

The extinction of the noble metal can be visualized conveniently in the range of visible spectrum. The requirement of the sample is relatively less strict than that in an electron microscope.

The depth of field in a microscope is a variable to describe for how long the image of the object we are observing remains sharp along the optical axial direction. The optical method can easily achieve the much larger depth of filed ranges around hundreds of nanometers compared with the EELS method in a TEM/STEM. That means in the large magnification the specimen can be observed more easily in optical method.

2. The disadvantages are:

In the optical microscopy the spatial resolution is in the order of the wavelength or sub-wavelength due to the diffraction limit. When the size of the noble metal particles or clusters are in the range of hundreds of nanometers the optical experiments can be done. As the specimen become smaller, the much more localized information need to be acquired thus the optical method may limit its application in the nanometer scale. Furthermore in the optical illumination the higher order multipole mode will play less important role compared with the electron excitation. The reason is that the dipole excitation is considered as making dominant contribution

within the optical range.

### 2.2.2 EELS method

Similar to the optical excitations, the electron excitation process includes the illumination, interaction between the specimen and the incident electron, and the spectrum collection. Compared with the diffraction limit in the optical experiments (around hundreds of nanometers), the powerful technique of electron microscope allows one to study the electronic structures of the surface/interface of the materials in nanometer scale. By analyzing the EEL spectra, we can obtain information of the plasmonic properties in the vicinity of the surface/interface in the solid.

1. The advantages are:

The spatial resolution of EELS in the TEM/STEM depends on the electron beam size, the delocalization distance and the beam broadening[91]. The delocalization distance in the low loss region is in the range of a couple of nanometers when a 200 kV acceleration voltage is applied in TEM/STEM. Although the electron probe size can be confined to the order of angstroms, the obtained information is coming from the averaged area larger than the probe size. Nonetheless the spatial resolution of the EELS in TEM/STEM can still be restricted to the nanometer scale, this is superior to the optical ones.

Secondly, the diffraction pattern can be obtained in the TEM/STEM, thus the crystallography of the specimen can be analyzed at real time.

Furthermore the spectrometer attached to the TEM can provide the spectrum of the small interested area with large energy range to tens of of eV with the energy resolution limited within 1 eV.

2. The disadvantages are:

The disadvantage is that the requirement of the specimen will be strict. The depth of field is very short compared with optical ones, it can be improved limitedly by using smaller electron entrance aperture but at the cost of illumination decrease in imaging.

### 2.3 Research Status of SP/IP excitation in different Si nanostructures

In the early years a lot of work was developed to explore the plasmonic properties in noble metal [13-15,38,39]. While the research on the Si-based structures is limited by the specimen synthesis and conventional optical-based experimental technique. In recent years more attractions was drawn on the plasmonic properties of the Si nanostructures. One reason is the breakthrough of the synthesis of the Si nanostructures with different geometries, the other one is the convenience of the application of EELS related technique in TEM/STEM. In this section we will review the research status of surface/interface plasmon excitation based on the Si nanostructures.

In the early research work done by Ugarte, Colliex, Reed, Howie etc. [17-19,45-46], STEM and EELS experiments were performed on different Si nanostructures. The

geometries of the specimen included nanospheres, filaments in nanometer scale (nanowires), multilayer of $Si/SiO_2$ stacks and clusters of nanospheres. In the nanoparticles, Ugarte and Colliex etc. found that there exist two apparent excitation modes below the energy of bulk plasmon of Si. They attributed the lower energy branch to the incompletely oxidized silica layer. But it was latterly proved that the incompletely oxidized layer is not likely thus the physical nature of the lower energy feature remains unclear. When the particle was elongated to the cylindrical configuration, such as Si tips or filaments, Reed etc. found the similar two branches in the EELS as well. The sharp lower energy feature was identified and considered as the interband transitions in Si. Nevertheless, as such a feature is not always observed in any Si nanostructures, the explanation of interface transition seems problematic.

Furthermore, the plasmon coupling in the structure of multi-layers and multiple particles (aggregates) were investigated as well [47-50]. It was stated from Batson's experiment that besides the expected bulk and surface plasmon features the coupling appeared when the adjacent spheres were in close contact.

The SP/IP excitation probability has been theoretically studied and calculated in nanoparticle, nanowire and planar boundary by Abajo, Ferrel, Echnique, etc.[51-53] under the classic dielectric theory. The relativistic correction was considered in planar boundary and particle configuration and clusters[32,54-56]. The calculation quantitatively explained the surface/interface plasmon excitation in the planar, spherical and cylindrical geometries. Also the coupling of the SP/IP modes is

discussed in the references [57-61] by employing the model of double particle system. From the calculation results the multipole modes can be excited and result in lower energy branch and higher energy branch. Moreover the quantum approach, anisotropic excitation response surface exciton polaritons coupling, are developed in the reference[62-64]. The results indicated that the quantum approach will give the identical results as the ones under the classical description, providing the target of the silicon is not so small (1-2 nm) . All of the work constituted the background of the research on the plasmonics properties of Si nanostructure. In the following chapters we will investigate and discuss the plasmonic properties in the corresponding Si nanostructures in more detail.

# Chapter 3. Instrumentation : TEM/STEM and EELS

EELS is the analysis of the profile of the primary electrons as a function of energy loss, after they interact with the specimen. A detailed study of the valence electron excitation by EELS can provide substantial information of the material, for example the band gap, the interband transition and the plasmon oscillation . It is a powerful technique in exploring the nature of the surface/interface plasmons down to the nanometer scale. At small sizes, the geometrical shape and configurations of the material can affect the distribution of the surface/interface charges significantly, which are induced by the incident electrons.

In studying the surface/interface plasmon excitation in Si nanostructures, the mainly used instrument include the EEL spectrometer in a TEM/STEM to collect the EEL spectrum after the specimen interacted with the incident fast electron, the Gatan Image Filter is used to record the Energy Filtered TEM (EFTEM) image[4,24]. In this chapter we will briefly introduce the corresponding instruments and the working mode used in our experiments.

### 3.1 The conventional/scanning transmission electron microscope

### 3.1.1 Conventional TEM

The basic concept of TEM is similar to the optical microscope. The microscope can be divided into 3 main parts in general: the illumination system (source and condenser lens), lens system and imaging system.

The electrons are produced from the field emission gun (FEG) or the tungsten filament. Then the electrons go through the illumination system (condenser lenses) and objective lenses, followed by the interaction with the specimen. After the electrons passing intermediate lenses and projective lenses, the image of the specimen or the diffraction pattern can be observed in the imaging mode or in the diffracting mode. In this section more detail will be introduced about the illumination system and the diffraction mode and imaging mode in a TEM .

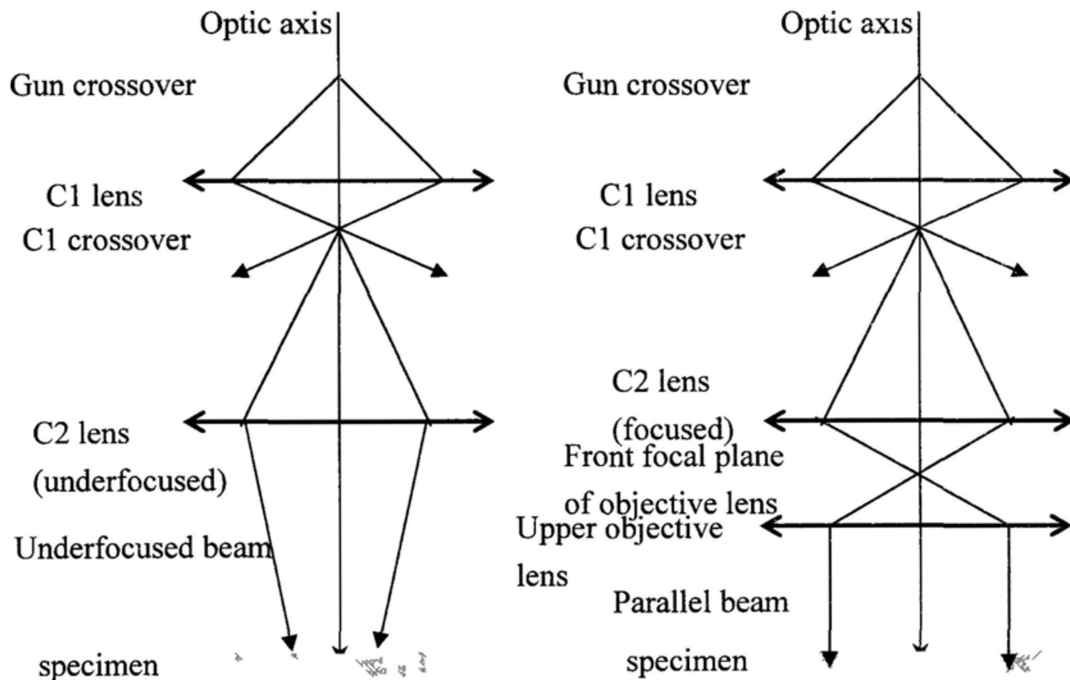


Fig.1 illumination system in TEM

In the specimen illumination system, converged beam and parallel beam mode are presented in the figure 1. The electromagnetic lenses are plotted in form of conventional lenses, and C1 and C2 are labeled for the condenser lens in use. In order to reduce the beam damage due to the converged beam, parallel beam illumination can be adopted in practical experiments at the cost of image intensity.

The objective lens and sample stage is the most important part in the TEM. The sample stage is used to clamp the specimen holder in the correct position so that the objective lens can form images or diffraction patterns in a reproducible way. The sample stage is usually combined with controllable mechanical part which can adjust the specimen position. The initial stage position should be close to the symmetrical plane between the upper and lower objective pole pieces, that is also the eucentric plane of the microscope. If the specimen is put on this plane, a point on the optic axis does not move laterally when it is tilted around the holder axis. Furthermore, the objective lens current is in an optimum value in this configuration.

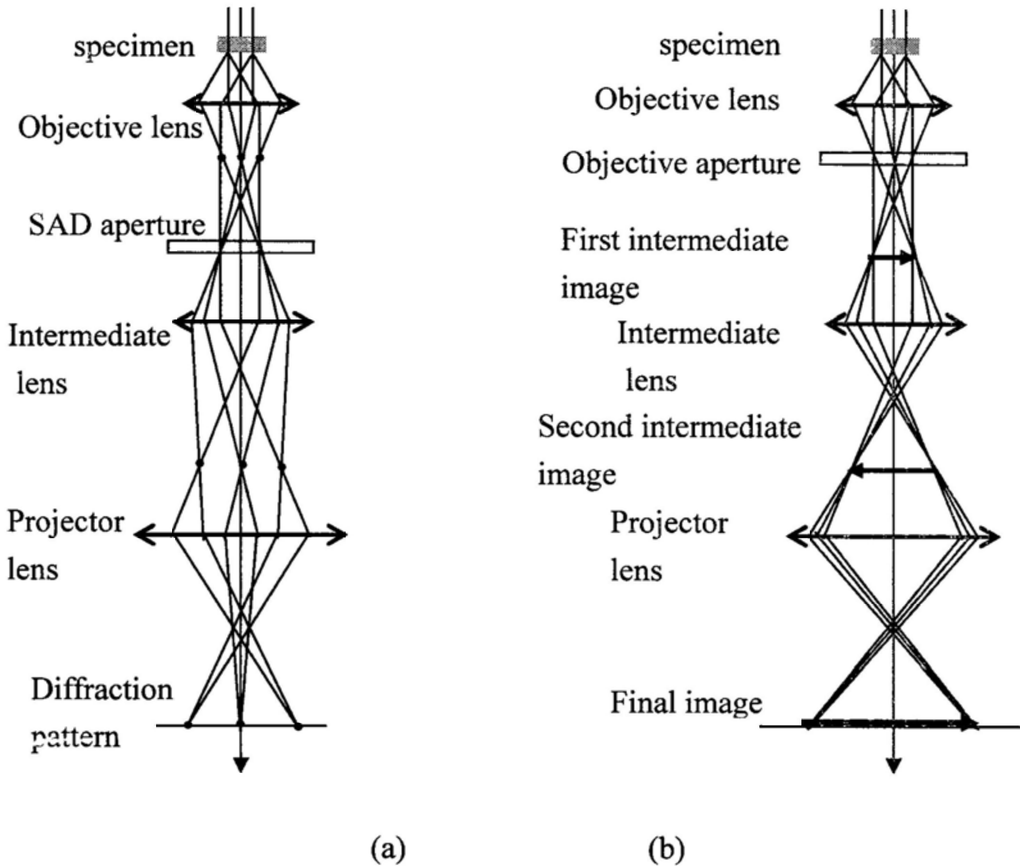


Fig.2 (a) imaging mode and (b) diffracting mode

The objective lenses collect the electrons exit the back surface of the specimen, creating diffraction patterns in the back focal plane or image in the image plane. The working principles of these two modes are illustrated in Fig.2. The diffraction mode and image mode can be summarized into the fundamental operations as below: to see the diffraction pattern one have to adjust the imaging system lenses so that the back focal plane of the objective lens acts as the object plane for the intermediate lens, then the diffraction pattern is projected onto the viewing screen, shown in Fig.2(a); if one want to look at an image, one can readjust the intermediate lens so that its object plane is the image plane of the objective lens, then the image is projected onto the viewing screen, shown in Fig.2(b). If the beam is converged at the specimen, the

diffraction pattern will spread into disks instead of sharply defined points. Thus the alternative way to obtain diffraction pattern with parallel beam illumination, the selecting area aperture is used. [24]

The Selected Area Diffraction (SAD) pattern contains a bright central spot (contributed mainly by the primary electrons) and diffraction spots (contributed by the elastically scattered electrons that satisfy the Bragg conditions). When we want to obtain the images of the specimen in a TEM, either the central spot or diffraction spots can be used. Inserting an objective aperture into the back focal plane of the objective lens can block out most of the electrons except those pass through the aperture As a result of this, the bright field image will be formed if the center spot is chosen, or the dark field image will be formed if a specific diffraction spot is selected.

### 3.1.2 Scanning TEM

Scanning transmission electron microscope incorporate the deflection scan coils into the conventional TEM column. When the incident electron beam is scanning over the specimen, the recording of the information can be realized in a point by point manner. This serial processing mode of the signal recording is different from the parallel one in the conventional TEM[24].

Based on the reciprocity relationship [90], the STEM and conventional TEM imaging systems are equivalent. It means when we consider each point of a finite source and each point of a detector separately, it can be confirmed that the image in a

STEM is the same as that in a conventional TEM. In the specimen plane, the objective lens in STEM produce the demagnification of the electron source (FEG) to form the fine probe with small diameter. The deflection coils serve to scan the electron probe over the specimen. While in the electronic optics, the key feature is the scanning beam must not change directions as the beam is scanned.

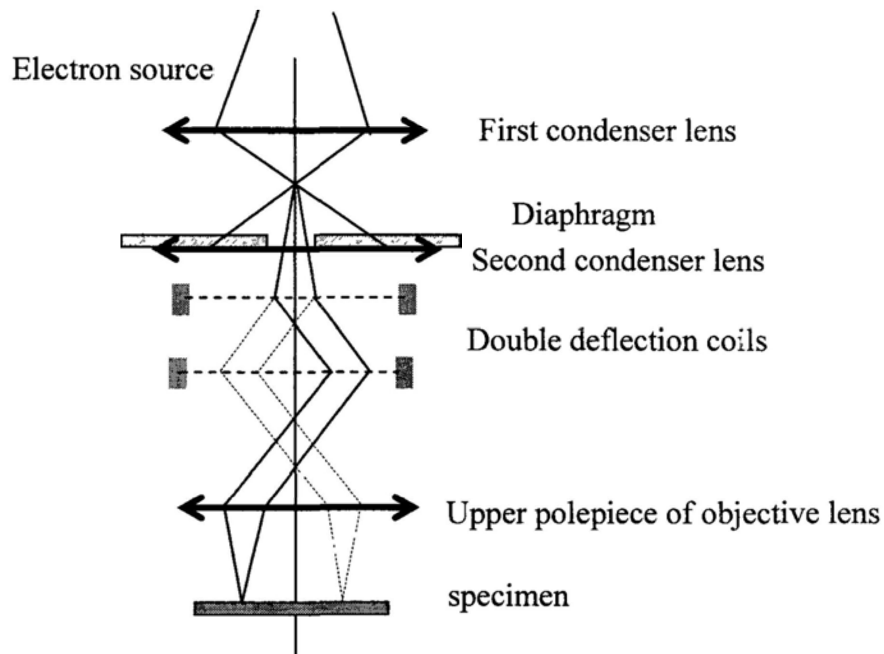


Fig.3 scanning of the convergent beam for STEM image formation

As shown in Fig.3, two pairs of scan coils are sued to pivot beam about the front focal plane of the upper objective polepiece. The lens then ensures that all electrons emerging from the pivot point are brought parallel to the optic axis and an image of the C1 lens crossover is formed in the specimen plane. If the objective lens is symmetrical, a stationary diffraction pattern is formed in the back focal plane. One advantage of this is that the defects in imaging lenses do not affect the image because

they are turned off during the imaging process. Thus the chromatic aberration is absent in STEM images.

The bright field (BF) image and dark field (DF) image will be formed by using central electrons or scattered electrons, which is similar to the conventional TEM. In general to get reasonable intensity in a STEM BF image in reasonable time, large intensity beam will be used thus the resolution will be poorer than TEM for good thin specimens. The DF image in conventional TEM is usually formed by allowing a fraction of the scattered electrons to enter the objective aperture, while the DF image in STEM are formed by collecting most of the scattered electrons on the Annular Dark Field (ADF) detector. Thus ADF images in STEM are less noisy than the DF images in conventional TEM, and the contrast is also greater than the ones in conventional TEM.

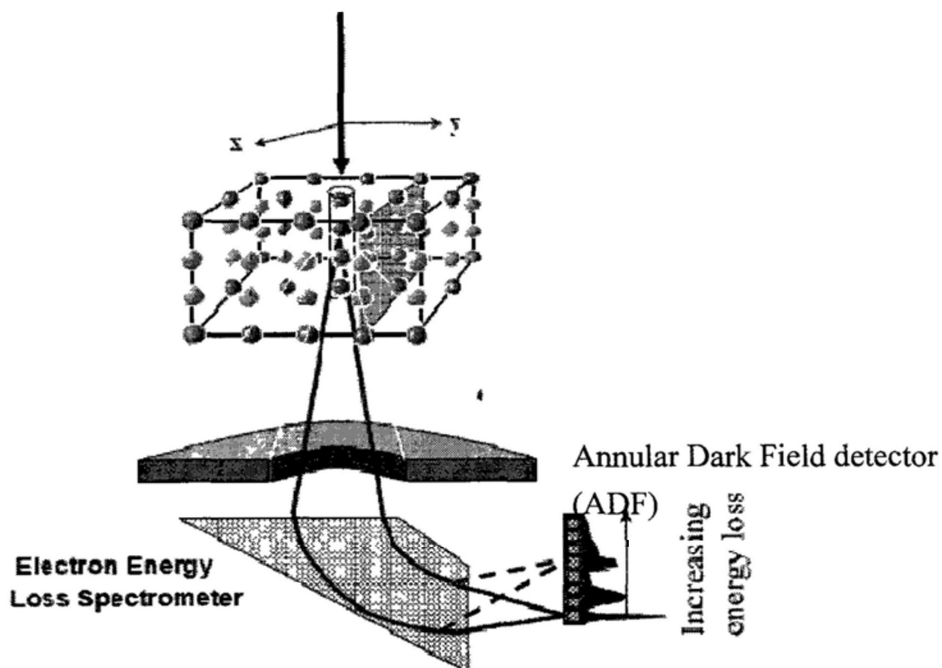


Fig. 4 ADF detector and line-scan mode

The DF images in STEM can be obtained by selecting the electrons that suffered energy loss of several eV, for example the plasmon excitation, or selecting the electrons suffered higher energy loss such as the inner-shell electron excitations. In our experiments the contrast of the image in the Si/SiO2 nanostructures is highly expected. The boundary of the silicon/silica nanostructures can be clearly distinguished by choosing the electrons involved in the imaging process with different energy, this can be attribute to the different plasmon excitation energy of silicon and silica. The configuration of the detector is illustrated in Fig.4. We can see the ADF detector is located in the region between the view screen and the specimen plane. Also, because of the scanning controlling system can determine the trajectory of the electron probe, the line-scan EELS mode is also available in a STEM.

## 3.2 electron energy loss spectroscopy

### 3.2.1 EEL spectrometer

When the electron beam is striking on a piece of thin specimen, the incident electrons will suffer from energy loss due to their interaction with the material. The EEL spectrometer is used to collect the scattered electrons and disperse them on the detector to form a spectrum.

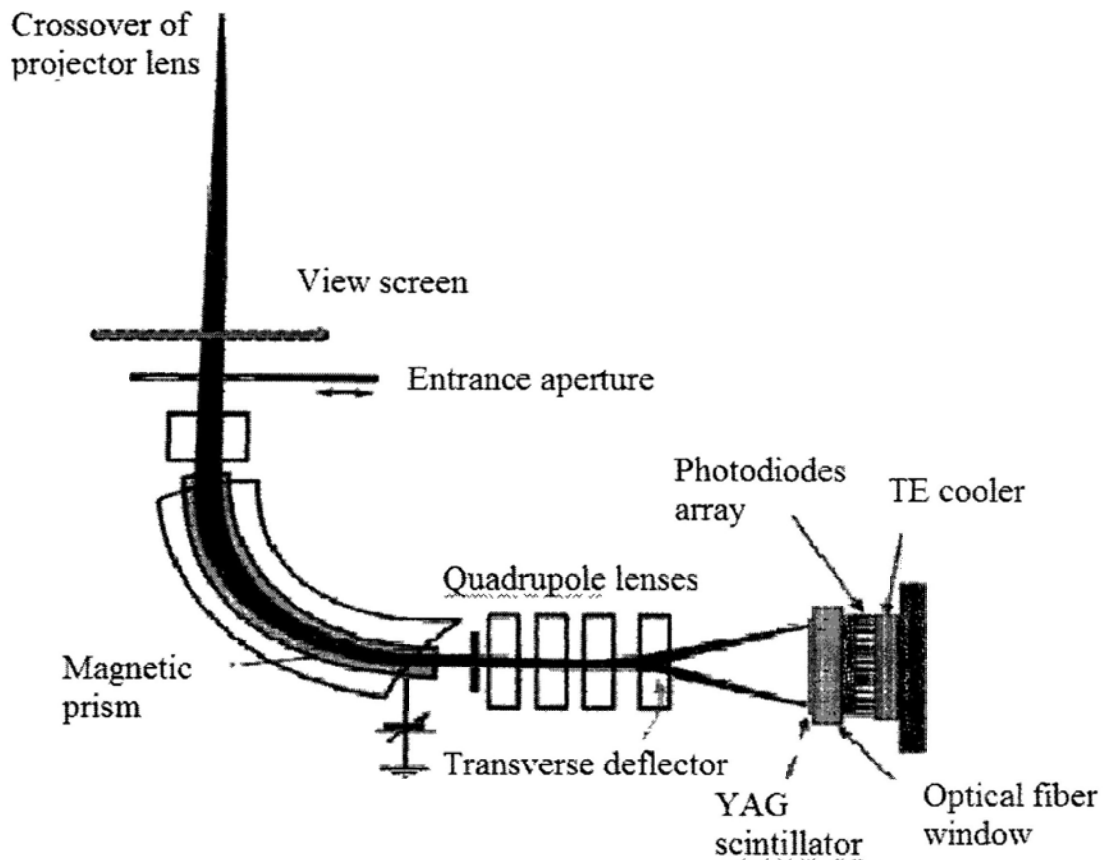


Fig.5 schematic illustration of parallel EELS

There are two ways to acquire a spectrum: serial acquisition EELS (SEELS), in which the spectrum is collected in one channel at one time; and parallel EELS (PEELS), in which the spectrum can be acquired through all the channels simultaneously. Apparently, the efficiency of PEELS is much higher than that of SEELS as the electrons from all regions of interest are collected for the whole integration time. In the experiments, PEELS mode is adopted to obtain the spectrum all the time. In the following discussion the term EELS refers to PEELS.

The schematic illustration of the PEELS is presented in Fig.5, the projective lens crossover serves as the objective plane of the spectrometer. After the electron get

through the entrance aperture, the magnetic prism will disperse the electron according to the different energy of the electrons, a YAG scintillator coupled via fiber optics to a semiconductor photodiode array in the dispersion plane of the spectrometer is mounted after the electron shield, the function of the quadrupole lenses will be introduced in Gatan Image Filter in the section of Energy Filtered TEM. The photodiode array consists of multiple electrically isolated silicon diodes which are thermoelectrically cooled.

The spectrum accumulates across the whole energy range simultaneously, the integration time can vary from milliseconds to hundreds of seconds. After integration, the whole spectrum can be read out via an amplifier though A/D converter and into multi-channel analyzer system.

### 3.2.2 spatially resolved EELS

In order to determine the changes of the surface/interface plasmonic excitation modes in the near surface/interface region, the ability of displaying the distribution of the spectra is expected. For example when we are investigating the detailed spectra features across an surface/interface, the most important information lies in the variation between the successive two spectra, which are taken in the successive position of the probe. Thus the expectation of acquiring the spectrum in the corresponding position of the specimen through a point by point manner becomes more and more important. Jeanguillaume and Colliex[66,67] proposed the new technique in EELS measurement named as spectrum imaging or spatially resolved

EELS to meet this requirement.

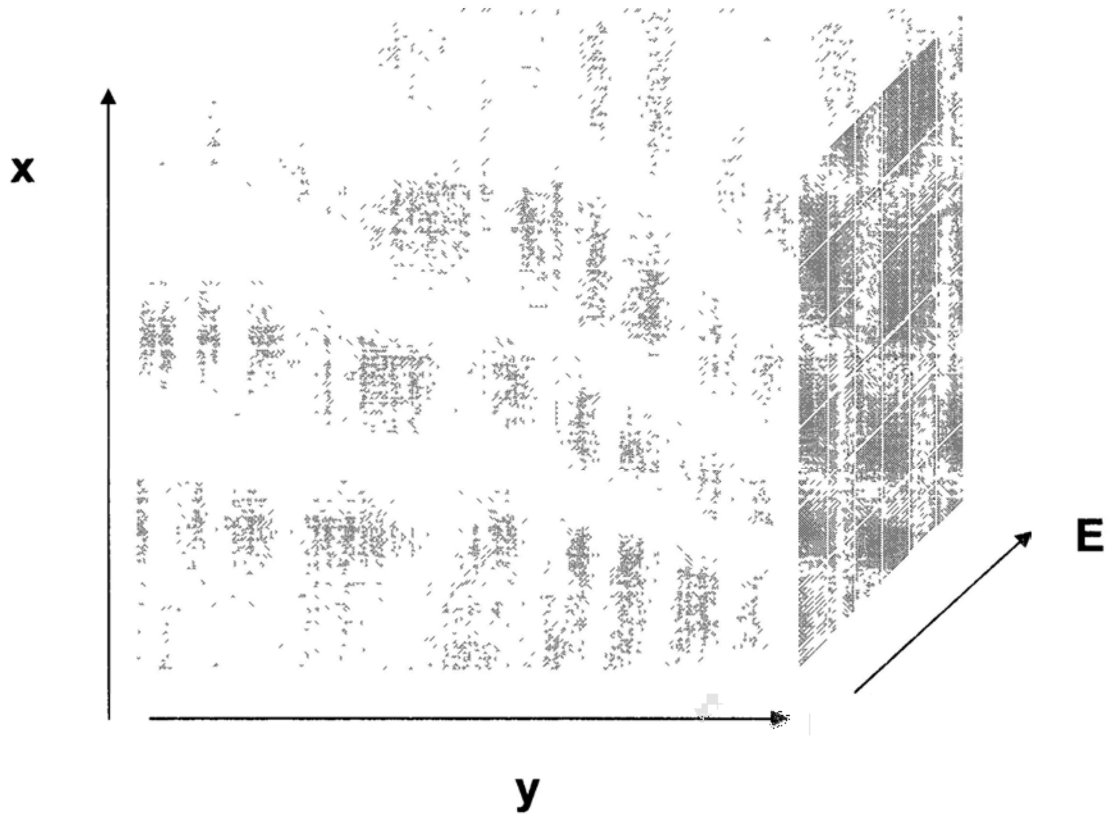


Fig.6 data cube of the spatially resolved EELS

The spatially resolved EELS (SREELS) allows the investigation on individual specimen structure such as Si nanostructures in our experiments, giving information on both single electron excitation and collective electron oscillation such as plasmon, also the spatial distribution of specific excitation will be given [68-70]. When the electron probe in the STEM scanned over one specific region of the specimen in a point by point manner, the spectra will be taken at the real space thus the data tube shown in Fig.6 can be constituted. The *x*-axis and *y*-axis corresponds to the spatial position of the area of interested, and the energy dispersion is along the *z*-axis in each

point of the spatial position. Thus each unit array along the energy axis indicates the spectra in the corresponding coordinates. The spatial resolution is determined by both the size of the electron probe and the step size of the two successive acquisition of spectra.

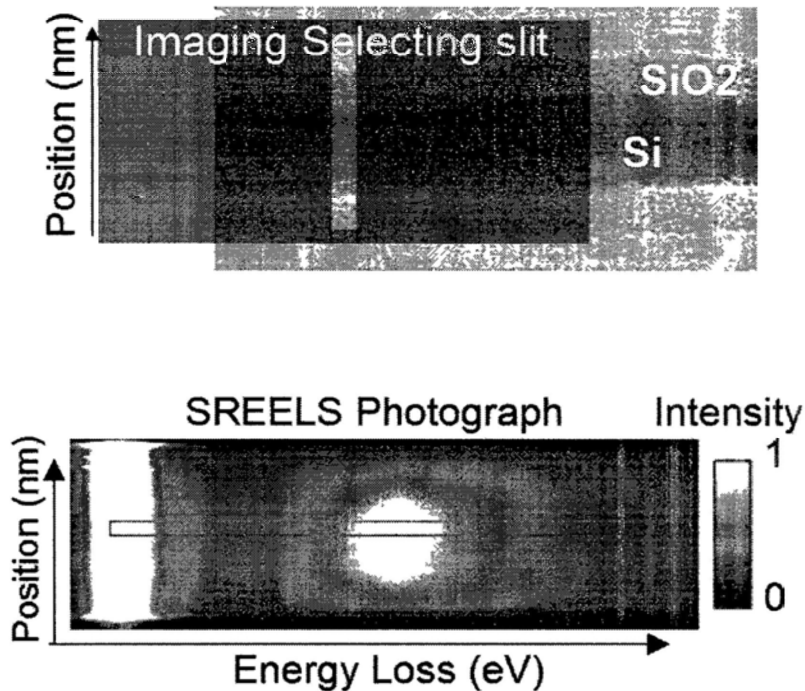


Fig. 7 (a)spatially resolved EELS illustration of imaging selecting slit and

(b)the spectrum image of the selected area

In our experiments, an imaging selection slit near the image plane of the objective lens was used to select the area of the specimen we were interested in. Because only one-dimensional spatial coordinates is involved, the data cube is transformed into a spectrum image. The SREELS spectra image of one sampling Si nanowire is shown in Fig.7(a), with the $x$-axis representing the energy loss and $y$-axis the spatial coordinate in the real space. By integrating the energy loss intensity along

the *y*-axis for a chosen pixel size (shown in the rectangular in Fig.7(b)), the spatially resolved EEL spectra from the corresponding area of interests can be reproduced. The detailed analysis will be imposed in the Chapter 4-7, it is also evidenced that SREELS is an perfect alternative to the conventional line-can EELS detection in STEM[68].

### 3.2.3 Energy Filtered TEM

In the STEM section (3.1.2) and EEL spectrometer section (3.2.1), we discussed that the entrance slit or entrance aperture will allow some part of the diffraction pattern to transmitted into an EEL spectrometer, so that the EEL spectra or an image will be recorded. The image will be produced with electrons having energy loss of specified value. In section (3.2.1) we have seen the structure of the EEL spectrometer is basically the Gatan Image Filter(GIF)[24]. The difference between the PEELS and GIF are that an energy selecting slit after the magnet, and multipole correction lenses and a two dimensional slow scan CCD array detector instead of a photodiode array detector are used.

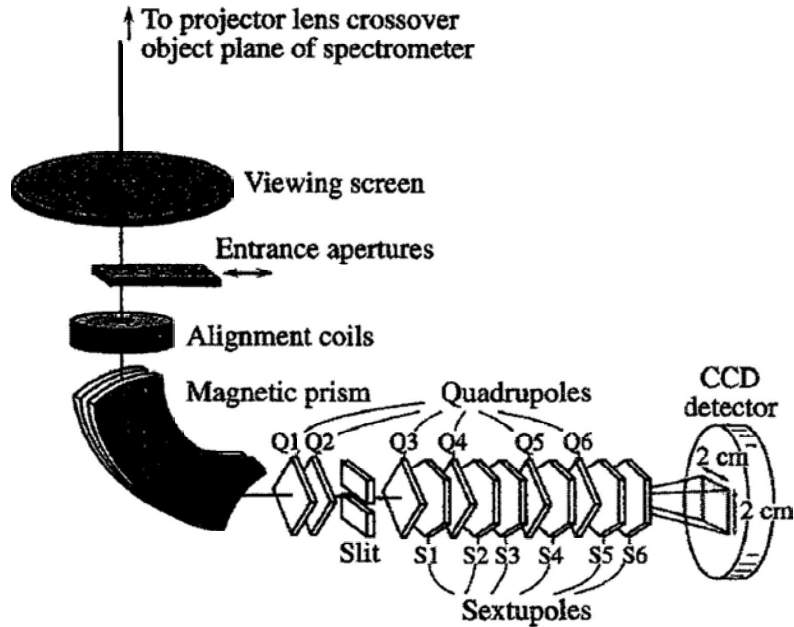


Fig.7 Gatan Image Filter attached to the TEM/STEM column

The Fig.7 given the schematic description of the GIF. In order to get good quality images with the electrons suffered energy loss, the first two quadrupoles increase the dispersion of the spectrometer onto the slit. The quadrupoles after the slit have two functions: one is to project the image of spectrum at the slit onto the CCD, the other one is to project the image of the specimen onto the CCD. The former one is just the same as standard PEELS, and for the latter one it produces the energy filtered TEM images (EFTEM) selected by the slit.

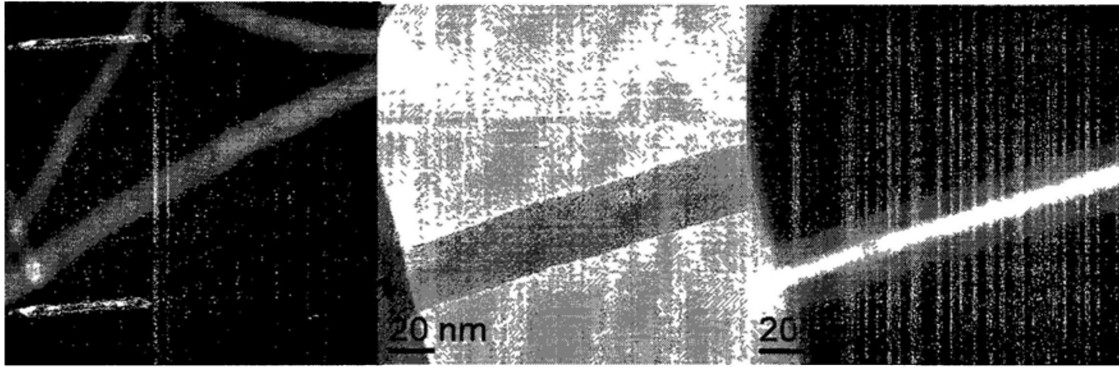


(a) (b) (c)

Fig.8 comparison between

(a) dark field (b) bright field and (c) energy filtered TEM image

One of the example of EFTEM image is shown in Fig.8. The specimen in the experiments is composed of Si cored nanowire, coated by the shell of $SiO_2$, in the BF and DF images, the Si core and $SiO_2$ shell can not be distinguished while in the Fig.8(c) the Si core and oxidation layer can be clearly distinguished, by selecting the bulk plasmon energy of Si (~16.5 eV) in EFTEM imaging mode.

# Chapter 4. Interface plasmon excited on planar $Si/SiO_2$ interfaces

## 4.1 Experimental results

### 4.1.1 Spectrum recording mode

In the EELS experiment, the spectra may be taken at different modes that give different information of the material plasmon oscillation. The simplest experiment can be done at the TEM-image mode, i.e., a large area of specimen is illuminated by a broad electron probe first. When the beam transmits the specimen, the exit energy loss electrons will be dispersed and refocused at the dispersion plane before they are recorded by CCD at the back of the EEL spectrometer. The image mode has rather poor spatial resolution due to the large illumination area of the specimen.

There are two other modes that provide much more spatially resolved information--the line-scan spectrum mode and spectrum imaging mode. In line-scan mode, a series of EEL spectra can be recorded in a point-by-point manner a focused electron probe travels along a fixed path. The real space spatial resolution is mainly

determined by the finite electron probe size, which can be as small as sub-nanometers. In spectrum imaging mode, the spectrum-image is taken by one shot and such a spectrum-image contains all the spectra data from the confined sample region, the detailed information can be found in the last chapter.

### 4.1.2 General features in the spectrum taken at the imaging mode

The Si/SiO2 interface in planar geometry draw much attraction because of the influence on the performance of semiconductor devices[5,53,71]. In this chapter we using the spectra taken from spectrum imaging mode to show how the plasmon excitations in the near region of Si/SiO2 interface can be affected by the factors such as: impact parameter of the incident electron and the thickness of the specimen.

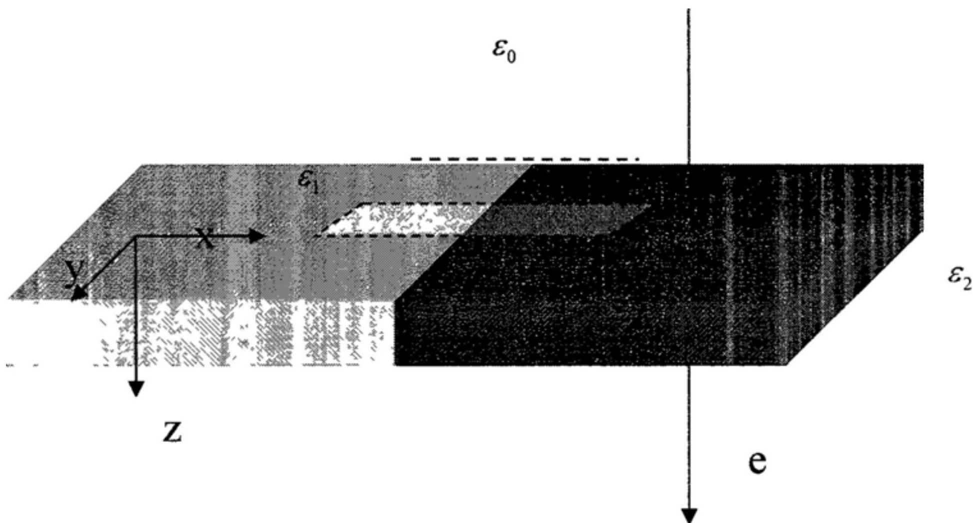


Fig. 1 Geometrical configuration of the Si/SiO2 interface structure.

The sample is composed of Si and SiO2 layer, which configuration is similar to that shown in Fig.1. Rectangular box indicates the sample region confined by

spatially resolved EELS slit, the single broken curve shows the electron beam path in line scan EELS mode (see following part). The SiO2 layer is formed on the surface of Si substrate by thermally oxidization with thickness ~200 nm. After conventional TEM cross sectional sample preparation, the sample was loaded in the microscope for investigation.

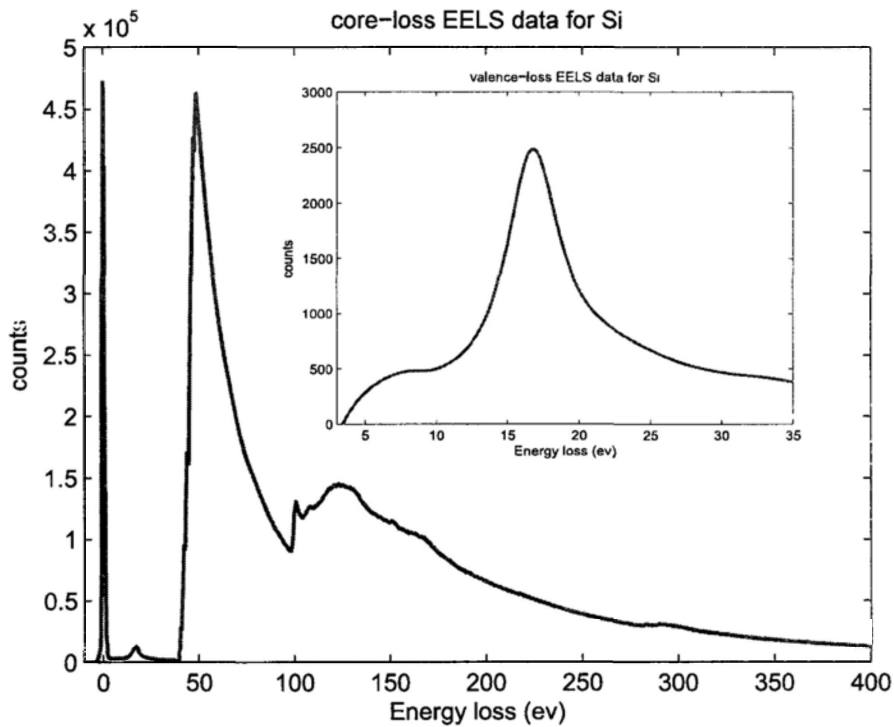


Fig 2(a) EEL Spectrum of bulk Si (inset shows the detail in the interested part after zero loss peak subtraction)

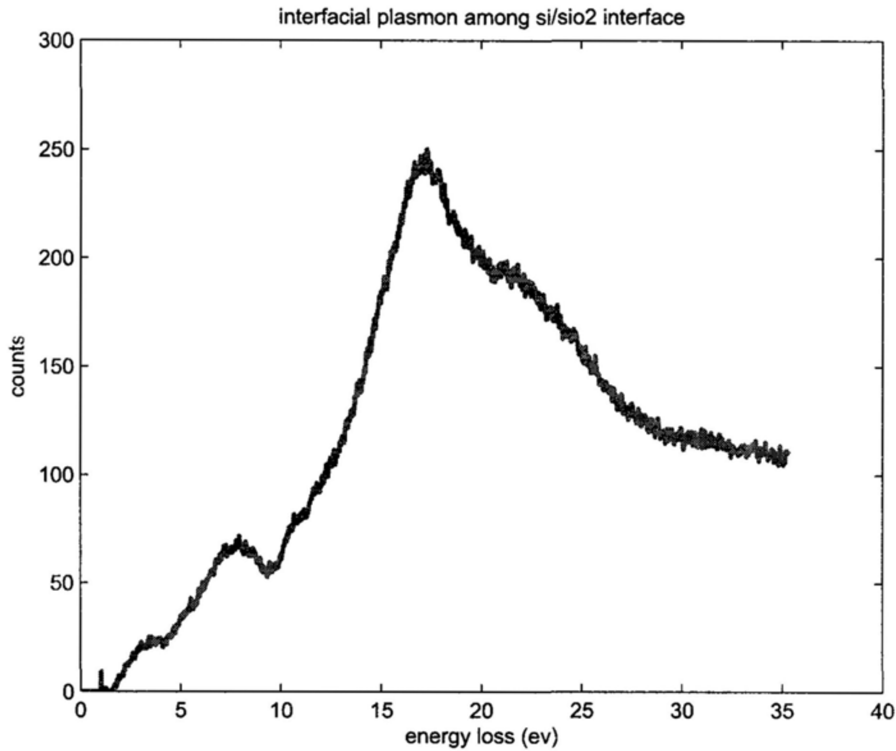


Fig. 2(b) EEL Spectrum of Si/SiO2 interface after zero loss peak subtraction

Fig.2(a) shows the EEL spectrum taken from silicon, the inset of which is the enlarged part of the low loss region after the zero loss peak subtraction. From the inset image we can see the most distinguished feature in this region is the bulk plasmon peak located at ~17ev. By focusing the electron probe at the Si/SiO2 interface, one would obtain a different EEL spectrum (Fig.2(b)). Both the Si (~17 eV) and $SiO_2$ (~23 eV) bulk plasmon peak can be observed. In addition, a peak at ~8eV appears, commonly ascribed to the interfacial plasmon peak (IPP).

**4.1.3. Spatially resolved EELS taken at the Si/$SiO_2$ interface**

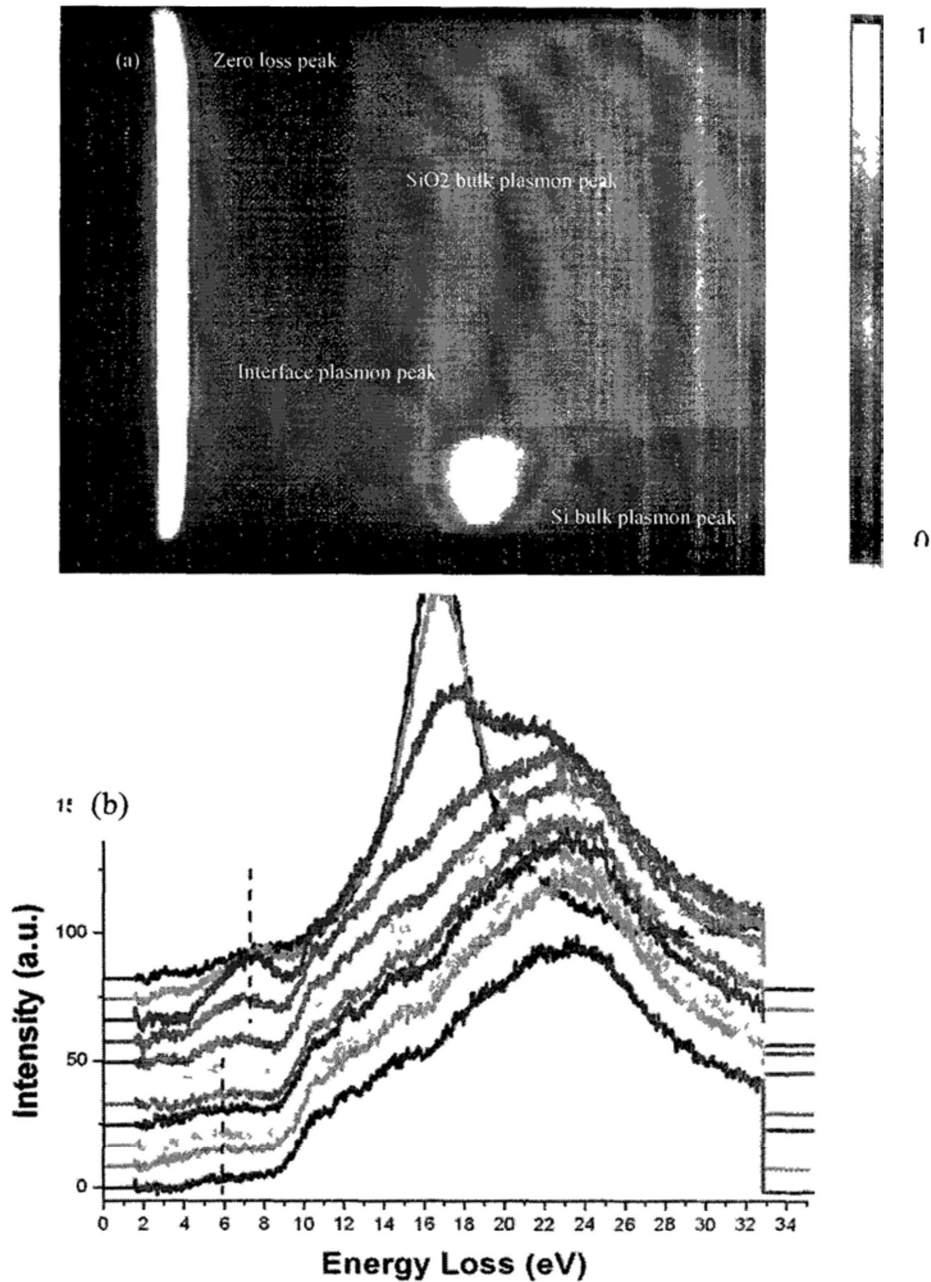


Fig. 3(a) Typical EEL spectra-image for Si/SiO2 planar interface (color bar indicates the intensity distribution) (b) the extracted corresponding EEL spectra

The interface plasmon of $Si/SiO_2$ would change as a function of the experimental impact parameter, which is defined as the distance between the electron probe and the exact interface. The polarity of the impact parameter value depends on the position of the electron beam. If the electron beam is in Si side, the impact

parameter is defined as negative value, while the positive value indicates the beam is in $SiO_2$ side. Now we illustrate this using a typical Si/SiO2 (with specific sample thickness) EEL spectrum-image (Fig.3(a)) as an example. The selected sample region is similar to the one in Fig.1. In the spectrum image, the horizontal axis is the energy dispersion, ranging from ~5ev to ~35ev. The vertical axis is the spatial distribution of the selected sample region, which is approximately 12 nm long across the Si/SiO2 interface. The Si/$SiO_2$ interface sits at the position 3nm above the bottom of the spectrum-image. Below the interface is the Si substrate and above is the SiO2 layer. One can see that the zero loss feature has the strongest intensity in the spectrum image, due to the large amount of transmitted and elastically scattered electrons. The bulk plasmon features of both Si and SiO2 can be clearly observed in the corresponding regions. A relatively weak IPP appears in the region near the interface, with its peak energy lies between zero and the Si bulk plasmon energy. Its intensity decreases rapidly as the impact parameter increases.

The extracted EEL spectra are plotted in Fig.3(b). From bottom to the top, the spectrum comes from the corresponding position as in the spectrum-image. The bulk plasmon peak of Si and SiO2 can be clearly distinguished, together with the IPP located in the range from 6 to 8eV.

### 4.1.4 Thickness dependence of the plasmon oscillations

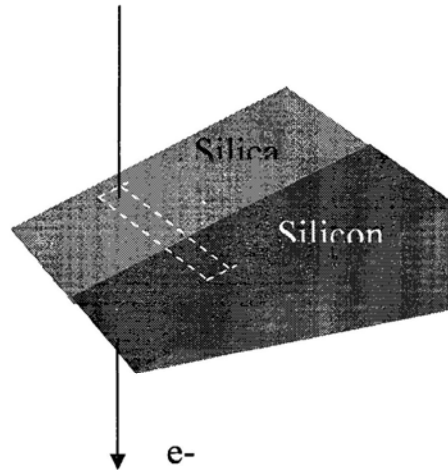


Fig. 4 Scheme of TEM sample shape for Si/SiO2 interface

The interface plasmon also changes as a function of the sample thickness (electron travel distance inside the sample). Here we took advantage of the TEM sample's wedge shape, i.e., the area near the peroration is the thinnest part, as electron beam travels away from the perforation, sample is getting thicker and thicker (as indicated by Fig.4). The following spectrum images were taken from sample regions with different thickness.

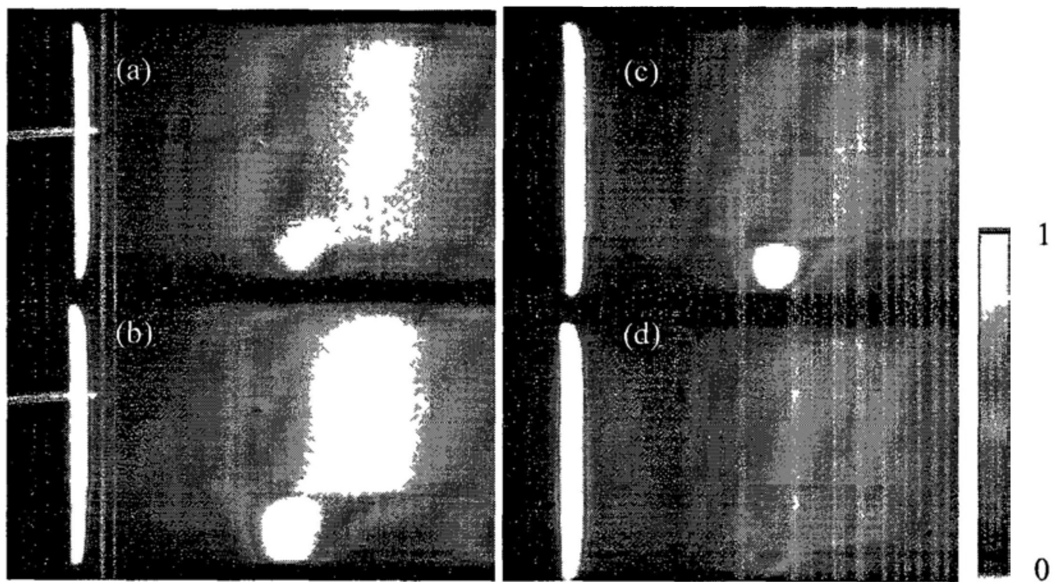


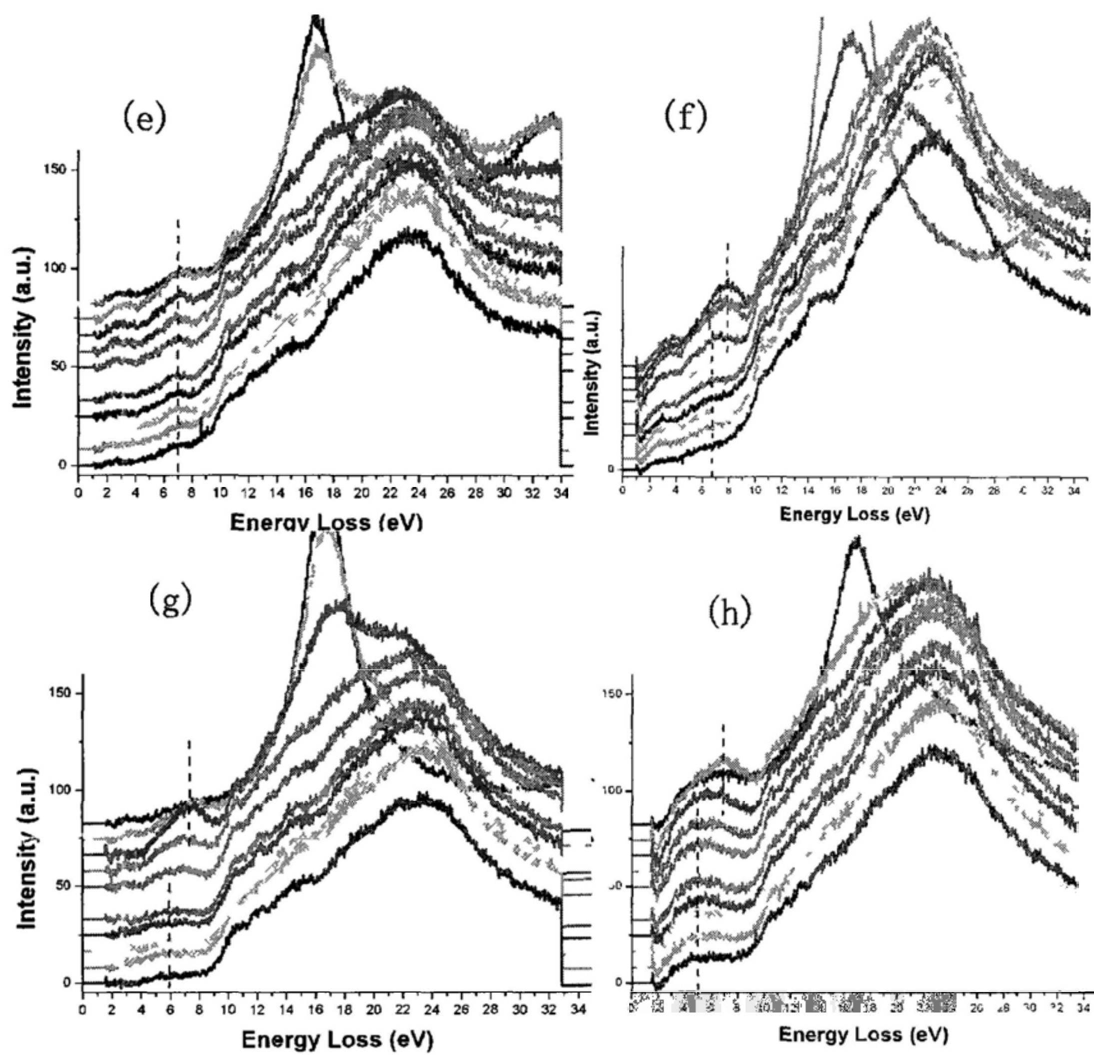


Fig.5 (a)-(d), spectrum-image for 4 different specimens, from top to bottom $T/\lambda = 3.3$, 2.65, 1.1 and

0.36. (e)-(h), EEL spectra of the four specimen with different impact parameters, in each of the single figure, the spectra from top to bottom corresponds to positions from the silicon side to the silica side

As the absolute sample thickness is difficult to evaluate, here we use the ratio of sample thickness (T) to electron mean free path (λ) to describe the different sample thickness. The T/ λ value can be estimated by the equation: $T / \lambda = \log I_0 / \log I_t$, where $I_0$ is the integrated intensity of the zero loss peak, and $I_t$ the integrated intensity over the whole spectrum range. The spectrum-images taken at 4 different T/ λ, i.e, 3.3, 2.65, 1.1 and 0.36, are shown in Fig.5 (a)-(d), respectively. The corresponding EEL spectra extracted from the spectrum-images are shown in Fig.5 (e)-(h). It can be seen that for very thick sample the IPP position does not change much when the electrons travel through the interface (Fig.5(e)). As a comparison, more and more obvious shift of the IPP position with the impact parameter is observed when the samples are getting thinner and thinner. Fig.5(f) shows an energy shift from 7.8 eV to 6.9 eV for $T / \lambda \approx 2.65$ sample, and 7.5eV to 5.1 eV for $T / \lambda \approx 1.1$ sample in Fig.5(g), 7 eV to 4.8 eV for $T / \lambda \approx 0.36$ sample in Fig.5(h). Such observation is consistent with the literature results [71].

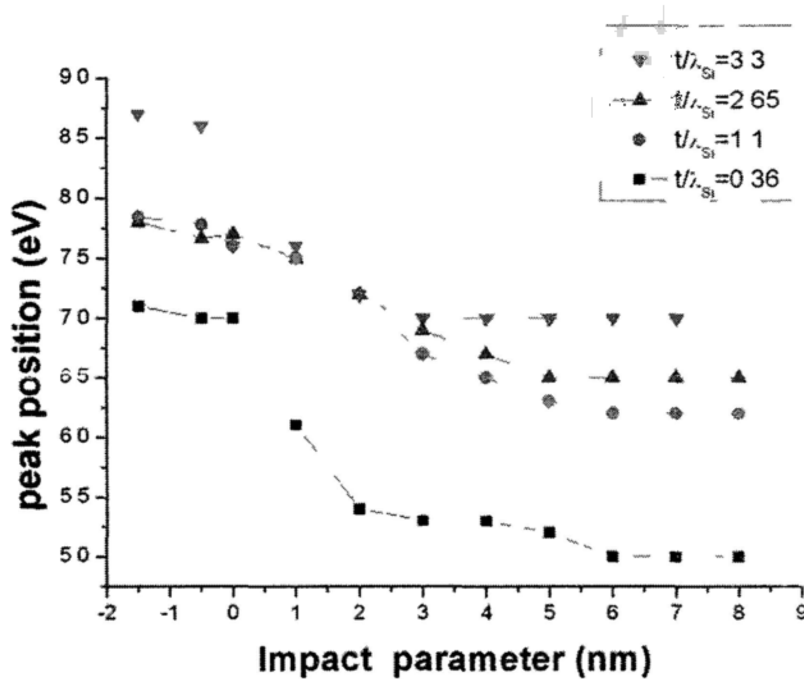


Fig. 6 Experimental results of IPP position as a function of impact parameter for different specimens,

$T/\lambda = 3.3$, 2.65, 1.1 and 0.36

Fig.6 plots the IPP position variation as a function of the impact parameter for the 4 different sample thickness. For all sample thickness, the IPP energy position red shifts as the impact parameter changes from negative value to positive value, and eventually levels off at a fixed value for further increase in the impact parameter. At small impact parameters, the IPP energy positions are similar except for the thinnest sample (T/λ =0.36) and thickest sample (T/λ =3.3). When the impact parameter is positive large enough the IPP positions levels off to a constant value for each specific sample thickness, for example, 7.0ev for sample with $T/\lambda = 3.3$, 6.5ev for sample with $T/\lambda = 2.65$, 6.2ev for sample with $T/\lambda = 1.1$, and 5.0ev for sample with $T/\lambda = 0.36$.

### 4.2 Simulation results

#### 4.2.1 The simulation model

Since there is no exactly analytical formula to describe the energy loss of the fast electron interacted with material at planar interface to date, all of the calculation results are approximations to some extent. This section is based on the model structured by Molina [53] etc., which is similar to that described in Fig.1.

$$\frac{d^2P}{d\omega dz}=\frac{e^2}{2\pi^2v^2\varepsilon_0\hbar}\mathrm{Im}\{\int_0^{k_{ym}}dk_y[-\frac{1}{\varepsilon_2\nu}+\frac{1}{\varepsilon_2\nu}\exp(-2\nu x_0)+\frac{2\exp(-2\nu x_0)}{\nu}\{-\frac{1}{\varepsilon_2+\varepsilon_1}\}]\}$$

(4.4)

$$\frac{d^2P}{d\omega dz}=\frac{e^2}{2\pi^2v^2\varepsilon_0\hbar}\mathrm{Im}\{\int_0^{k_{ym}}\begin{matrix}dk_y[-\frac{(1-\varepsilon_2\beta^2)}{\varepsilon_2\nu_2}+\frac{(1-\varepsilon_2\beta^2)}{\varepsilon_2\nu_2}\exp(-2\nu_2x_0)+\\ 2\exp(-2\nu_2x_0)\{-\frac{1}{\varepsilon_2\nu_1+\varepsilon_1\nu_2}+\frac{\beta^2}{\nu_1+\nu_2}\}]\}\end{matrix} \quad (4.5)$$

$$\nu=\sqrt{k_y^2+\omega^2/v^2}\,,\ \nu_j=\sqrt{k_y^2+\omega^2/v^2(1-\varepsilon_j\beta^2)}\,,\ \beta=v/c$$

Starting from the simplified equation (4.4) and (4.5), the excitation probability $P$ per unit length along the trajectory and per unit frequency can be obtained, for non-relativistic consideration and relativistic consideration respectively.

In both equations, the integral upper limit $k_{ym}$ is the largest scattering vector along the interface direction ($y$-direction). It is known that the value of scattering vector is determined by the wave vector of incident electron and scattering angle together. Experimentally, the scattered fast electrons which can enter the spectrometer

are determined by the size of the entrance aperture, and the effective collection angle can be estimated as 15 mrad for a 2 mm entrance aperture, while the cut-off angle for silicon is around 7 mrad [4]. Therefore, we take 7 mrad as the largest scattering angle for $k_{ym}$ calculation.

Although the scattering vector $k$ should have projections along both $x$ and $y$ directions, i.e., $k_x$ and $k_y$, the literature results [53] suggested that the IPP intensity and energy position are not affected by the $k_x$ limitation. Consequently, we do not involve $k_x$ in the present simulation.

$\varepsilon_1$ and $\varepsilon_2$ are the dielectric functions of Silicon and Silica, which are obtained from the optical database. The impact parameters we choose here ranged from -5 nm to 10 nm, i.e., the electron beam is scanned from the silicon side to the silica side across the interface. 0 nm impact parameter indicates the exact interface location.

The term containing $\mathrm{Im}(-1/\varepsilon_2)$ comes from the bulk plasmon contribution while the term containing factor $\mathrm{Im}[1/(\varepsilon_1+\varepsilon_2)]$ gives rise to the interface plasmon peak, the factor $\mathrm{Im}[1/(\varepsilon_1+\varepsilon_2)]$ is also named as interface response. The Begrenzung effect[5,72,73] describes that the bulk plasmon intensity may decrease and the IPP intensity may increase at the same time due to the appearance of surface mode. The exponential terms $\frac{1}{\varepsilon_2\nu}\exp(-2\nu x_0)$ and $\frac{(1-\varepsilon_2\beta^2)}{\varepsilon_2\nu_2}\exp(-2\nu_2 x_0)$ depict this trend of the bulk plasmon peak for non-relativistic, and relativistic situation, respectively. Correspondingly the terms containing $\frac{2\exp(-2\nu x_0)}{\nu}\{-\frac{1}{\varepsilon_2+\varepsilon_1}\}$ and

$\exp(-2\nu_2 x_0)\{-\frac{1}{\varepsilon_2\nu_1+\varepsilon_1\nu_2}+\frac{\beta^2}{\nu_1+\nu_2}\}$ depict the IPP for non-relativistic and relativistic situation respectively.

### 4.2.2 Non-relativistic consideration with zero impact parameter

As described in the previous sections, the IPP arises from the term containing the factor $\frac{2e^{-2\nu x_0}}{\nu}\{-\frac{1}{\varepsilon_2+\varepsilon_1}\}$ in the integration in formula (4.4) for non-relativistic situation, and the parameter $\nu$ is the same for the two materials (Si and $SiO_2$).

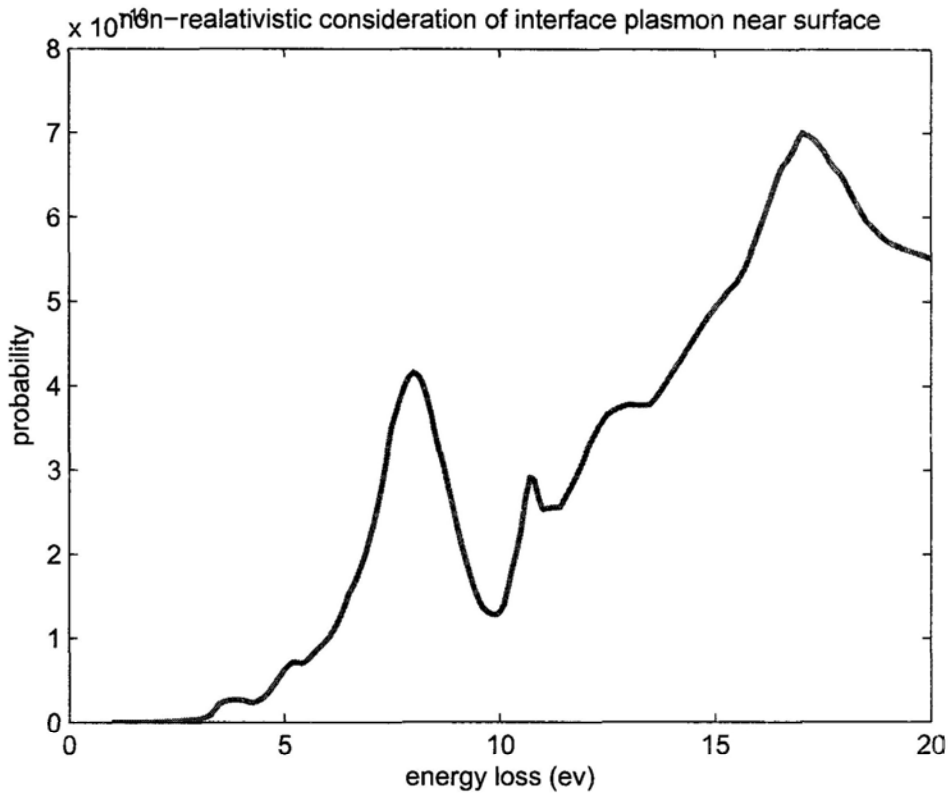


Fig. 6 Simulated spectrum for non-relativistic consideration with impact parameter as 0.

Fig.6 shows the non-relativistically treated spectrum with zero impact parameter. The IPP located at 7.5 eV can be seen clearly in the spectrum. The bulk plasmon peak of Si at ~17ev can also be distinguished. The broaden shoulder after

17ev comes from the bulk SiO2 plasmon peak which is located at ~23 eV. The spectrum calculated at 0 impact parameter exhibits basic features of Si/SiO2 IPP. How this IPP change with impact parameter will be discussed in the next section.

### 4.2.3 Non-relativistic consideration with different impact parameter

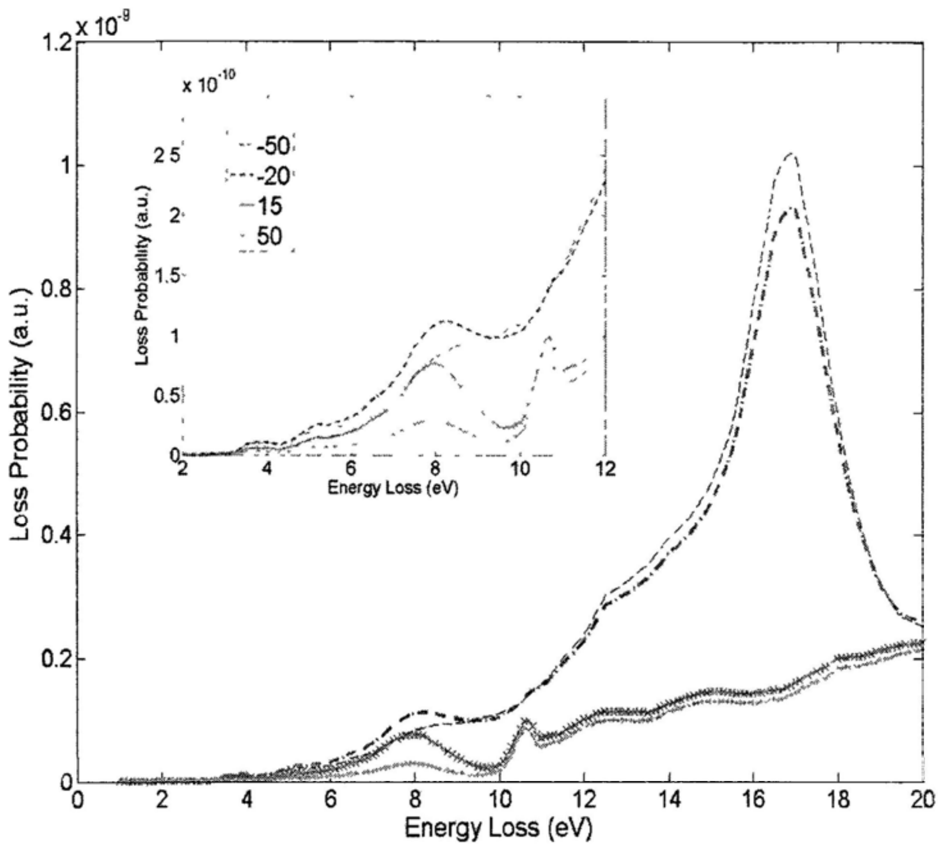


Fig. 7 Calculated spectra for non-relativistic consideration with different impact parameter.

For the non zero impact parameters, the situation is more complicated. Fig.7 shows calculated spectra for different impact parameters of one sample. From the top to the bottom spectra, the impact parameter increases from -5 nm to 5 nm, as the electron travel through Si side across the interface to $SiO_2$ side. The inset shows the

enlarged energy region containing IPP.

Similar to the result at zero impact parameter, the IPP can be distinguished clearly at ~8eV. The bulk plasmon peaks for Si and $SiO_2$ locate at ~17ev and ~23ev (not shown completely in the figure), which is originated from the term containing $\mathrm{Im}(-1/\varepsilon)$ in the analytical formula. It is intuitive that the IPP intensity decreases with the impact parameter increases, as a result of the exponential factor $\exp(-2\nu x_0)$. No shift on the IPP energy position is generated in the simulation, due to the face that the integration over $k_y$ for term containing $\mathrm{Im}(1/(\varepsilon_1+\varepsilon_2))$ in the non-relativistic equation (4.4) is only a scaling factor.

### 4.2.4 Relativistic consideration with different impact parameter

One would notice that the above simulated results do not agree with the experimental results as impact parameter increases. In this regard, we took relativistic effect into account. The relativistic effect would modify the speed of the fast electrons when they enter the medium. In addition, the retardation effect can not be ignored at large impact parameters.

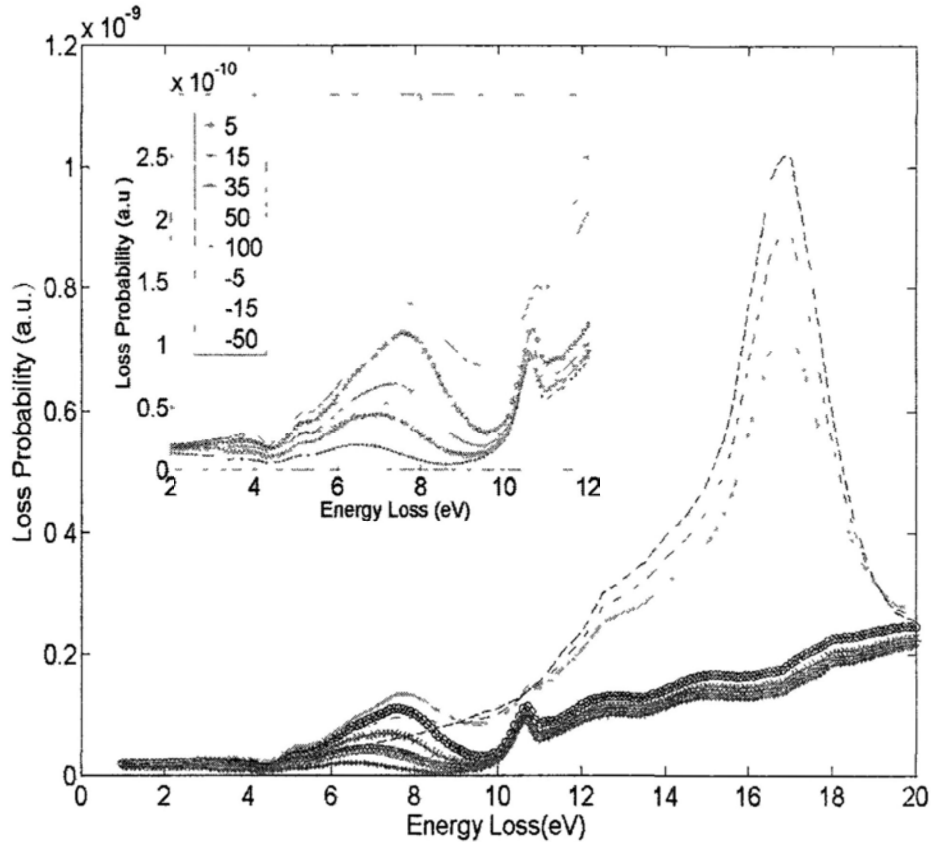


Fig. 8 Calculated spectra under relativistic consideration with different impact parameters.

Fig.8 shows the calculated spectra under the relativistic considerations for different impact parameters, from the top to the bottom the impact parameter increases from -5 nm to 10 nm, as the electron beam travels from Si to $SiO_2$ across the interface. The inset gives enlarged spectra which contain IPP as the main feature.

Similar to the non-relativistic case, the intensity of the IPP decreases when the impact parameter increases. Nevertheless, an energy shift from 7.6eV to 6.5eV occurs in the IPP as the impact parameter increases from 0.5nm to 10nm, which agrees well with the experimental results.

In the integration $\text{Im}\{\int_0^{k_{ym}} dk_y[2\exp(-2\nu_2 x_0)\{-\frac{1}{\varepsilon_2\nu_1+\varepsilon_1\nu_2}+\frac{\beta^2}{\nu_1+\nu_2}\}]\}$, the IPP arises from the factor $1/(\nu_1\varepsilon_1+\nu_2\varepsilon_2)$, which is different from the non-relativistic ones. Due to the finite speed of electron beam, $\nu_1$ and $\nu_2$ cannot be simply replaced by $\nu$ as in the non-relativistic case. On the other hand, the term $\frac{\beta^2}{\nu_1+\nu_2}$ can be ignored in the integration due to its small value. At large values of $k_y$, interface plasmon peak around 8eV is obtained from the integral, being the same as the non-relativistic case. This is because $\nu_1 \approx \nu_2 \approx \nu$ for large $k_y$ value. Large $k_y$ corresponds to a small value of scattering wavelength in the real space, when the wavelength is much smaller than the size of the scattering object, the retardation effect can be ignored. As a comparison, at $k_y$, the term in the integration cannot be simplified, leading to different interface plasmon peak at around 6ev, which is called the relativistic peak [53]

The exponential factor $\exp(-2\nu_2 x_0)$ depends on $k_y$ as well, when the impact parameter $x_0$ increases, the contribution from the high value of $k_y$ becomes more and more trivial in the integration, so that the relativistic peak is left to dominate the final spectrum.

### 4.2.5 comparison between experimental and simulated results as a function of the impact parameter

In this section we make comparison between our experimental results and the simulated ones when the impact parameter changes.

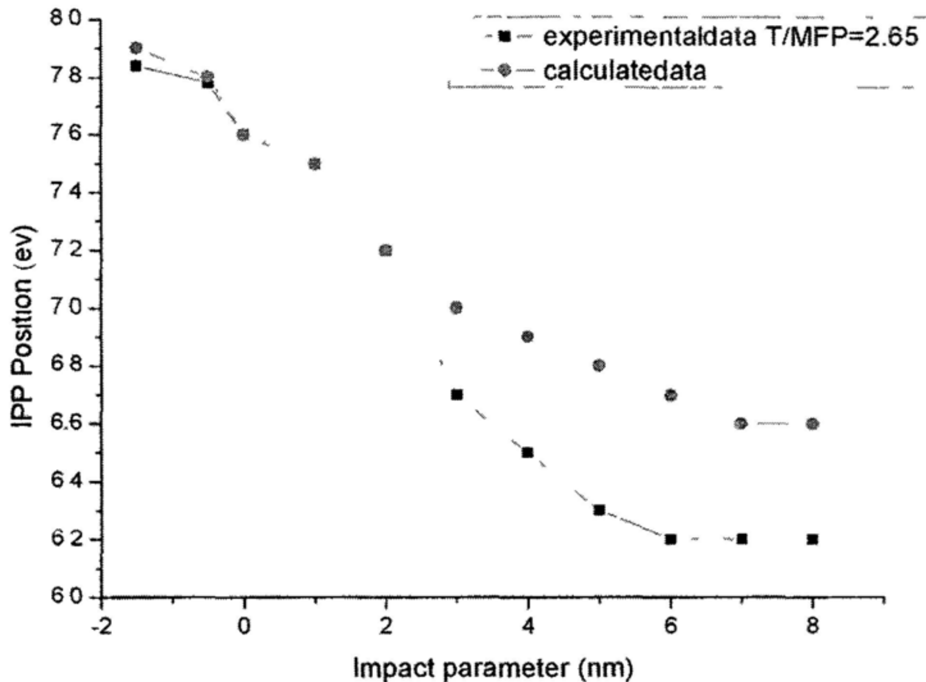


Fig. 9 Comparison between simulated IPP energies and experimental ones, as a function of the impact parameter

Fig .9 shows the comparison between calculated IPP positions and experimental ones, as a function of the impact parameter. When the impact parameter increases from negative to positive values, the IPP energy goes through an exponential decay in both the simulated and the experimental data. As we know the

energy resolution of the EEL spectrometer is around 0.7 eV, the simulated data can be seen to match the experimental ones well.

Although general agreement exists between the simulated and the experimental results, the current theoretical model employed for simulation has some limitation.

1 It has been demonstrated in the experiment that the sample thickness affects the IPP energy, although not significantly when the impact parameter is not so large. Nevertheless, effect of sample thickness is not considered in both the non-relativistic (4.4) and relativistic formula (4.5).
2. The possible existence of a thin intermediate $SiO_x$ layer between Si substrate and SiO2 film has not been considered in the present model. Adding such a layer in the simulation may lead to better match with the experimental data [17]. Nevertheless, we did not detect such a layer in the experiments (with the current experimental spatial resolution), but cannot completely eliminate the possibility of the existence of such a layer with very small thickness.

### 4.3 Conclusion

In this chapter, we studied the interface plasmon of planar interfaces. Specimen with the $Si/SiO_2$ interface is prepared and the spatially resolved EELS experimental results disclose the presence of the interface plasmon, which intensity and/or energy change with the sample thickness as well as the impact parameter

variations. By introducing relativistic effect to the simulation model, a general agreement between the experiments and the simulations can be found.

# Chapter 5. Size Effect on the Interface Plasmon of $Si/SiO_2$ Nanostructures

In the last chapter, we have discussed the interface plasmon in planar $Si/SiO_2$ boundary with a thin film configuration, which can be treated as a two-dimensional system. In the present chapter, we will discuss the interface plasmon in Si-core/$SiO_2$-shell nanoparticles, with particular focus on how the geometrical size, i.e., the Si core radius and the $SiO_2$ shell thickness in the nanoparticles, affect the interfacial plasmon in the corresponding systems, using both experimental EELS and simulation approaches.

## 5.1 General spectrum features of the $Si/SiO_2$ core/shell nanoparticles

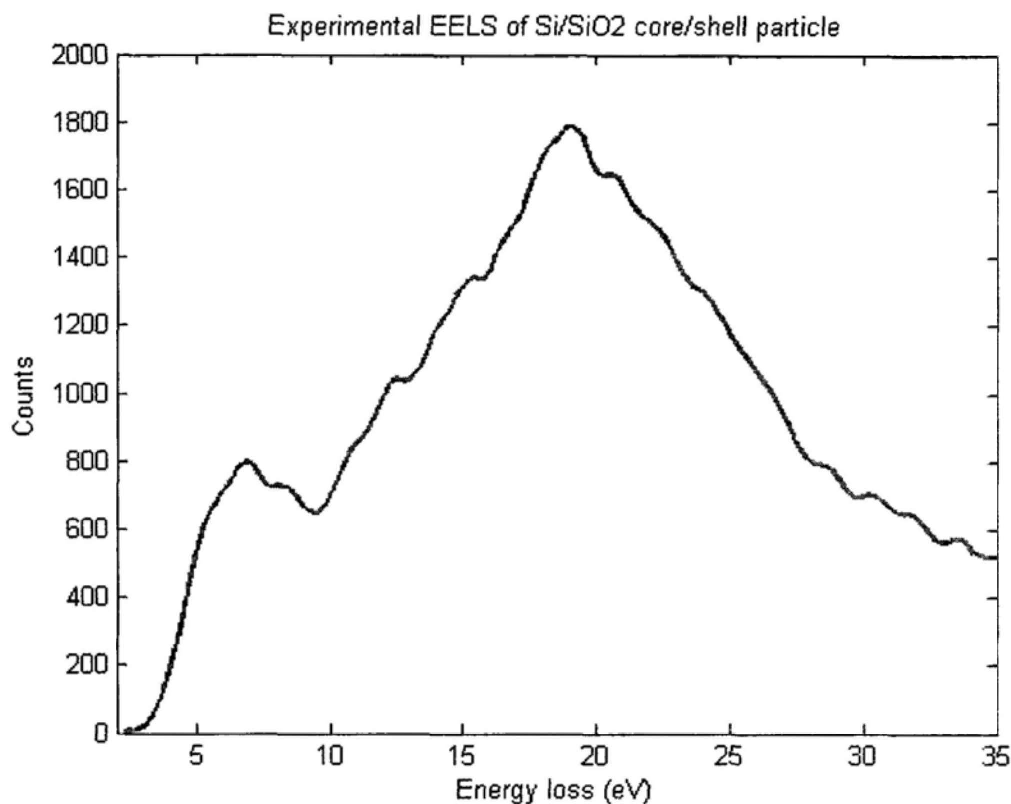


Fig.1 experimental EEL spectrum of $Si/SiO_2$ core/shell nanoparticle

The figure above shows a typical EEL spectrum taken from a $Si/SiO_2$ core/shell nanoparticle, in which the electron beam incidence on the particle at grazing angle. In the spectrum the zero loss peak (ZLP) was subtracted by using power law fitting [4]. Similar to the former cases, a broad peak centered at around 20 eV indicates the existence of bulk plasmon peaks of both Si (~17 eV) and $SiO_2$ (~23 eV) in the interface region. An additional IPP appears at ~7 eV, characterizing the collective oscillation of weakly bonded electrons at the interface of the core/shell nanoparticles.

## 5.2 Effect of the Si core diameter on the interface plasmon oscillation

### 5.2.1 Experimental EELS results from core/shell nanoparticles with different Si core size

The sample in the experiments is composed of the Si nanoparticles with different radius. The oxidation layer is usually unavoidable right after the Si particle is produced, due to the rough vacuum condition for the nanoparticle growth. After annealing this oxidation layer could be thicker. Therefore, the first step in the EELS experiment is to identify the size of the specimen of interest.

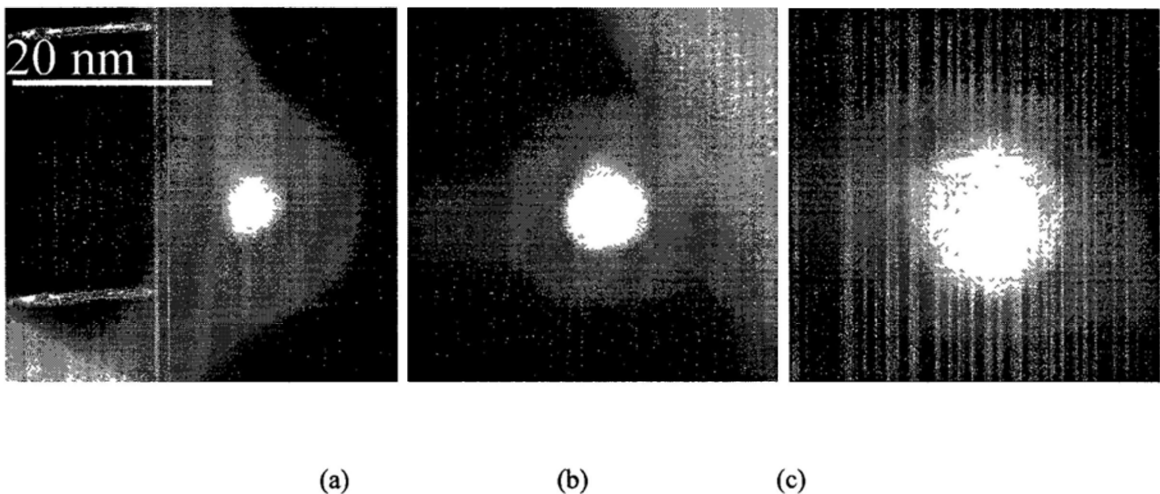


(a) (b) (c)

Fig.2 Energy filtered image of Si nanoparticle of different core size

(a) 2.5 nm radius (b) 4 nm radius (c) 9 nm radius

In the conventional BF (Bright Field) imaging method, it is difficult to distinguish the boundary between non-crystalline $SiO_2$ shell and crystalline Si core explicitly. Alternatively, the EFTEM (energy filtered transmission electron microscopy) image is employed to characterize the size of the Si core and $SiO_2$ shell.

The image is formed using a GIF (Gatan Image filter) with electrons of selective energy range (around the silicon bulk plasmon 16.9 eV in the present case). Consequently, we can estimate from Fig.2 that the three samples we examined have Si core radius of ~2.5 nm, ~4 nm, and ~9 nm, respectively. Their $SiO_2$ shell thicknesses are similar, i.e., ~6 nm.

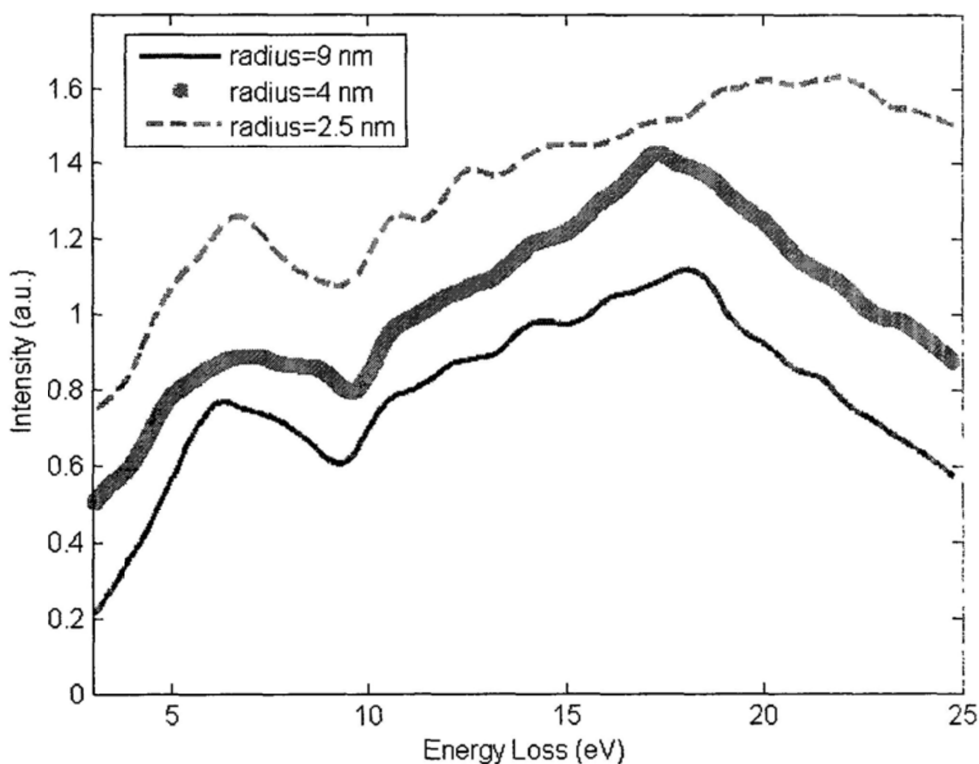


Fig.3 EEL spectra taken from Si nanoparticles of different core sizes, spectrum from top to bottom came from Si nanoparticle of radius ~9 nm, ~4 nm and ~2.5 nm, and the impact parameter is ~10nm, ~5 nm and ~3 nm respectively

The EEL spectra taken from the above three samples are shown in Fig.3. In each case the electron beam is located in the vacuum close to the outer surface of the nanoparticles. All the measurements were carried out using a 200 kV STEM. Due to

the high intensity of ZLP, short spectra acquisition time is used, leading to rough data in the low loss region (those close to the ZLP) after the ZLP subtraction. In the spectra shown in Fig.3, the IPP of the 2.5 nm Si-cored nanoparticle is found to center at ~7 eV. Some broadening of IPP is observed when the Si core size increases to 9 nm. Nevertheless, no obvious red-shift of the IPP is observed in the spectra.

### 5.2.2 The simulation model

In the corresponding simulation, we start with the simplest case, i.e., a shell-free single phase nanoparticle, from where we extend our discussion to core/shell nanoparticles, the EELS results of which has been obtained experimentally.

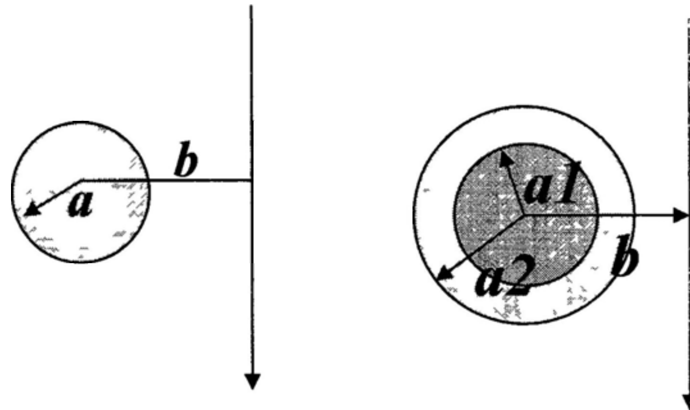


Fig.4 Schematics of the shell-free and core/shell nanoparticles

The schematics of the shell free nanoparticle and the core/shell nanoparticles are shown in Fig.4. In both cases, the impact parameter ***b*** is defined as the distance between the center of the nanoparticle and the incident electron probe. In the case of shell-free sphere, $a$ denotes the radius of the homogeneous particle, while $a_1$ and $a_2$ refer respectively to the core and the whole sphere radius in the core/shell structure.

The interaction between the incident electrons and the nanoparticle can be expressed in the following way: the incident fast electrons produce an original electromagnetic field in the vacuum, this in turn engenders an induced field at the sphere, the induced field then acts back upon the fast electrons, resulting in energy loss in them [30,32,33].

$$\Gamma^{loss}(\omega) = \frac{1}{c\omega}\sum_{l=1}^{\infty}\sum_{m=-l}^{l} K_m^2(\frac{\omega b}{\upsilon\gamma})[C_{lm}^M \operatorname{Im}\{t_l^M\} + C_{lm}^E \operatorname{Im}\{t_l^E\}] \quad (6.1)$$

$$t_l^{M,E} = \frac{-j_l(\rho_0)\alpha_l^{M,E} + [\rho_0 j_l(\rho_0)]'\beta_l^{M,E}}{h_l^{(+)}(\rho_0)\alpha_l^{M,E} - [\rho_0 h_l^{(+)}(\rho_0)]'\beta_l^{M,E}} \quad (6.2)$$

As the electron beam pass aloof the shell-free nanoparticle, the probability of specific energy loss is described in equation (6.1), in which $t_l$ is the scattering matrix as defined in equation (6.2). All multipole modes (as denoted by the quantum number $l$) have been included for simulation based on equation (6.1). The quantum number $m$ indicates the possible value of $l$ along the fast electron incident trajectory. $K_m$ is the modified Bessel function of order $m$ arising from the spherical wave and $\gamma = 1/\sqrt{1-(v/c)^2}$ accounts for the Lorentz contraction of the impact parameter $b$. $C_{lm}^E$ and $C_{lm}^M$ represent respectively the two expansion coefficients of the electric and the magnetic component when solving the Maxwell equations. $t_{lm}^E$ and $t_{lm}^M$ represent the scattering matrix of the electronic and the magnetic component accordingly in the Mie's scattering theory [6,74].

In describing the scattering matrix $t_{lm}^E$ and $t_{lm}^M$ in equation (6.2), $j_l$ and $h_l$ are

the spherical Bessel function and spherical Hankel function which characterize the spherical wave, and the prime denotes the differential with respect to $\rho_0$ . The superscript plus sign of $h_l$ means that the outgoing wave is taken into account. Other parameters in the scattering matrix depend on the dielectric function of the material and the geometrical size, which can be calculated separately.

### 5.2.3 Relativistic criteria for Si nanoparticle

In the STEM, the incident fast electrons can reach the value of $v/c = 0.6952$ at 200 kV acceleration voltage. The large velocity implies the relativistic corrections may need to be taken into account. Moreover, when the size of the specimen becomes comparable to the value of $c/\omega$, in which $\omega$ is the frequency of the excitation, the retardation effects become significant and may result in peak shifting of the plasmon oscillation and splitting [75]. Thus in order to make the calculated and experimental spectra comparable we firstly need to carry out the calculation both with and without relativistic treatment and find out whether it will bring in significant difference in the spectrum features.

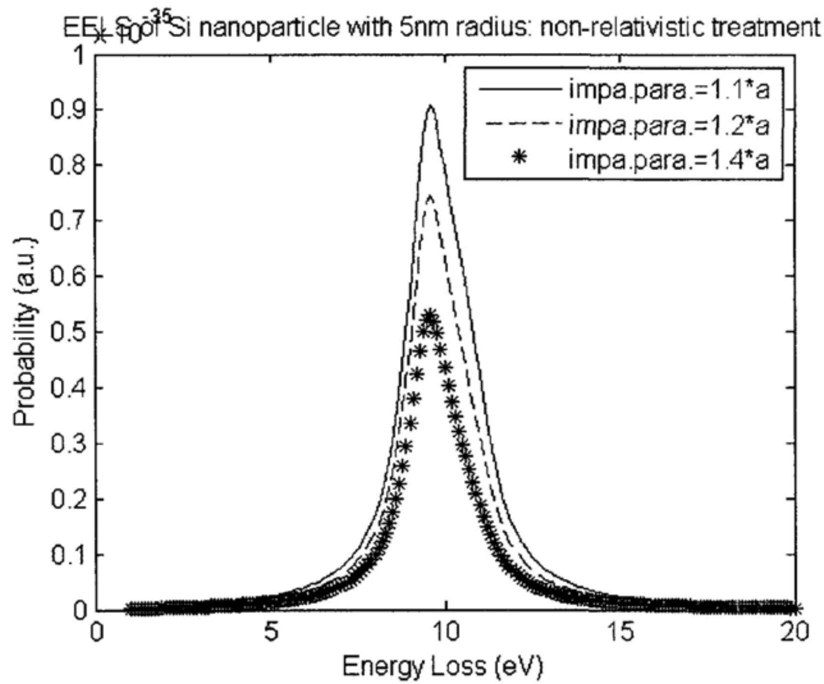


(a)

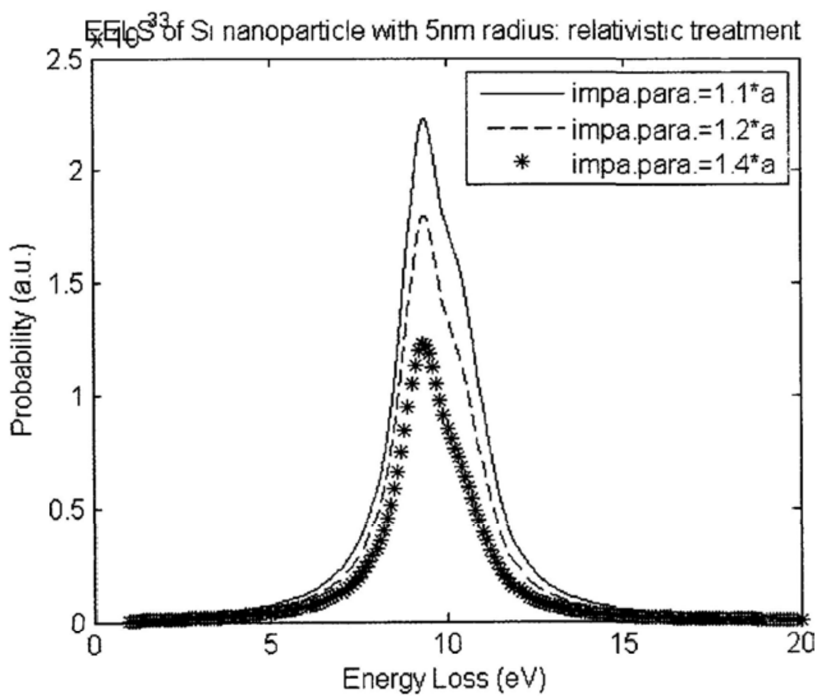


(b)

Fig.5 Comparison of EEL spectra with different impact parameter in a 5nm-radius Si nanoparticle

(a) without relativistic treatment; and (b) with relativistic treatment.

Fig.5 presented the calculated EELS result of a 5nm-radius Si nanoparticles, without (Fig.5(a)) and with (Fig.5(b)) the relativistic treatment. The incident fast electron energy is 200keV, being identical to that in the experiment. Besides the particle size, the impact parameter is another adjustable variable in both experiments and simulations. In both figures, the impact parameter changes from 5.5 nm to 7 nm, from the top to the bottom plots. The impact parameter change is found to cause only variation in the spectra intensity, being similar to the experimental observations. As similar results regarding the impact parameter change are also obtained for other particle sizes, we do not need to consider the effect of the impact parameter change in the later simulations.

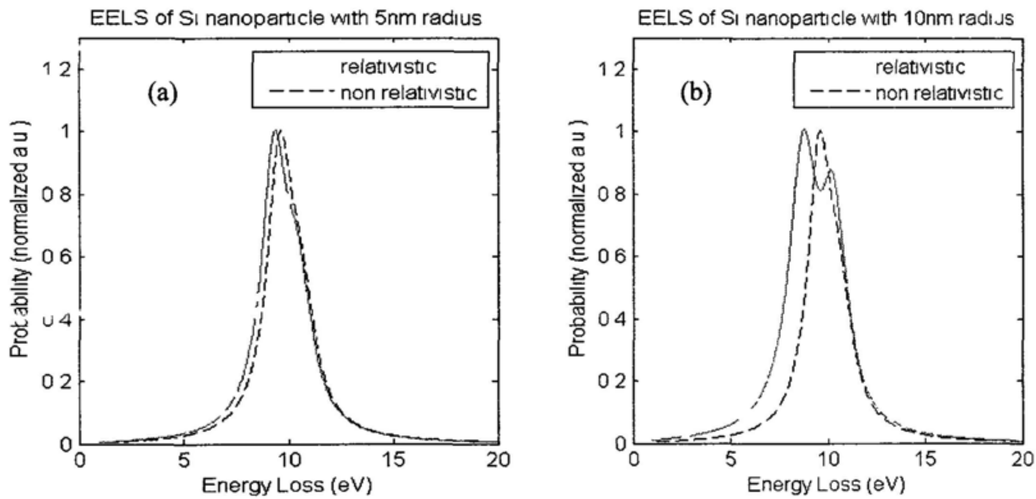

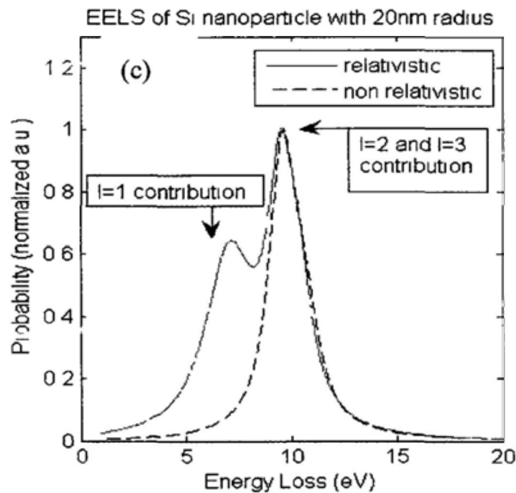


Fig. 6 EELS of (a) a 5nm-radius shell-free Si nanoparticle, with and without relativistic correction; (b) a 10 nm-radius shell-free Si nanoparticle; and (c) a 20 nm-radius shell-free Si nanoparticle. The dashed curves represent the non-relativistic cases and the solid lines for relativistic ones.

We have compared the simulated spectra of nanoparticles with different particle sizes without and with the relativistic effect taken into consideration (Fig.6). As the introduction of the surface oxidation layer ($SiO_2$) would complicate the situation, we use the shell-free Si nanoparticle in this simulation.

Here we summarize the results for $l = 1 \sim 3$. Higher order modes with $l > 3$ are not included because they contribute very little to both the intensity and the line profile of the spectrum. Fig.6(a) shows the EEL spectra of a 5 nm-radius Si nanoparticle, in which the solid line and dashed one indicate respectively the treatment without and with relativistic considerations. The EEL spectra of a ~10 nm and ~20 nm radius nanoparticles are presented in the same way, and can be found in Fig. 6(b) and 6(c).

When the particle is small (radius < 5nm), the simulated results with and without relativistic consideration are similar, i.e., only very little peak energy shifting is observed, which can be barely detected in the experimental EELS. The main contribution to the peak intensity in the simulated spectra comes from the $l = 1$ mode, which is the dipole mode. When the particle size increases from 5 nm to 10nm and then 20 nm, the spectra difference with and without the relativistic effect becomes obvious. Not only a general red-shift in the peak energy can be observed, but also the contribution from different $l$ modes leads to multiple peaks when relativistic effect is considered. It can be seen clearly in Fig.6 (b) and (c) the contribution from higher order mode increased compared to that from $l$=1 mode, and a red-shift of the overall peak position exists. The simulation results suggest that the relativistic effect induce spectra difference when the particle radius is larger than 5 nm. In the EELS experiments, most of the nanoparticles examined have the radius ranging from 5 to 20 nm. Therefore, the relativistic effect must be considered during simulation, in order to be comparable to the experimental results.

### 5.2.4 Simulation results and discussion

Drude model is usually employed in the simulation for simplicity to investigate the size criteria for relativistic consideration. While it is also possible to carry the simulation using the dielectric function of Si obtained experimentally.

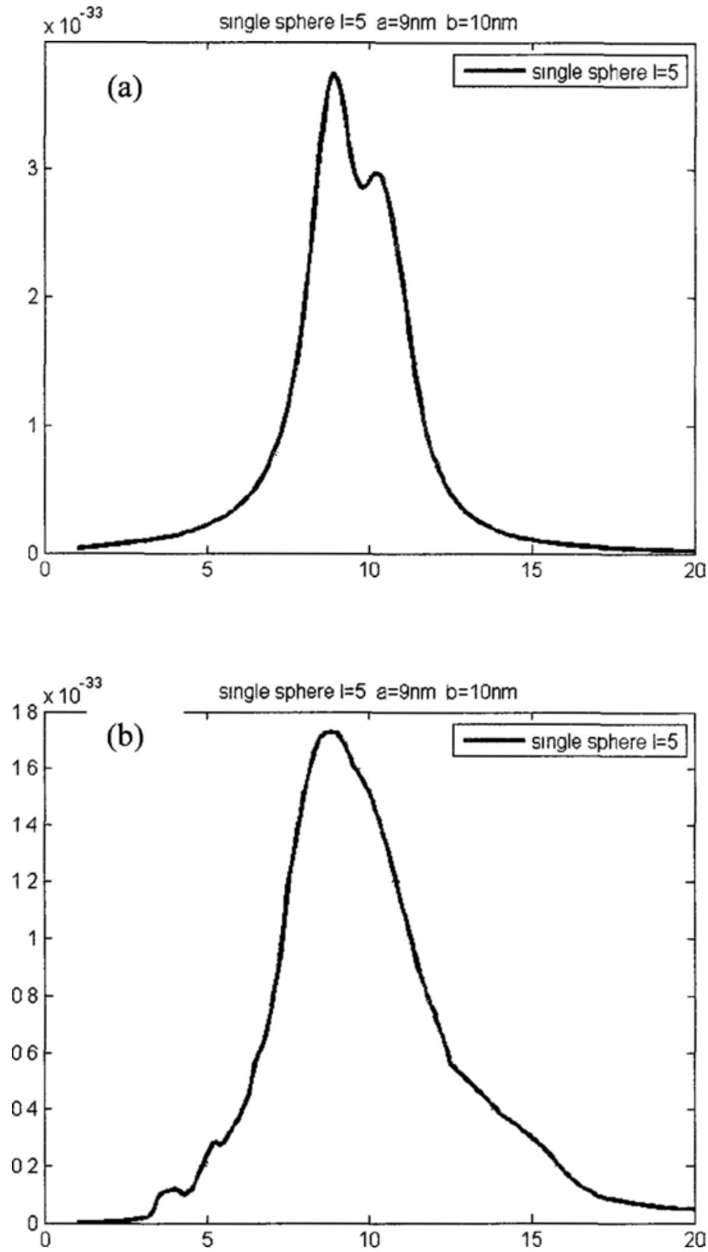


Fig.7 EELS in Si nanoparticle by using dielectric function obtained from (a) Drude model and (b) experimental measurement

Fig.7 shows the simulated results with Fig.7(a) taking the analytical dielectric function such as Drude model and Fig.7(b) using the experimental dielectric function obtained from optical measurement [29]. Both spectra were calculated using a 9 nm

radius shell-free Si nanoparticle, and the relativistic effect has been taken into account. Peak splitting is observed the in Fig.7(a), as resulted from different modes contributions. The simulated result in Fig.7(b) generally agrees with that in Fig.7(a), but the splitting can not be distinguished. This is due to the fact that the energy resolution has already been considered in the experimentally obtained Si dielectric function. We therefore choose to use the dielectric function of Si obtained from experimental measurement in later simulations.

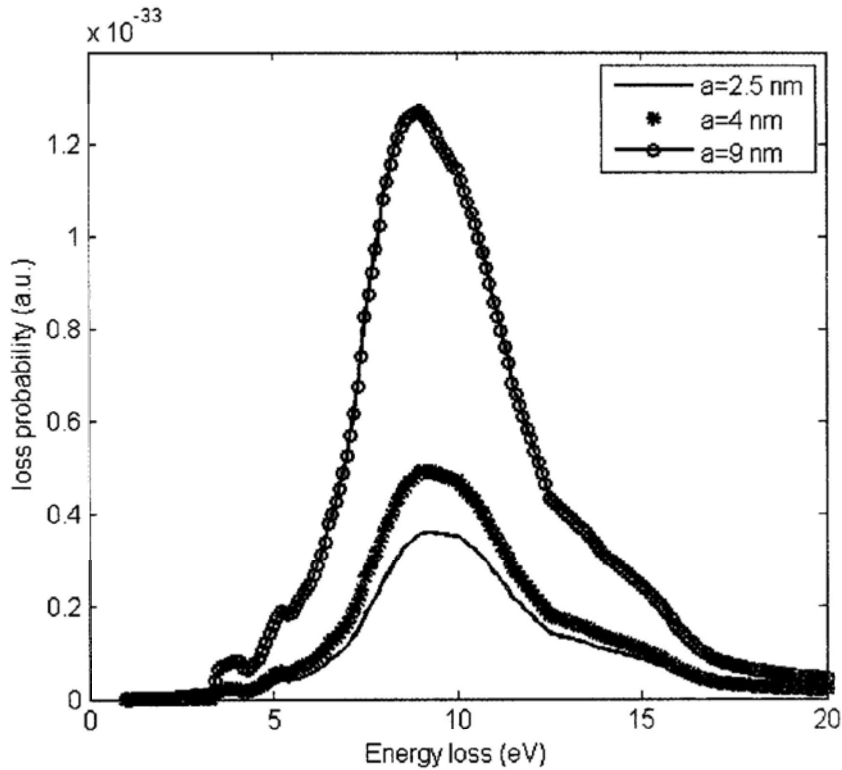


Fig. 8(a) calculated spectra of Si nanoparticles (shell-free particles)

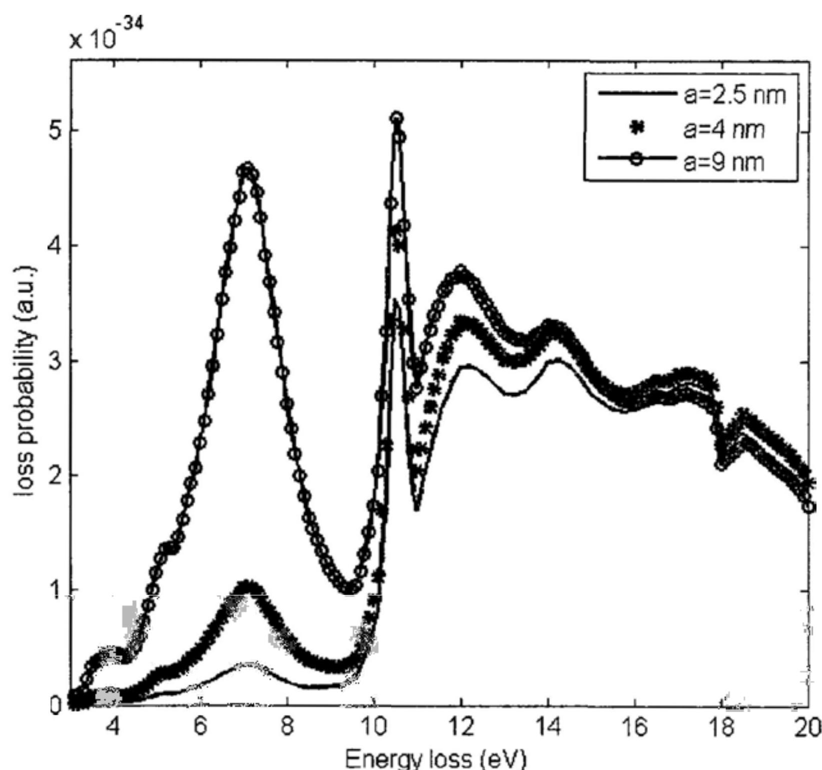


Fig. 8 (b) calculated spectra of Si nanoparticles with 6 nm thick oxidation layer ;

In order to illustrate the size effect of the Si core in the core/shell nanoparticle on the IPP, the simulated results for nanoparticles of three different sizes, i.e., 2.5 nm, 4 nm, and 9 nm in radius are shown in Fig.8. The results of shell-free particles were presented in Fig.8 (a), and those shown in Fig.8 (b) have considered a 6 nm oxidation surface layer (being consistent with the experimentally chosen nanoparticles in section 5.1.2.1). In the shell-free nanoparticles (Fig.8 (a)), little change of the surface plasmon peak can be identified when the radius of the nanoparticle increases from 2.5 nm to 9 nm. The relatively high oscillation frequency associated with the surface plasmon is ascribe to the absence of the surface oxide layer. One can see the IPP blue shifts to ~7 eV when the surface oxide layer is introduced during the simulation (Fig.8

(b)), being consistent with the experimental results. In all cases investigated, the change of the Si-core size seems to have little effect on the interface plasmon of the nanoparticle system. On the other hand, the introduction of a surface oxide layer do affect the IPP, and we will discuss it in the following section.

## 5.3 Effect of the $SiO_2$ shell thickness on the interface plasmon oscillation

### 5.3.1 Experimental results

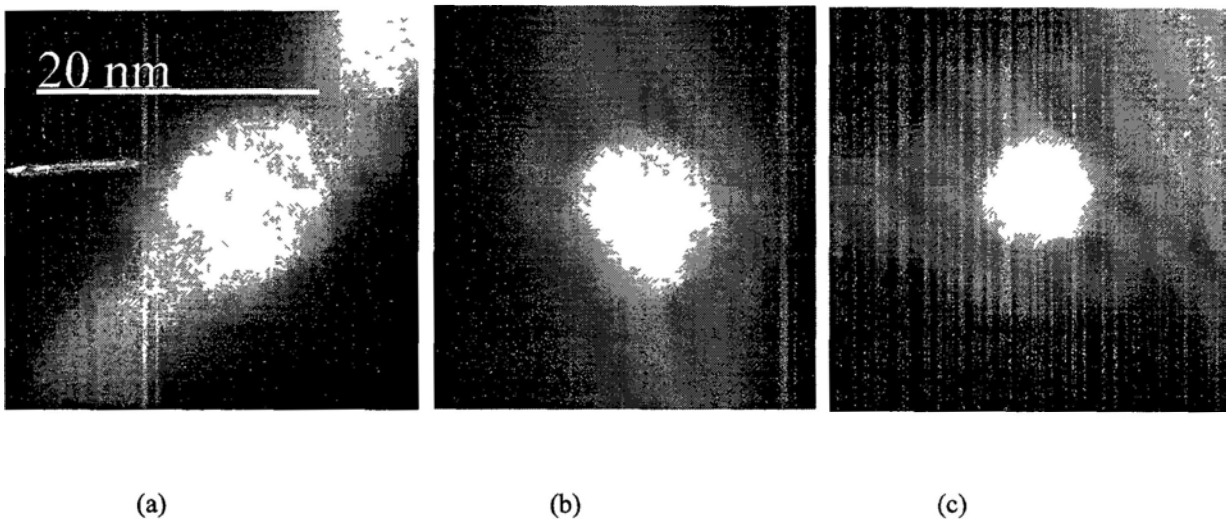


(a) (b) (c)

Fig. 9 Energy filtered TEM image of Si nanoparticles with similar core size of ~5 nm in radius, the shell thickness is (a) 1 nm; (b) 3 nm; (c) 5 nm;

In this section, the dependence of the EEL spectra of $Si/SiO_2$ core/shell nanoparticles on the shell thickness will be discussed. The EFTEM images of the specimen used in experiments are shown in Fig.9. The nanoparticles have similar Si core size of ~5 nm in radius while the $SiO_2$ shell thickness increases from 1 nm to 5 nm.

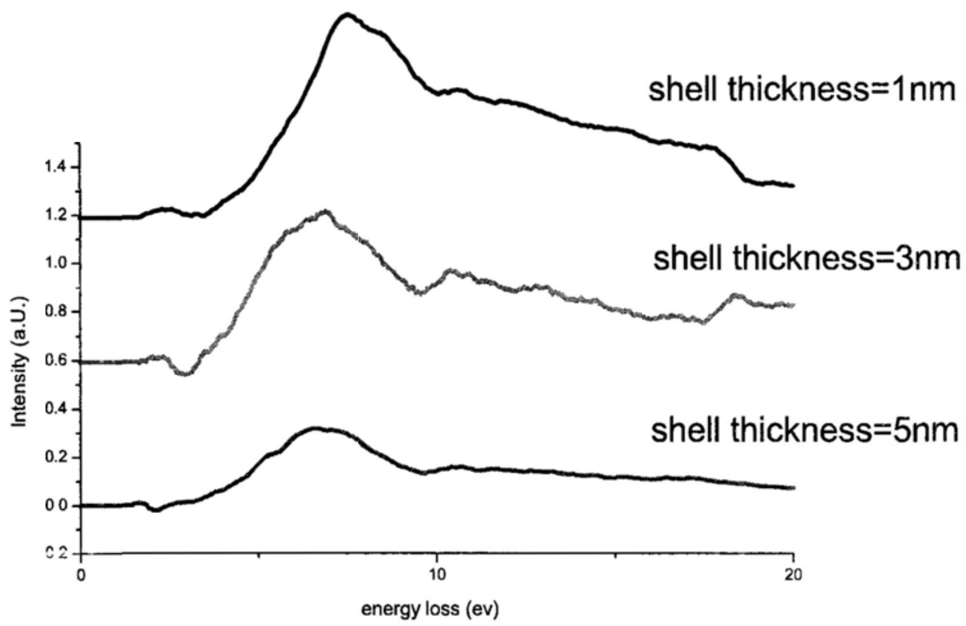


(a)

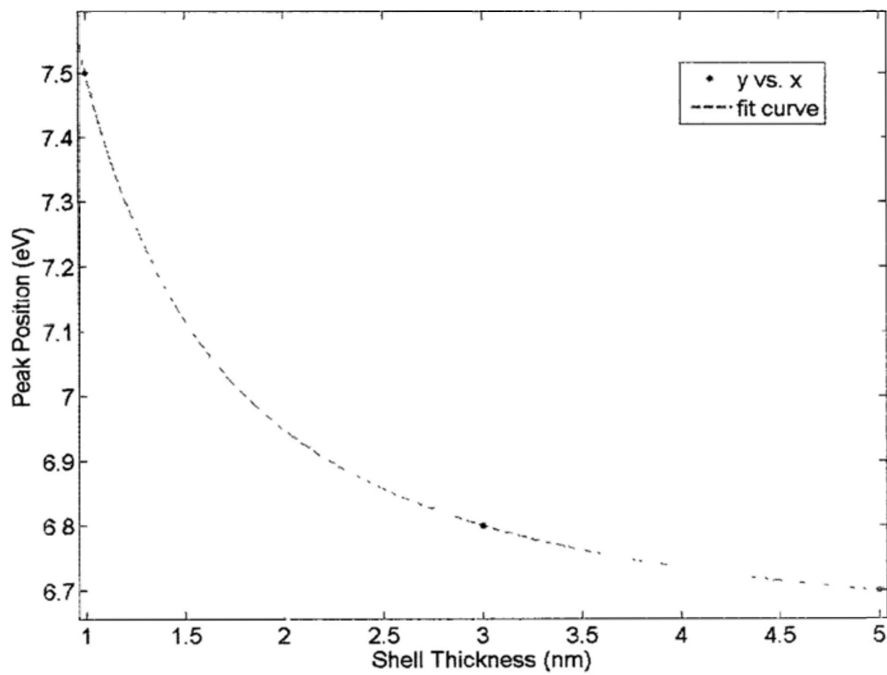


(b)

Fig. 10(a) experimental EELS of interface plasmon oscillation for 3 different samples (b) the peak position as a function of the shell thickness

The experimental data were taken in the EELS aloof mode, i.e., the electron probe was passing through the nanoparticles, but was located in the vacuum, being close to the surface of the particle. In this way, one can avoid the high intensity of the bulk plasmon peak and obtain better signal to noise ratio of the IPP. The EEL spectra of the three samples are shown in Fig.10(a), the IPP centered at ~8eV dominates spectra for all three sample alike. The IPP position is found to vary with the $SiO_2$ shell thickness, which is illustrated in Fig.10(b). As the shell thickness increases from 1 nm to 3 nm, obvious red-shift from 7.5 eV to 6.8 eV is observed. Further increase in the $SiO_2$ shell thickness only causes small reduction on the IPP energy, which is barely discernable.

### 5.3.2 Simulation results and comparison with experimental ones

In this section in order to investigate the effect caused by the different shell thickness we calculate the EEL spectra by fixing the core radius of the Si nanoparticle as 5 nm, and change the shell thickness from 0 nm (shell-free particle) to 20 nm (very thick oxidation layer). The simulation model is based on the one described in section 5.2.2 with relativistic effect considered.

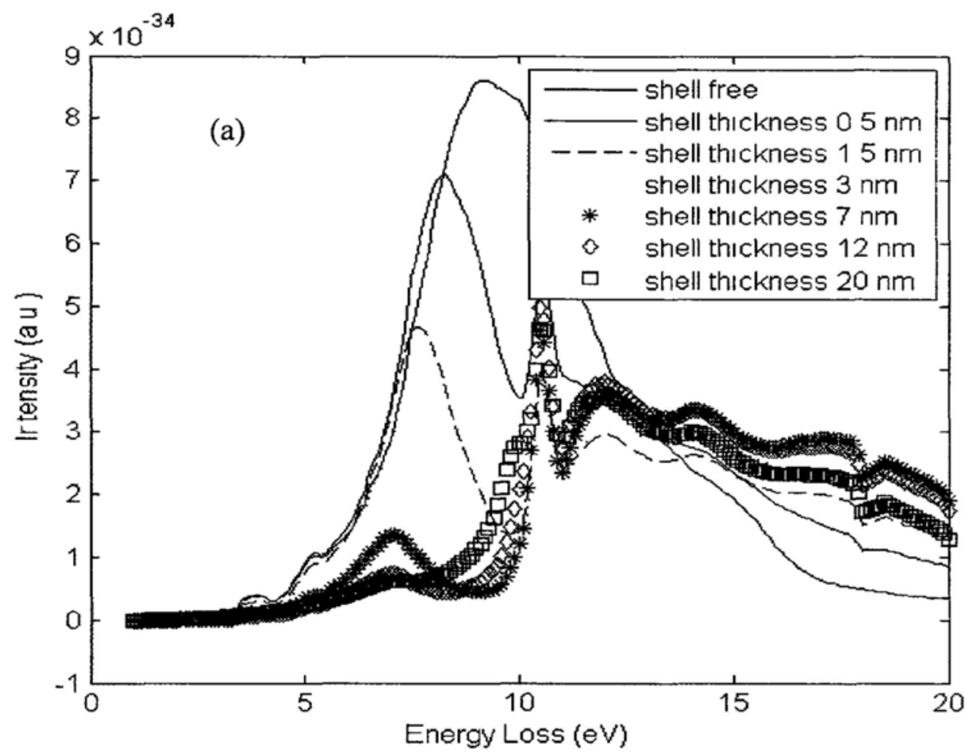


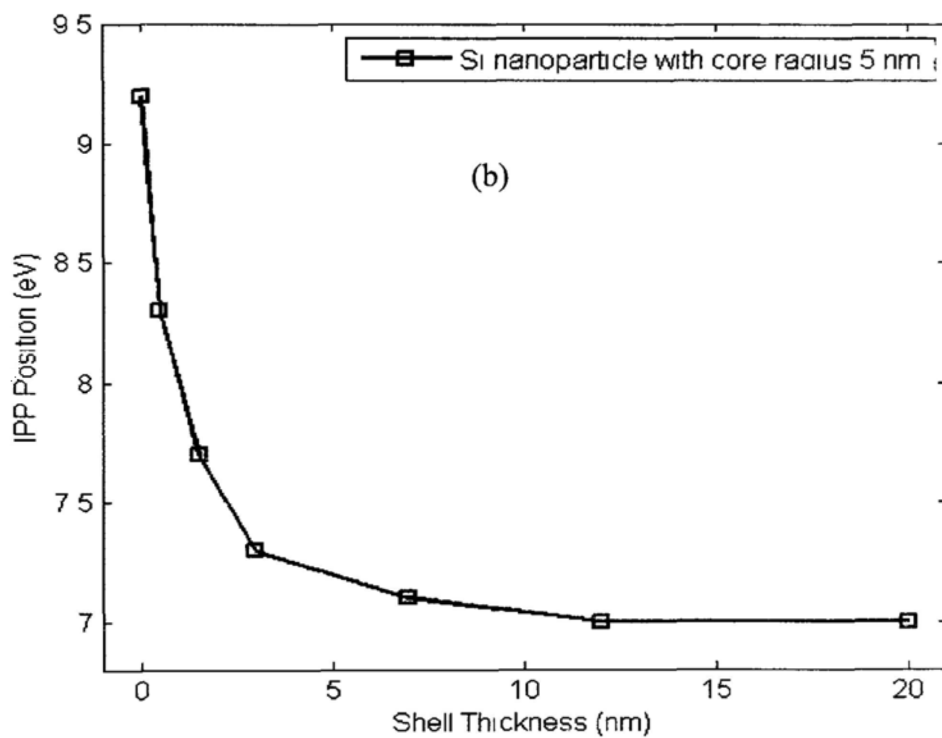


Fig. 11(a) calculated EEL spectra in Si nanoparticles of core radius 5nm (b) IPP position as a function of shell thickness

Fig.11(a) shows the calculation results of a number of core-shell particles with shell thickness ranging from 0 to 20 nm. The plot represents the spectra of nanoparticles with increasing shell thickness from top to bottom. In the shell-free particle, the IPP centered at 9.1 eV is the main feature in the EEL spectrum. For nanoparticles with a $SiO_2$ shell, features above 9 eV appears other than the IPP, mainly originated from the interband transition of $SiO_2$. Red-shift in IPP is obvious for thin $SiO_2$ layer thickness. A more clear evolution of the IPP with the $SiO_2$ shell thickness is shown in Figure 11 (b), in which the IPP energy position is plotted as a function of the $SiO_2$ layer thickness. For $SiO_2$ shell thickness smaller than 3 nm, the IPP energy is found to drastically increase with the shell thickness decrease. Nevertheless, further increase in the shell thickness cause little shift in the IPP energy, which levels off as shown in Figure 11 (b). Such a trend is consistent with the experimental observation.

### 5.4 Conclusion

One can see that the simulated IPP energy position does not match perfectly with the experimental ones (IPP position red shift from 8 eV to 7 eV in the simulation while from 7.5 eV to 6.7 eV in the experiment), this may be ascribed to two factors:

1. Simulation suggests that small variation in the shell thickness will cause the significant change in the IPP energy position. However, in the experiments the spatial resolution in the EFTEM mode determines a relatively large measurement error of ~1 nm for the $SiO_2$ shell thickness value.

2. The imperfect geometrical configuration of the nanoparticles (i.e., shape of the nanoparticles deviate from perfect spheroid). As will be discussed in the following chapter, geometrical configuration of the nanostructure will have a profound effect on the IPP.

# Chapter 6. Interface Plasmon Excitation in Si/SiO2 Core/Shell Nanostructures with Different Geometrical Configurations

It is known from the research work on the metal nanorods/nanowires that tuning the surface/interface plasmon energy are available via varying the material aspect ratio (length/diameter ratio)[15,76,77], and the field enhancement is found more efficient at some "hot spots" in specific nanostructure, such as tips and inter-region of the particles[78,79]. It is therefore of great importance to understand the evolution of the excitation of surface/interface plasmon as a function of the aspect ratio change in 1D $Si/SiO_2$ core/shell nanostructures, as well as the spatial distribution of the IP modes in those nanostructures.

To investigate the questions above, techniques besides conventional optical methods can detect the plasmonic properties with sufficient spatial resolution are highly expected. The work done on Ag by EEL spectroscopy reveal that the SP/IP excitation can be investigated within a broad energy range, such as near infrared/visible/ultraviolet domain, with the spatial resolution down to nanometer scale. Simultaneously the imaging technique related with EELS, such as Energy Filtered TEM/STEM (EFTEM) and spectrum imaging, also provide the way of

mapping the localized excitations over individual nanoparticle with better spatial resolution than conventional optical ones.

In this chapter, the energy evolution of the SP/IP in one dimensional $Si/SiO_2$ core/shell nanostructures with different aspect ratios and size will be investigated by EELS measurement. Then the spatial distribution characters of the SP/IP modes are studied by employing EFTEM imaging, which can provide a quick visualization of the eigenmodes of SP/IP among nanostructures with large field of views and less irradiation damage to the samples. Based on the experimental observations the physical interpretation is discussed. The spatial distribution of different SP/IP modes are compared, and possible influences of retardation effect in long nanostructures are also studied. The simulations on the long nanowire were carried out, and we also found the validity in explain the comparison between experimental and theoretical results.

## 6.1 The evolution of EEL spectra in the Si/SiO2 core/shell nanostructures

### 6.1.1 Comparison of the general features in EEL spectra between different nanostructures

The Si based 1D nanostructures are synthesized via thermal evaporation of SiO powder in a high temperature tube furnace. The Si nanostructures with different morphologies, which are covered with $SiO_2$ shell, are formed during the cooling process in different temperature zone of the furnace. Specifically, nanoparticles are

mainly formed at 1100°C, and the particles' diameters are around 25±10 nm. The nanowires are collected at 1000°C with diameter 30±10 nm, and at 900°C with diameter 20±10 nm. EELS measurements were carried out in a TEM (Hitachi HF 3300) attached with a GIF (Tridiem™) with ~0.5 eV energy resolution. By applying relatively parallel beam illumination, the EEL spectra in this study are acquired from an area selected by an area selecting slit on individual Si nanostructures (see Chapter 4). The spatially resolved SP/IP mappings are obtained by employing EFTEM imaging, with a 2 eV energy selecting slit centered at the specific energy positions, for example ~16.5 eV, ~4.5 eV and ~8 eV, corresponding to the Si bulk Plasmon, longitudinal, and transverse Plasmon polarizations, respectively (Details can be found in later sections).

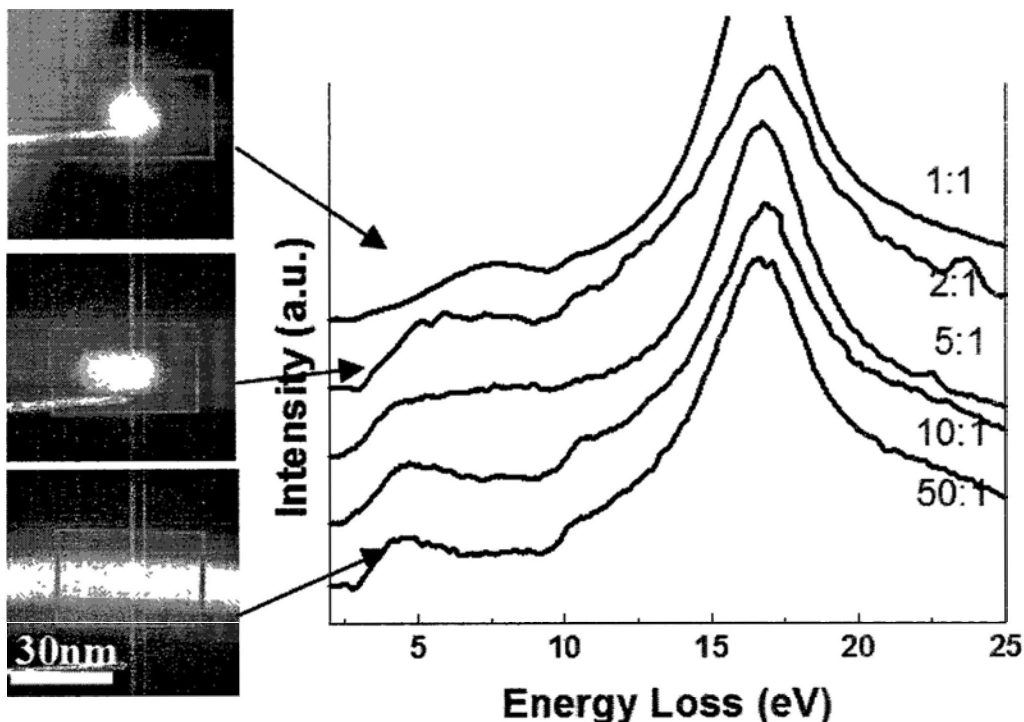


Fig. 1 comparison of the EELS spectra between different Si nanostructures with EFTEM imaging taken at the Si bulk Plasmon loss

The EFTEM images and EEL spectra are taken from three different specimens of distinct morphology, as shown in Fig.1(b). The spectra are taken from the rectangular area in the $Si/SiO_2$ core/shell nanostructures with different aspect ratios, i.e., from nanospheroid (aspect ratio is ~1), to rod-like structures with different aspect ratios (aspect ratio is ~2 to 10), and to long nanocable (aspect ratio is >50). The influence from the zero loss peak was removed by applying power law. Three EFTEM images (using Si bulk plasmon energy) are selected to illustrate that the diameter of the Si-core (15 nm) and the $SiO_2$ shell thicknesses are similar (~10 nm) for the nanostructures studied. The dominant peak at ~16.9 eV originates from the Si bulk plasmon, which remains unchanged in different nanostructures. While the peak features at lower energy range (i.e., 3-10 eV) are found varying with the aspect ratio. For the $Si/SiO_2$ core-shell nanospheroid (the upper specimen), a single peak centered at ~7.8 eV can be clearly observed. Broadening of such a peak and a simultaneous red shift occur when the nanostructure aspect ratio increases to 2/1. Further increasing the nanorod's aspect ratio leads to the splitting of the ~7.8 eV peak into two, with the slightly blue shift of the higher energy branch, and a significant red-shift of lower energy branch, and finally reaches ~8.2 eV and ~4.2 eV in the case with extremely large aspect ratio such as long nanocable. In addition, the intensity of the lower energy branch increases greatly as the aspect ratio increases, while the opposite trend happens to the higher energy peak, leading to the dominance of the ~4.2 eV peak in the long nanocable.

### 6.1.2 Longitudinal mode and transverse mode

The localized SP/IP excitations in nanostructures such as nanorods and nanowires are different from those excited in spherical configuration (discussed in the last chapter). Elongation of the nanoparticle to rod-like or wire-like structures would lead to different induced charge distributions along the short and long axis in the external electrical field, forming transverse and longitudinal SP/IP oscillations with different characteristic frequencies. In general, the oscillation energy depends on the charge separations along the specific axis, the longer charge separation will result in lower excitation energy or vice versa.

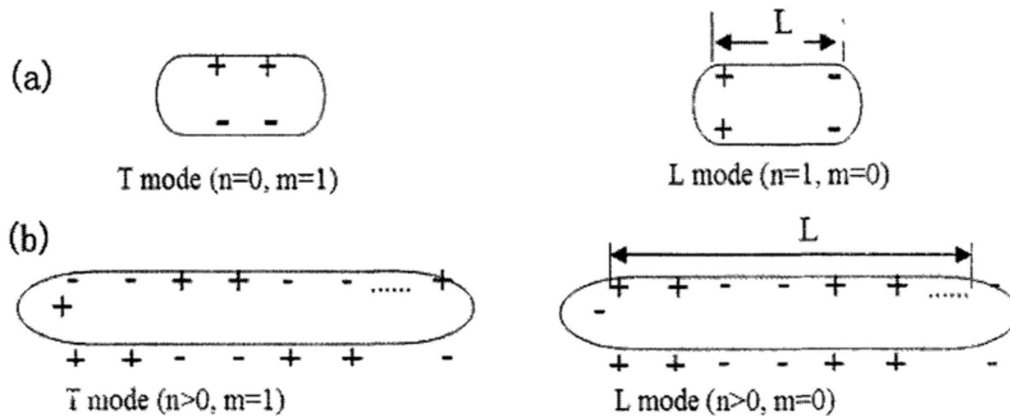


Fig.2. The schematic description of the charge distributions in the nanorod (a) transverse (T) modes with n=0, m=1 and longitudinal (L) modes with n=1, m=0. (b) For long nanocable, the n>0 modes are excited

For nanostructures in the scale of $q \cdot a < 1$, dipole like charge distribution is predominant, the schematic description in the nanorod or nanowire is illustrated in

Fig.2. To describe the transverse and longitudinal SP/IP modes (the charge distributions in different directions), two sets of numbers are used, i.e., (n=0, m=1) for the transverse and (n=1, m=0) for the longitudinal, where n is the longitudinal charge modulation number, and m the azimuthal number. Under such dipole approximation, one can see that when the length of the nanorod increases (while diameter unchanged), the charge separation along the longitudinal direction would increase, resulting in the decrease in the longitudinal SP/IP energy. As a comparison, one shall expect little change in the energy of the transverse SP/IP mode, as elongation of the nanorods does not affect much the charge separations in its transversal direction. This can serve as a qualitative explanation for the experimentally observed SP/IP energy in Fig.1, in which the 4~6 eV mode is attribute to longitudinal mode in the axial direction, and the 8 eV mode is attributed to the transverse one in the radial direction. The calculation results for the evolution from nanoparticle to nanowire will be illustrated in the following section, using Gans theory[12].

The oscillation frequency $\omega_m(q)$ of the surface/interface plasmon can be obtained by setting the denominator of the surface response function $\mathrm{Im}(\gamma_m)$ to zero, with specific boundary condition satisfied[72] . $\mathrm{Im}(\gamma_m)$ describes the surface excitation features in a loss spectrum for object of a given radius in the cylindrical configuration:

$$\gamma_m(q,\omega) = \frac{1}{qa[\varepsilon_1 I_m'(qa)K_m(qa) - \varepsilon_2 I_m(qa)K_m'(qa)]} \quad (6.1)$$

in which $q$ is the scattering wavevector and $a$ is the radius of the nanowire. $\varepsilon_1$

and $\varepsilon_2$ are the dielectric functions of the Si and the surrounding $SiO_2$. $I_m$ and $K_m$ are the modified Bessel functions, the prime indicates the derivative with respect to the corresponding arguments. The boundary condition [20,52,58] can be expressed as

$$L_m \varepsilon_1 + (1 - L_m)\varepsilon_2 = 0 \qquad (6.2)$$

in which $L_m = qaI'_m(qa)K_m(qa)$.

The frequency of the SP/IP $\omega_m(q)$ can then be written as

$$\omega_m(q)^2 = qa[I'_m(qa)K_m(qa)\omega_{p1}^2 - I_m(qa)K'_m(qa)\omega_{p2}^2] \qquad (6.3)$$

in which $\omega_{p1}$ and $\omega_{p2}$ represent the bulk plasmon excitation frequencies of Si and the surrounding $SiO_2$. As $m$ represents the athmuzal number, all possible $m$ value will contribute to the spectrum. Nevertheless, when considering specific geometrical configurations, such as thin vs. thick nanowires, one may select specific $m$ values to make corresponding approximations. Figure 3 (a) and (b) shows an example of the surface response function of Si as a function of $qa$ and $\omega$ when m is taken as 0 and 1, respectively.

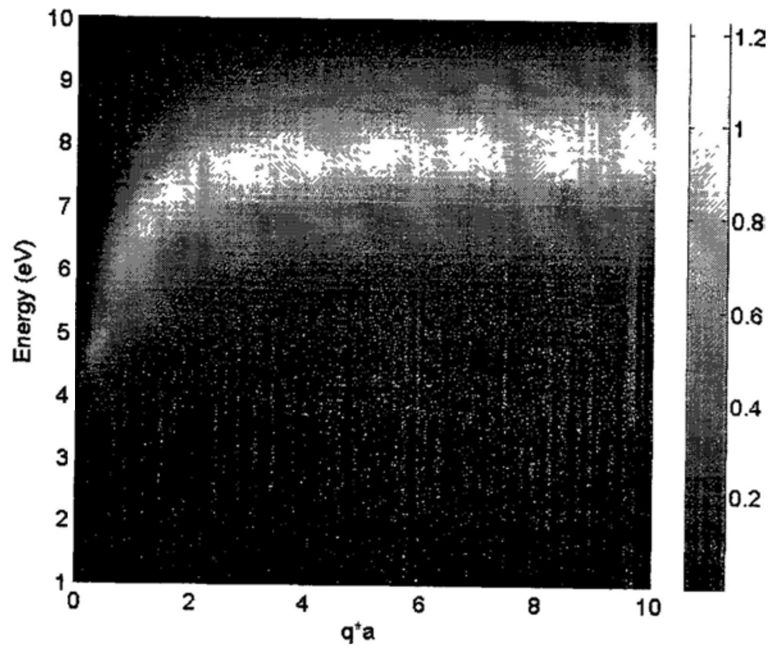


(a)

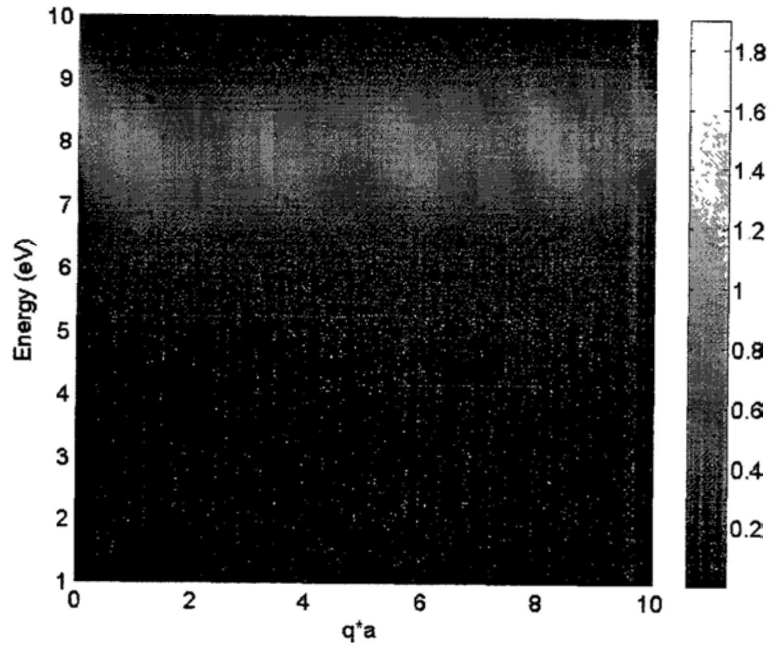


(b)

Fig.3 surface response of Si nanowire for (a) m=0 mode and (b) m=1 mode

Under the dipole approximation the distance between the charges in the dipole is supposed to be much smaller than the wavelength of the excitation, which means $a < \lambda \sim \frac{1}{q} = \frac{v}{\omega}$. This is to say, when $qa < 1$, the dipole approximation is valid, while in the case of $qa >> 1$ the surface charge density will be complicated .

In Fig.3(a) the surface response function (image part of equation (6.1)) is plotted as functions of $qa$ (horizontal axis) and frequency $\omega$ (vertical axis, here we use the energy value $\hbar\omega$ to indicate the real frequency $\omega$), while *m*=0. The gray level in the plots indicates the intensity variation which is illustrated by the level bar on the right. The dielectric function of Si was adopted from optical experiment [29]. In the *m*=0 mode, there is only one excitation observed, which disperse significantly with *qa*; while in the *m*=1 mode, this is also one mode, which does not disperse with *qa*. Combine the results from Fig.3(a) and (b), one shall then expect to see two excitation(~5 eV and ~8 eV) in the case of small *qa* (<1), corresponding to the longitudinal (m=0) and transverse (m=1) oscillations as observed in Fig. 2. (In our experiments, the specimens of the nanowires are around ~10 nm in radius or thinner. As for the surface/interface excitations below 10 eV, the *qa* value is <1. )

### 6.1.3 the evolution of EEL spectra as a function of aspect ratio and retardation effect

To understand the evolution of the two IP modes as the nanostructure aspect ratio varies, the Gans theory[12] is used in simulation. As is known that the Gans theory is

the extension of Mie theory for spherical particles, and it describes the extinction characteristics of elliptical/elongate particles using a dipole approximation. It is usually employed to simulate the dependence of the SP/IP mode on the aspect ratio of elongated particle with size much smaller than the excitation wavelength in optics. By applying the dielectric functions of Si and $SiO_2$ as the target and surrounding materials, the optical extinction is plotted as a function of 1/aspect ratio in Fig.4.

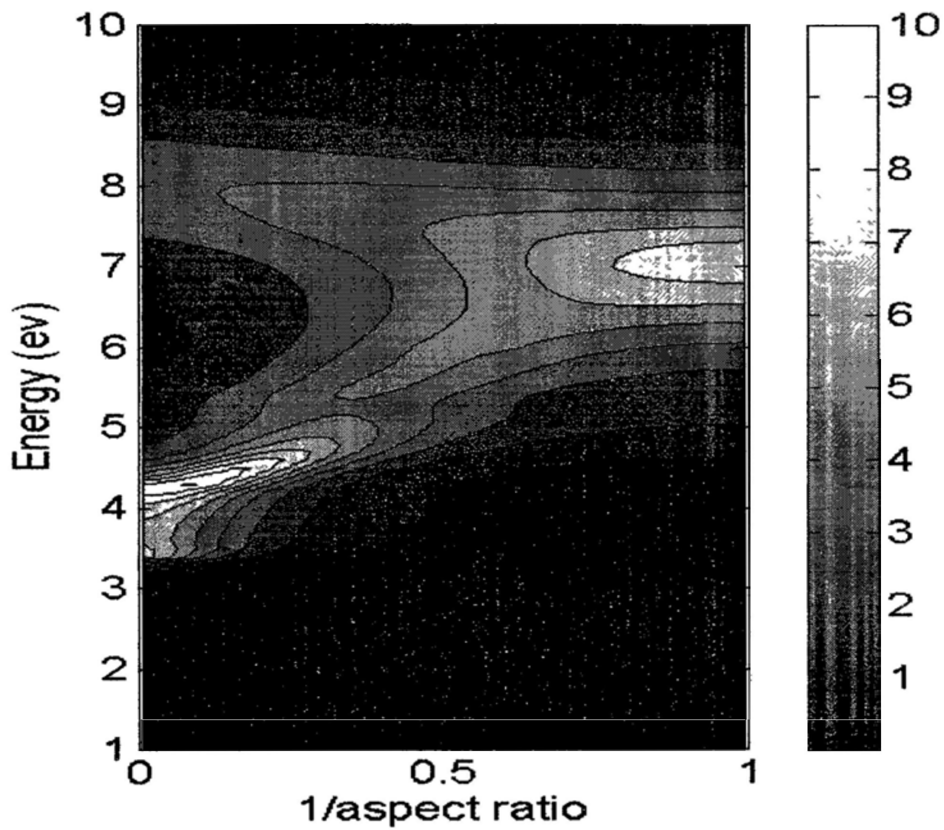


(a)

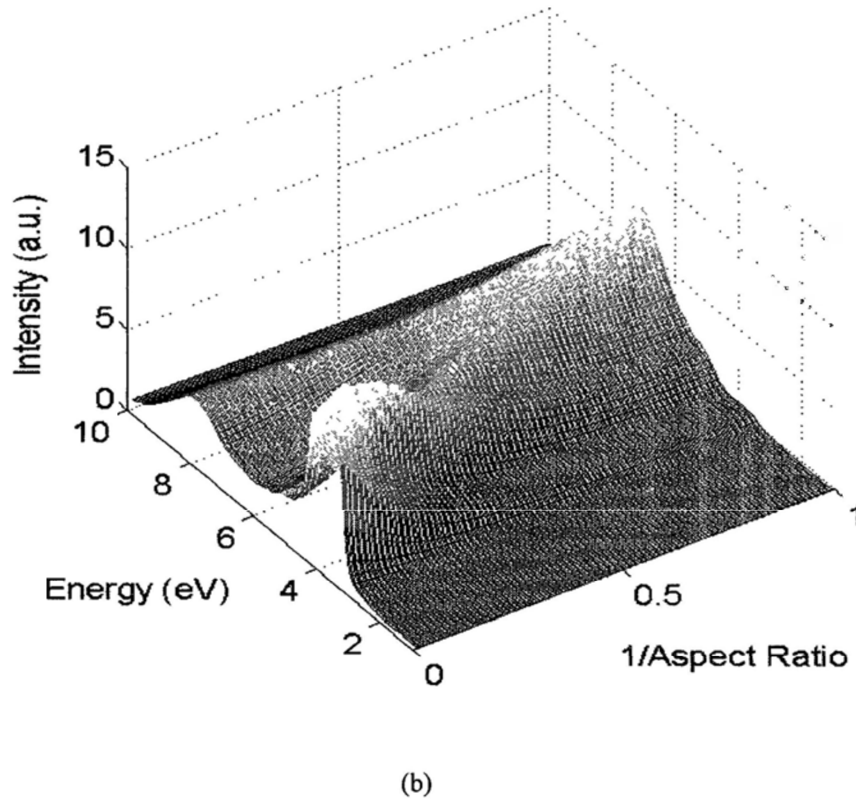


(b)

Fig. 4. The plots of the extinction spectra for $Si/SiO_2$ nanorod with different aspect ratios

(a) contour plot; (b) intensity plot;

The single peak at ~7 eV is observed for the nanostructure with aspect ratio around 1, and such a peak split into two branches which further shift toward ~4 eV and ~8 eV as the aspect ratio increases from 1 to infinity. It is has been reported that the simulation using Gans theory can show great agreement with the experimental optical extinction results for metal nanorods [76,77]. Here, the consistency between the EELS and the optical simulation is also observed, as the results in Fig.3 agree with the experimental spectra in Fig.1 . Nevertheless, the dipole approximation is valid only when the nanoparticle of small size, both the diameter and the length of the nanorods is much smaller than the excitation wavelength. In practical case, as the nanorod

length increases the retardation effect [75] will be induced thus the dipole approximation might be invalided in the interpretation. The retardation effect will introduce periodical charge modulations of opposite charges in the longitudinal direction of a thin nanocable when its length exceeds the electrostatic limit. As a result, additional dipole oscillations with shorter charge separations (than the length of the rod) are also excited along the nanocable's longitudinal direction, and $n$ can take a series of values greater than 0. An example of such configuration is sketched in Figure 2(b), in which the azimuth number $m$=0 (i.e., monopole mode) represents a uniform charge distribution across the transversal plane and $m$=1 is a dipole like charge distribution on the same plane. The overall longitudinal mode in such an nanocable is then obtained by summation of all charge oscillations with $n$=1,2..N. Despite the fact that $n$>1 modes may produce oscillations with higher energy, their intensity are less intense than that of the $n$=1 mode. This is because the higher order ($n$>1) modes have smaller dipole moments than the dipole mode. Consequently, the retardation effect does not impose significant changes on the IP peak energies, but may cause subtle difference in the spectrum line shape.

### 6.1.4 spatial distribution of the SP/IP excitation with different aspect ratio

The spatial distributions of different Plasmon modes are then investigated by EFTEM imaging technique. In Fig. 4, the images are taken using Si bulk Plasmon (black and white images) and the SP/IP excitations (color images) from nanospheroid, nanorod and nanowire. In the experiments a 2 eV width slit centered at specific

energy losses is employed.

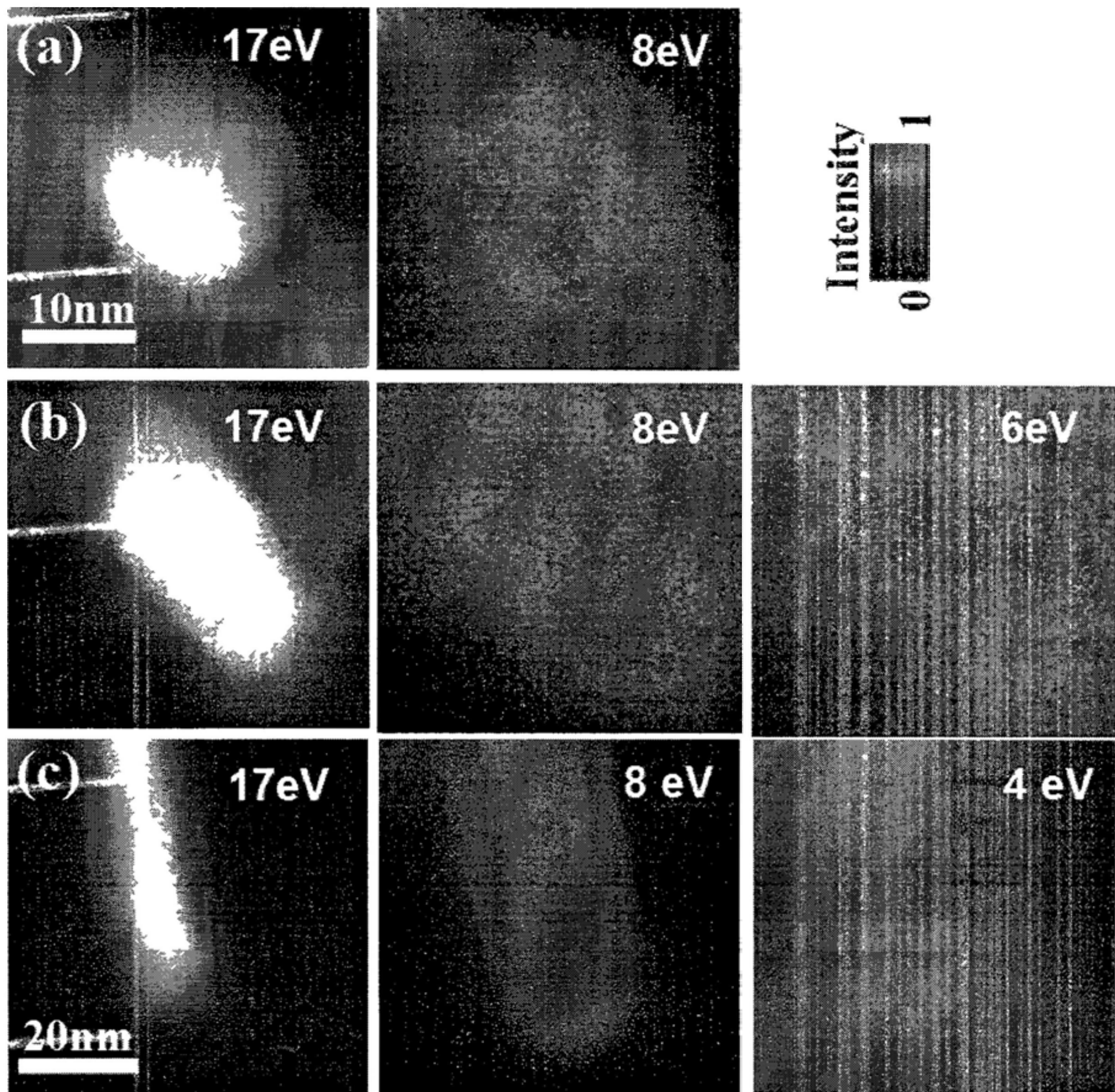


Fig. 5 The EFTEM images of core/ shell Si/$SiO_2$

(a) nanosphere (b) nanorod and (c) nanocable

In Fig. 5(a), the 8 eV EFTEM image of the nanospheroid particle illustrates that the intensity are found isotropically distributes among the particle, indicating the ~8 eV SP/IP mode are excited from the spherical Si/$SiO_2$ interface with symmetrical excitation probability. As a comparison, in nanorod (Fig.4 (b)), the spatial characters

of the two SP/IP modes are inhomogeneous: the 8 eV mode exhibits higher intensity at the Si/$SiO_2$ interface along the short axis and the 6 eV mode mostly resides on the two ends of the nanorod along the long axis. For the nanocable in Fig. 4 (c), similar spatial character is found for the transverse SP/IP modes at ~8eV with that observed in the nanorod. Nevertheless, a rather uniform intensity distribution is observed for the longitudinal SP/IP mode (at ~4eV) along the entire Si nanowire, instead of concentrating on the tip region.

The transverse nature of the ~8 eV excitations in both the nanorod and nanocable is clearly demonstrated by the intensity distribution of such IP mode, as seen in the corresponding EFTEM images. The observation that the ~6 eV excitation in the short nanorod intensifies at the two ends along the long axis agrees well with the dipole approximation (as in Fig. 2(a)), and discloses its longitudinal nature. On the other hand, the uniform intensity distribution of the ~4 eV excitation in the long nanocable is also consistent with longitudinal characteristic, which is due to the periodical piling up of opposite charges along the nanocable long axis as a result of the retardation effect.

## 6.2 Interface plasmon oscillation in Si/$SiO_2$ core-shell nanocables of different diameter

In this part, the EELS study of the long Si/SiO2 core/shell nanowires (thin wires and thick wires) will be discussed in detail, the experimental results will be

demonstrated firstly, then simulation model is given and some of the calculation results are used to interpret corresponding experimental results.

### 6.2.1 General features in EEL spectrum for Si/$SiO_2$ nanocable

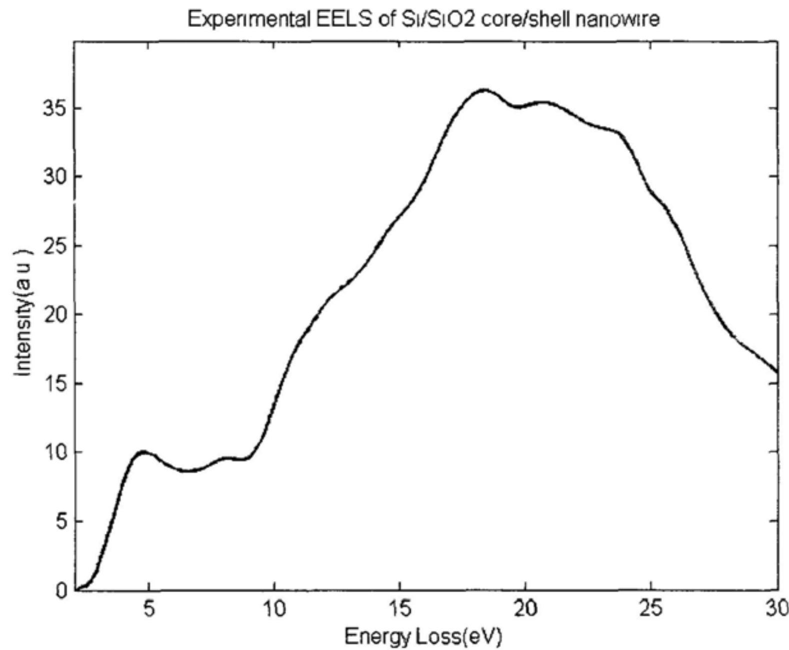


Fig.6 experimental EEL spectrum in Si/SiO2 core/shell nanowire

After ZLP (zero loss peak) subtracting Fig.6 shows a typical EEL spectrum taken near the center region of the Si nanowire, in which the electron beam incident on the nanowire perpendicularly. In the spectrum the bulk plasmon excitation of Si ~17 eV and SiO2 ~23 eV can be distinguished clearly and a weak surface/interface excitation ~8 eV presence as well, which is similar to the case in the nanoparticle structure. While an additional IPP peaks at ~ 4.5 eV indicates another excitation mode which is different from that in the previously cases. In the following sections the investigation will focus on how these two IPPs can be affected by the diameter of the nanowires.

### 6.2.2 Experimental EELS results with different Si core size

The specimens used in the experiments consist of the Si nanowires with different radius coated by $SiO_2$ oxidation shell. The spatially resolved EELS is employed to collect the spectra, which is same as the one introduced in chapter 4. The rectangular spectra collection area is indicated in Fig.7.

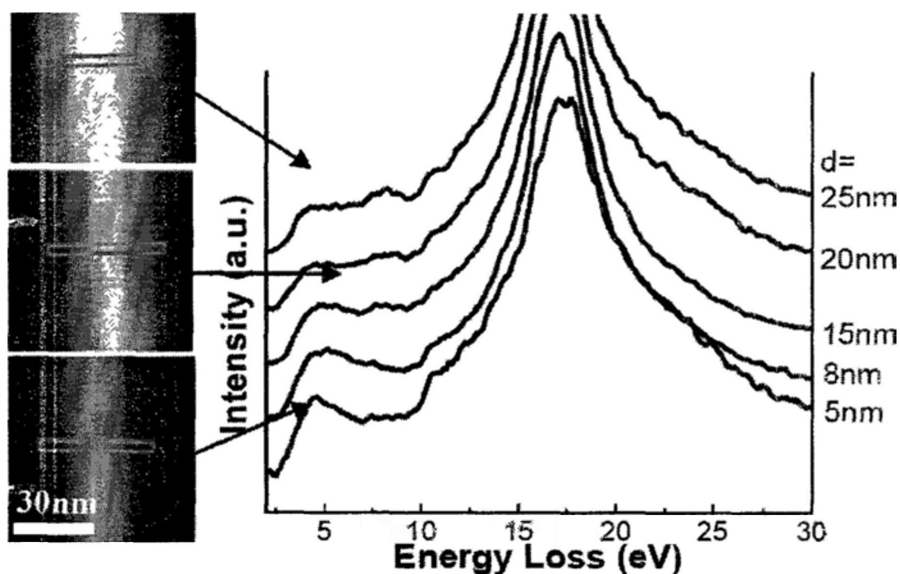


Fig.7 series of EEL spectra taken from the rectangular area in the EFTEM images, from the bottom to the top, the Si core diameter changes from 5 nm to 25 nm separately

The experimental results are shown in the figure above, the three images in the left show the EFTEM images of the specimens under investigated. By integrating the energy loss intensity along the y-direction for a chosen pixel size in the spectrum image (see Chapter 3&4), we can reproduce the spatially resolved EEL spectra from the corresponding area of interests (the rectangular boxes in the EFTEM images). The background of the ZLP is subtracted by using power law. When the Si core diameter < 10 nm, the ~4 eV mode is predominant in the low energy region with a very weak

feature of the ~8 eV IP mode. As the diameter of the Si core increases, the intensity of the two peaks become comparable, the further increase of the core size lead to the reverse of the intensity ratio of the 4 eV/8 eV.

### 6.2.3 Simulation results with different Si core size

We compare the simulated spectra between thin and thick wire, in which we can see how the change of the diameter of the nanowire would contribute to the spectra features.

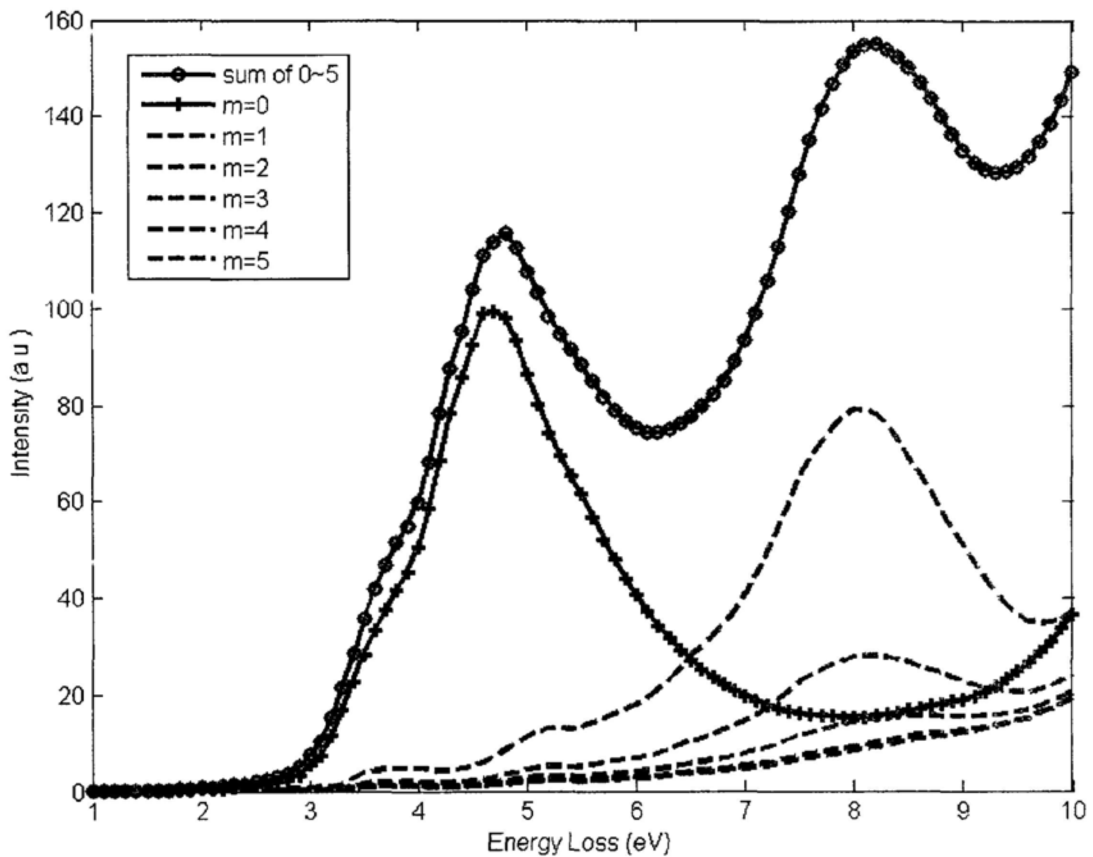


Fig. 8. The simulations of EEL spectra, contribution from m=0 mode (black cross) and from a summation of m=0 to 5 modes (black circles), the contribution from discrete mode of 1 to 5 is plotted in dashed line, from top to bottom

Fig 8 shows the results of the simulated EEL spectra of Si nanowires. In the figure the total spectrum is composed of transverse modes (~8 eV) and longitudinal mode (~4.5 eV) separately. The ~4.5 eV peak feature (can be described using $m$=0), is dominant in thin nanocables [18,19], which corresponds to a uniform charge distribution across the cylindrical surface in the longitudinal direction. In long and thin nanowires, such a mode should make dominant contribution to the spectrum although one shall expect the dipole mode ($m$=1) is also there. While for the thicker nanocables (in the scale of ~20 nm), multipole excitations besides dipolar excitation come into play, leading to the intensity increase of the transverse excitation, as compared with the longitudinal one.

### 6.3 optical absorption properties of the Si nanostructures of different geometrical configuration—from nanoparticle to nanocable of small and large diameters

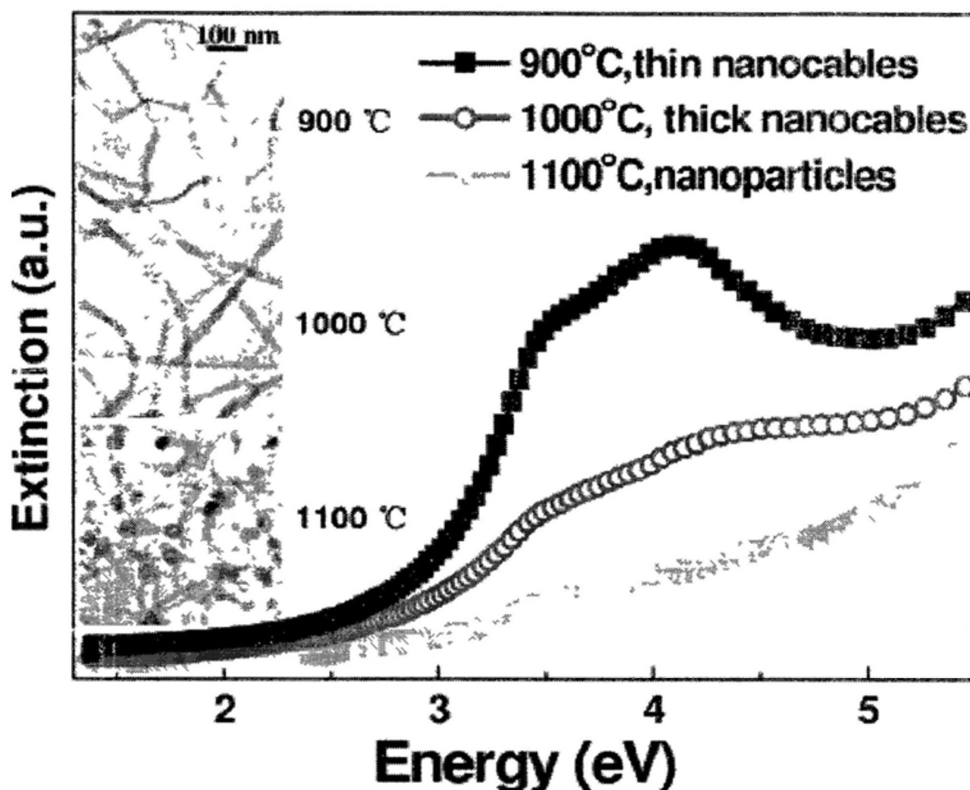


Fig 9.comparison of the optical extinction spectra among Si nanostructures of different geometrical configurations

When the morphology of the free standing Si/SiO2 core/shell nanostructures changed from spherical to cylindrical, we observed outstanding extinction modes appear in the near UV region (3-5 eV) through the optical study, the results are presented in Fig.9. The left hand side of the Fig.9 shows the low magnification TEM images of the three samples. The absorption of the nanoparticle (the bottom curve) continuously increases from 1.3 eV to 5.5 eV while no distinct feature is observed. In the case of the nanowires, an obvious absorption appears at 3-5 eV, and as the diameter decreases (the top curve), the intensity of the absorption band increases. This macroscopic feature in the extinction spectra of the Si nanostructures agrees well with

the EELS results.

## 6.4 Conclusion and discussion

In conclusion, the SP/IP excitations which depend on the aspect ratio of the $Si/SiO_2$ core/shell nanostructures have been investigated using EELS-related techniques under near parallel illuminations in STEM, making the results comparable to those obtained by optical methods. Elongation from a perfect spherical nanoparticle results in splitting of the SP/IP modes into a transverse and a longitudinal branch. Retardation effect comes into affect in longer nanostructures such as nanowires or nanorods, and the corresponding charge distribution in such nanostructure is revealed by the uniform intensity distribution along the longitudinal direction of the long nanocable in the EFTEM images. Simulations are also carried out by considering the cylindrical configuration, the size of the Si core in the Si/SiO2 nanowire determines the intensity ratio (transverse/longitudinal) of the SP/IP modes. All these understanding provide important guidance to the tuning of SP/IP in nanostructures by control their size and aspect ratio.

# Chapter 7. Interface Plasmon in Interacting Si Nanoparticle Chains

In the previous chapter, we have studied the effect of geometrical configuration on the plasmonic properties of individual Si nanostructures. In particular, we found the surface charge redistribution resulted from the nanostructure shape change (from spheroid to nanorod and nanowire) would lead to splitting of the interface Plasmon into transverse and longitudinal polarizations, the weight of the which in the overall plasmon oscillation also depends on the geometrical configuration. .

When the individual nanostructures are organized together in a specific manner (such as forming nanoparticle chains), one would expect possible interactions among the particles[57,59,61,80]. It is easy to image that such interaction would affect the surface charge distribution, and consequently affect the plasmonic behavior of the interacting system.

In this chapter, we have investigated the plasmonic behavior of one-dimensional Si nanoparticle chains, in which slightly elongated Si nanoparticles (nano-ellipsoids) are aligned in $SiO_2$ nanowires with different particle-particle separation distance. By employing the technique of EFTEM imaging, the spatial distribution and possible

interaction of different SP/IP modes have be visualized, disclosing the local field enhancement as a result of the coupling effect. The absorption properties of the nanoparticle chains are explained, which is found to directly correlate to the plasmonic behavior of the nanostructures.

### 7.1 Sample preparation and experimental setup

The Si nanoparticle chains were synthesized via thermal evaporation of SiO powder in a high temperature vacuum tube furnace[81]. Pure Ar gas was introduced as the carrier gas, and the total pressure of the system was kept at 200 mbar for the whole fabrication process. The source material was heated up to 1300℃ for 2hrs before the tube furnace was eventually cooled down to room temperature, and the products were collected at the temperature zone of ~1000℃ in the downstream of the tube furnace. A higher processing pressure at ~300 mbar leads to the formation of other forms of Si nanostructures, i.e., Si nanowires (being collected at 900-1000℃ temperature zone), and well separated Si nanoparticles (being collected at 1100℃ temperature zone)[20]. The products were annealed at 700℃ in oxygen atmosphere for 20 minutes before taking out from the tube furnace. In the present study, we have investigated the SP/IP excitations in the Si nanoparticle chains, in which the Si nanoparticles are ~12 nm in diameter, and they are assembled into one-dimensional chain-like structure by embedding in $SiO_2$. The separation distance between individual particles is in the range of several to several tens of nanometers. In order to make comparison, different Si nanoparticles chain with different inter-particle

separations was used in the experiments, for example ~30 nm, ~20 nm, ~10 nm and ~ 0 nm.

The morphology and microstructure of the products were characterized using a TEM, (Tecnai G2) with a GIF, (Tridiem$^{TM}$) attached to it. SREELS spectra were acquired in the STEM line scan mode with the electron probe size of ~0.5 nm and ~0.5 eV energy resolution. The EFTEM images were taken using a 2 eV slit centered at specific energy positions of interest. The optical extinction spectra of all the products (dispersed in ethanol) are measured using a UV-VIS spectrometer (Hitachi spectrophotometer U-3501).

### 7.2 EEL spectrum in the Si chain nanostructures with different particle distances

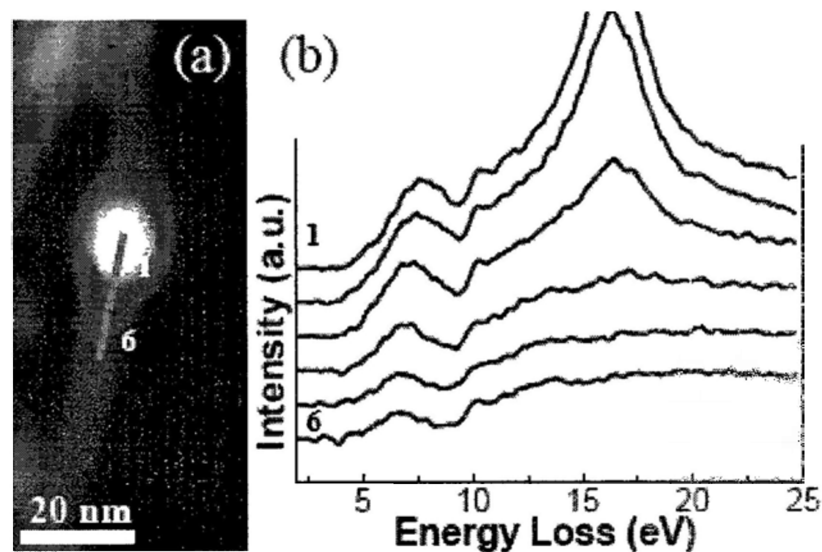


Fig. 1 (a) EFTEM image of an isolated Si particle embedded in a $SiO_2$ nanowire; (b) the corresponding EELS line scan spectra starting from the particle centre to the $SiO_2$ matrix wire along the chain axial direction.

We start our discussion with an isolated Si nanoparticle firstly. Fig. 1(a) shows the EFTEM image (using a 2 eV slit centered at the Si bulk plasmon resonance ~16.9 eV) of a spheroid nanoparticle with ~12 nm diameter, embedded in the wire-like $SiO_2$ matrix. A slight elongation of the spheroid is observed along the wire's axial direction, and the surface oxide thickness is ~3 nm. EELS line scan has been taken across the nanoparticle along the wire's axial direction (as marked by the red line in Fig. 1(a). Si bulk plasmon at ~16.9 eV dominates the EEL spectra (Fig. 1(b)) with a weak peak appearing at ~7.8 eV, when the electron probe is located on the nanoparticle. The intensity of the Si bulk plasmon peak drastically decreases when the electron probe moves away from the particle and spectrum features being characteristic of $SiO_2$ become obvious. At the same time, a slight red shift of the ~7.8 eV peak occurs.

The ~7.8 eV peak is commonly understood as the surface/interface plasmon arising from the Si surface surrounded by $SiO_2$ medium, similar to the situation in Chapter 5. In spherical particles with diameter below 100 nm, the oscillation frequency of the surface/interface plasmon can be generally estimated using point dipole approximation. Although the SP/IP excitation energy is expected to change with the size of the particles, such effect is rather weak for particle diameter <100nm[11]. The shape deviation from a perfect spheroid to ellipsoid could have more profound effect, i.e., a splitting in the SPR energy would occur, with one appearing at higher energy, and the other at lower energy, corresponding respectively to the transverse and longitudinal polarization of the surface plasmon[8], which has been

discussed in the last chapter. However, the energy difference between the two split peaks would also be fairly small for a slightly elongated spheroid[74]—such as the one shown in Fig.2. Consequently, it would be difficult to identify two distinct peaks (transverse and longitudinal modes) in the EEL spectra (as limited by the energy resolution and the signal to noise ratio of the technique) taken on such Si nanoparticle, but observe a "red-shift" of the SPR when the electron probe moves aloof the nanoparticle along the chain axial direction[82].

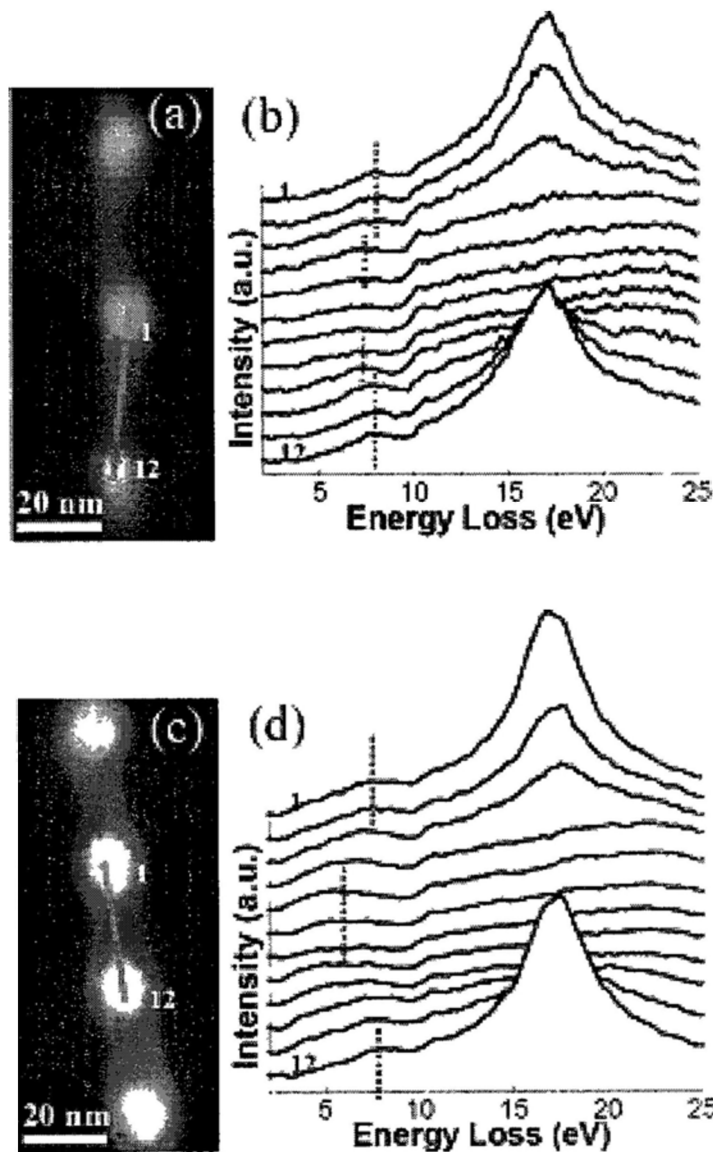

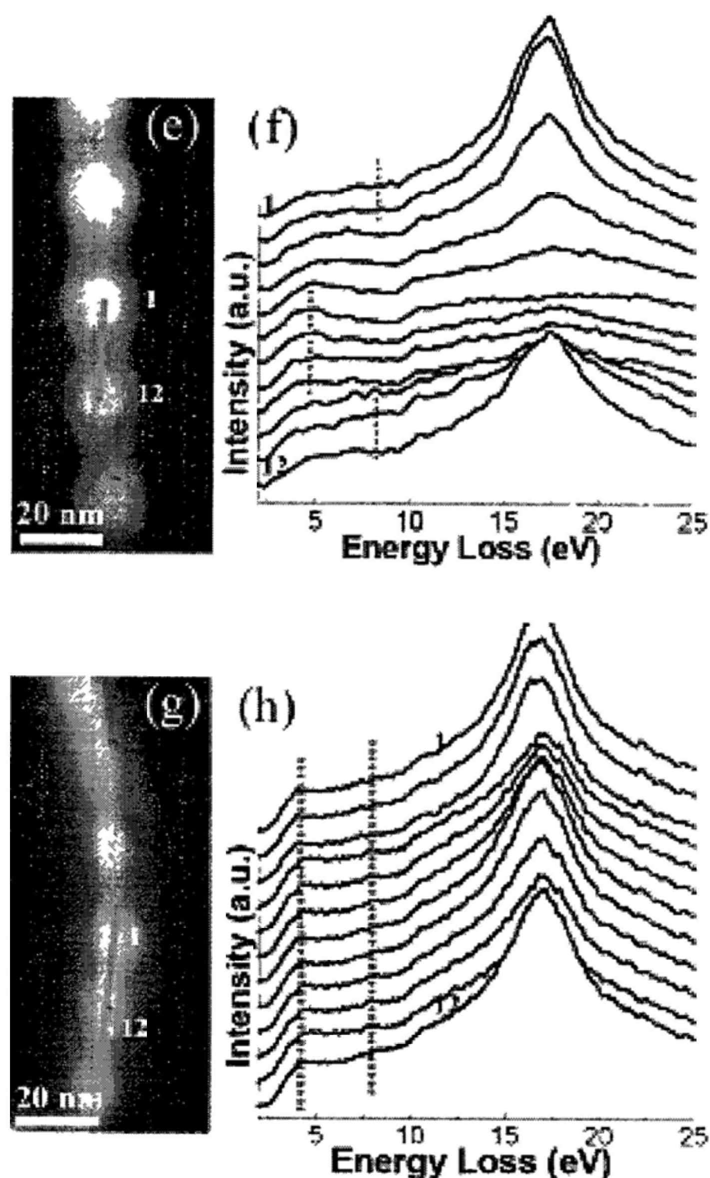


Fig. 2 EFTEM images of particle chains with different inter-particle spacing,(a) ~30 nm, (c) ~20 nm, (e) ~10 nm and (g) ~ 0 nm; (b) (d) (f) and (h) are the corresponding EELS line scan spectra taken across the Si particles along the chain axial direction.

The electron probe then scans across multiple nanoparticles with inter-particle separation of ~30 nm, which is shown in Fig. 2(a) (the inter-particle separation is defined as from edge to edge). The diameter of the Si nanoparticles in the chain and its surface oxide thickness are similar to those of the isolated Si

nanoparticle in Fig. 2(a). The SPR peak is observed to red shift from ~7.8 eV to ~6.7 eV when the electron probe moves from the center of the Si nanoparticle to the $SiO_2$ connection wire, with the SPR intensity significantly weakened in the middel of two particles. This red shift is only slightly larger than that in isolated particles. However, distinct difference in the EEL spectra is observed with inter-particle separation reduces to ~20 nm in Fig 2(c). When the electron probe is located on the Si nanoparticle, the SPR appears at ~8 eV, but with a plateau-like shoulder intensity extending to ~5.5 eV. As the e-probe scans away from the nanoparticle, a decrease in the ~8 eV peak intensity is observed simultaneously with an increase in the ~5.5 eV one (Fig. 2(d)). Similar trend is observed in the particle chain with shorter inter-particle spacing (i.e., ~10 nm in Fig. 2(e)), but with one peak occurring at slightly higher energy, i.e., ~ 8.1 eV (as compared to 8 eV), and the other at even lower energy, i.e., 4.8 eV (as compared to 5.5 eV) in Fig.2(f). In the extreme case, i.e., the Si nanoparticles are about to touch/touching each other in the chain, forming continurious wire-like morphology (Fig.2(g)), little variation is observed in the EEL spectra as the e-probe scans to different position on the chain. A low energy peak at ~4.2 eV is constantly observed in all of the spectra, while another weak furure can be barely discerned at ~8.2 eV.

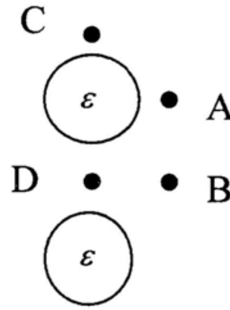


Fig.3 electron trajectories in the bispherical system

The chain structure is assumed to consist of nanoparticles aligned closed with small gaps between them. Based on the works done by Schmeits and Dambly, Zabala and Echenique Ruppin[57,59,61,80], the surface/interface plasmon excitations eigenenergies in this bispherical system correspond to the ratio of $x=r/d$ sensitively, $r$ is the sphere radius and $d$ is the distance between the centers of the two spheres, here we assume the two spheres have the same size ($x$=0 indicates the isolated sphere, while $x$=0.5 indicates the touching of the two spheres). The configurations of the fast incident electron in the bispherical system can be divided into 4 cases, which is indicated in the Fig.3. In different electron incident configurations, different SP/IP modes will be excited which will result in the different dominant peak.

In this section, EELS line-scan mode was adopted, case C and D are involved in the analysis of the excitation modes. The ratios of $x=r/d$ are 0.15 in Fig.3(a), 0.20 in Fig.3(c), 0.30 in Fig.3(e) and 0.45 in Fig.3(g). When the x-ratio is not big, for example in Fig.3(a) and Fig.3(c), the coupling is not so significant,

thus the dipolar-like surface/interface induced charge distribution dominates,which is ~9.5 eV for silicon. While in Chapter 5 we have seen the Silica oxidation layer will reduce the SP/IP energy. Considerting the energy resolution (~0.5 eV) of the STEM we used, the ~8 eV features in Fig.3(a) and (c) can be atrribtue to this.

On the other hand, the coupling of the excitation between two spheres leads to the lower energy peaks around ~ 5 eV, which corresponds to the two distorted dipoles. Since the coupling is sensitive to the $x$-ratio in the bispherical system, the relative inensity in Fig.3(a) and (c) is very weak. For the cases of the higher $x$ ratio, there will be lots excitations in the enery region 8 eV-10 eV. But due to the relative proximity of the SP/IP eigen-energies, the losses features cannot be resolved and yield a relative intense loss feature at ~8 eV.

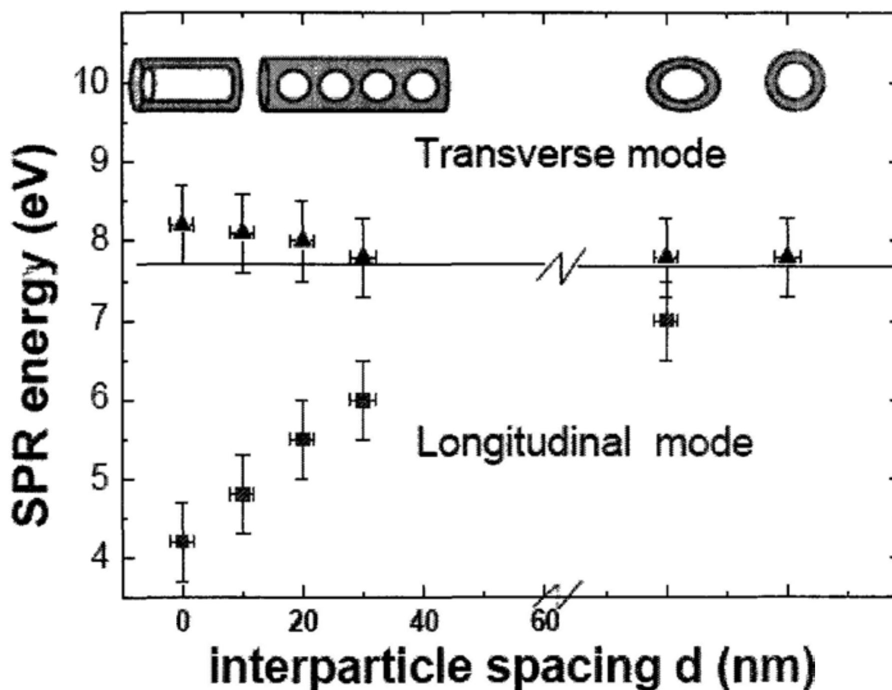


Fig. 4 The SP/IP energy as a function of the inter-particle separation, measured from experimental EEL spectra of different particle chains and isolated particles

The general effect of the interaction between close spheres is the splitting of the interface plasmon peak into two peaks at a lower and a higher energy, which is similar to the observation in chapter 6, i.e., the SP/IP modes would split into two polarizations along transverse and longitudinal direction as a result of the surface charge re-distribution. Fig.4 plots the experimental SPR data as a function of the inter-particle separation, with the error bar being determined by the energy resolution of EELS, i.e., 0.5 eV. Intuitively, when the nanoparticles are far apart from each other, they can be treated as isolated particles. On the other hand, when the nanoparticles in the chain are getting closer and closer, eventually a continuous thin nanowire would be formed. We therefore include data taken from both the single isolated Si nanoparticles and the thin Si nanowire as the two ends in such a plot.

When the inter-particle separation gets shorter and shorter, a blue shift and a red shift have been observed respectively in the high and low energy SPR branches, until ~8.2 eV, and ~4.2 eV are reached in the case of thin nanowire, corresponding respectively to the multipole and monopole modes of the SP/IP resonance in the nanowire.

The observed splitting for SP/IP excitation is a piece of direct evidence of the dipolar interactions between adjacent particles[83]. In such a model, the nanoparticles in the chain can be treated as an assembly of interacting dipoles, and the interactions between the particles can align the dipole fields forming collective dipole oscillations in the particle chain. When the nanoparticles are getting closer to each other, a

continuously change in the charge distributions on the particle chain would occur as mediated by the interaction of dipole fields on neighboring particles[57,61,84]. The Coulomb force interactions between the electrons in neighboring particles would then cause a blue-shift for polarization perpendicular to the chain axis (the high energy branch in the split SP/IP excitation modes, corresponding to the transverse SP/IP mode), and a red-shift for the longitudinal polarization (the low energy branch in the split SP/IP excitation modes)[85]. This is consistent with our experimental observations summarized in Fig.4.

### 7.3 spatial distribution of the SP/IP excitations in the Si nanoparticle chains

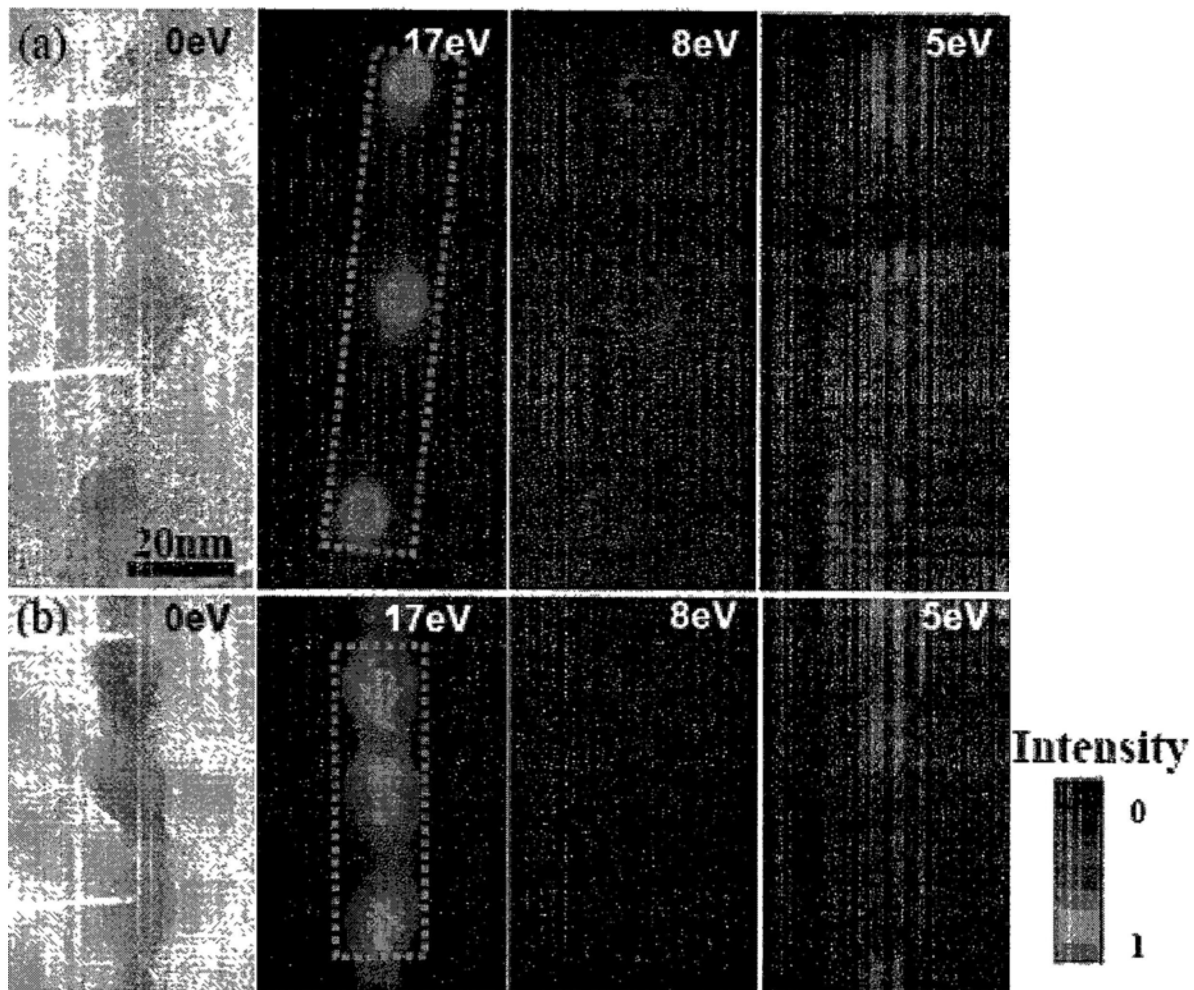


Fig. 5. (a) and (b): EFTEM images of two particle chains with different inter-particle spacing: ~30 nm and ~10 nm, imaged at energy losses of 0 eV, 17 eV, 8 eV and 5 eV using a 2 eV width slit;

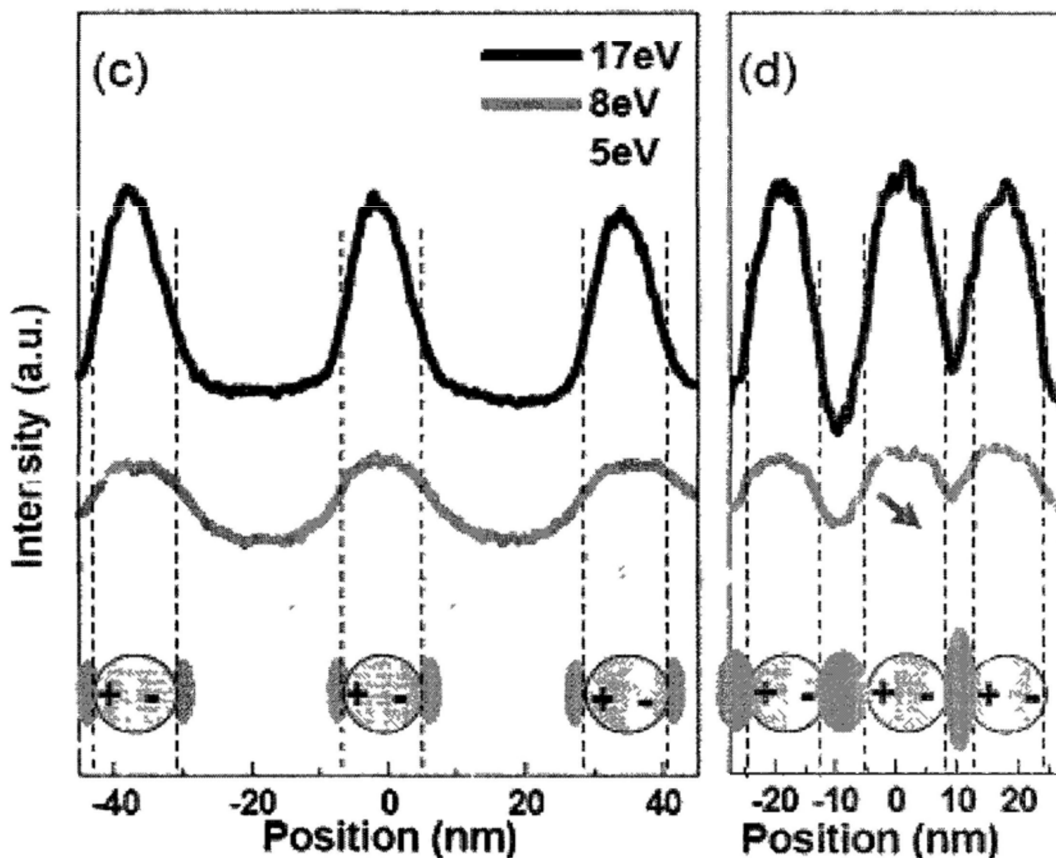


Fig. 5. (c) and (d) the intensity profiles retracted along the longitudinal directions of the two Si nanoparticle chains.

The interactions between the particles can be directly visualized in the energy filtered TEM (EFTEM) images of the Si nanoparticle chains taken at specific energy losses. Fig. 5 compares the EFTEM images of two different Si nanoparticle chains (with inter-particle separation of (a) ~30 nm, and (b) ~10 nm, respectively) taken at 0 eV (corresponding to bright filed TEM image), 17 eV (Si bulk plasmon resonance), 8 eV (transverse mode SPR), and 5 eV (longitudinal mode SPR). To obtain more straight-forward comparison of different plasmon mode intensity vs. their spatial distribution, the intensity profiles of the 17 eV, 8 eV, and 5 eV maps are retracted

along the longitudinal direction of the nanoparticle chain (as marked by the rectangular boxes in the corresponding maps), and are plotted in Fig. 5(c) and (d).

One can see that for both particle chains alike, the Si bulk plasmon is highly localized in the Si nanoparticles, while the 8 eV SP/IP mode is mainly confined to the spherical interface between the Si nanoparticle and $SiO_2$ interface layer. As a comparison, the spatial distribution of the 5 eV SP/IP mode is very different—although still locates on the spherical interface between Si and $SiO_2$, stronger intensity is found on both edges of the Si particles along the chain axial direction. When the nanoparticles are very close together (~5 nm interparticle separation, as marked by the arrow in Fig. 5(d)), the strongest intensity moves to in-between two adjacent nanoparticles, rather than locates on the Si particle surface, confirming the greatly enhanced field between the particles—another indication of the coupling. One of the major differences between the ~8 eV (transverse polarization) and the ~5 eV (longitudinal polarization) is their electron impact parameter, with the latter being much longer than the former along the axial direction of the particle chain[72]. Consequently, the dipolar interactions between the nanoparticle would exert stronger effect on the longitudinal mode of SP/IP (including the obvious red-shift in the SP/IP energy and its spatial re-distribution of intensity), but weaker effect on the transverse mode of SP/IP (small blue shift in the SP/IP energy).

## 7.4 Absorption property of the nanoparticle chain

The interaction between the nanoparticles in the chain would result in distinct character in their absorption properties. By controlling the fabrication of Si nanostructure samples into three different morphologies, i.e., well separated Si nanoparticles connected by $SiO_2$ nanowire, periodically distributed Si nanoparticles in the $SiO_2$ nanowire (i.e., the nanoparticle chains with inter-particle separation of 20±15 nm), and $Si/SiO_2$ core-shell nanocables, one can manipulate the optical property of such material.

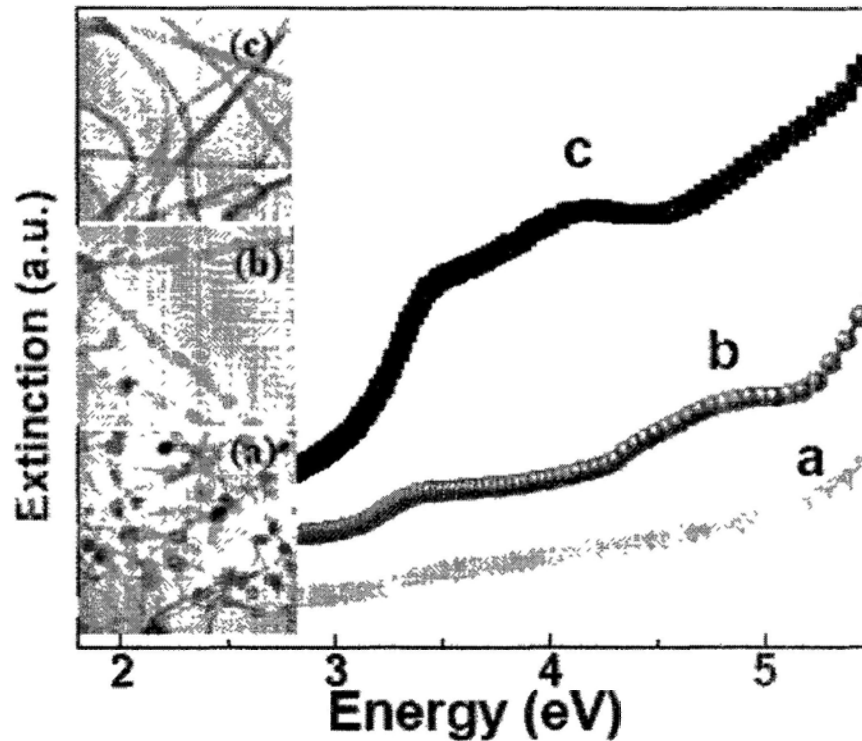


Fig. 6. The low magnification TEM images and the optical extinction spectra of (a) well separated Si nanoparticles (connected by $SiO_2$ nanowire), (b) nanoparticle chains with inter-particle separation of 20±15 nm, and (c) $Si/SiO_2$ core-shell nanocables.

Fig.6 shows the optical extinction spectra and corresponding bright field (BF)

TEM images of these three products. While there is no distinct feature presenting in the extinction spectrum of well separated Si particles (sample a), a broad extinction band centered at ~5 eV is observed above the 3.4 eV excitation threshold of Si for the nanoparticle chains (sample b). Similar extinction band has also been revealed in the $Si/SiO_2$ core-shell nanocables (sample c), but at lower energy of ~4.2 eV.

One shall note that absorption measurement was performed on macroscopic scale, so that the extinction spectrum would represent the average behavior of the nanoparticle chain with different inter-particle separation (ranging from 5 to 35 nm). Finer control over the inter-particle separation during growth is currently attracting much more investigation and research. In addition, the SPR modes in individuc Si nanotrusture are essentially broader than those in metals, as the imaginary part of the dielectric function of Si is large. This suggests that Si may be less competetative to metals, such as Au, in the applications of waveguides and sensors.

### 7.5 Conclusions

In conclusion, the surface plasmon resonance in closely packed one-dimensional Si nanoparticle assemblies has been directly visualized using EELS and EFTEM imaging, which techniques enjoy spatial resolution down to nanometer scale. Near-field interactions between the adjacent nanoparticle result in splitting of the surface plasmon resonance into transverse and longitudinal

polarizations with different spatial distributions. In particular, spatial re-distribution and enhancement of the longitudinal mode SPR intensity are observed to occur when the inter-particle separation is very short (in our case the distance is shorter than 10 nm). The experimental observation suggest possible tuning of the surface plasmons and local electromagnetic field enhancement by adjusting the interparticle separation in the 1D particle chain, which may find promising applications in functional UV optical devices below the diffraction limit of light.

# Chapter 8. Conclusion

In this thesis study, the plasmonic properties of Si nanostructures with different geometrical configurations are investigated by both experiments and theoretical simulations. The theoretical solutions are based on the classical dielectric theory and the mainly experimental techniques include STEM line-scan EELS, SREELS spectrum image and EFTEM imaging.

The planar boundary was considered in a wedge shape Si specimen, and the spectrum image is obtained from such a sample. It can be concluded that the SP/IP excitation modes depends not only on the impact parameter of the electron, but also on the thickness of the specimen, a general consistency between the experimental results and simulation ones appeared only when the relativistic correction is adopted.

We then examined Si nanoparticles, in which the interface changes into a spherical configuration. We have employed two series of samples. In the first series, the specimen had similar Si core size, while the thickness of the oxidation shell varied; in the second set, the specimens had similar shell thickness while the size of the Si core changed. The experiments results showed that the spherical system associates with an IP at ~7 eV, which red shift obviously only when the thickness of the

oxidation shell increases. Such a red shift eventually levels off when the shell is thick enough (in the experiments the shell thickness is more than 5 nm in sample set 2). A reasonable consistency is found between the experimental and the simulated results given that the imperfect shape of the specimen is not taken into consideration in the simulation. When the core size of the Si nanoparticle increases, the multipolar excitations contribute to the broadening of the IP peak rather than red-shift. As a comparison, when the thickness of the $SiO_2$ shell increases, the depolarization filed will reduce the restoring force of the multipolar excitation, thus the plasmon eigen-energy will red shift to lower energy. Nevertheless, as the shell thickness becomes larger than the interaction distance of the depolarization filed around the particle, the plasmon excitation energy will level off a constant value while the intensity will decrease greatly.

As the nanoparticle is elongated along one direction, the nanorod or nanowire can be obtained, in which the spherical interface evolutes to cylindrical interface. We consequently investigated specimens starting with isolated nanoparticles to nanorods and to nanowires. The IP of elongated nanostructures split into two branches with one located at lower energy range and the other at higher energy range. The lower energy excitation mode results from the longitudinal polarization while the higher one from the transverse polarization. This can be explained by the specific charge distributions on a cylindrical surface/interface. We have also found that the intensity ratio of the two IP modes can be modulated by vary the diameter of the Si core in the case of long nanowire, which is resulted from change of contribution from different modes as the

nanowire diameter varies.

With the understanding obtained from the isolated Si nanostructures, we then focus on the plasmon excitation in interacting nanoparticle chain. In the chain system the Si nanoparticles are connected by amorphous $SiO_2$ wire. The nanoparticle chains have different separation distance between the adjacent nanoparticles. The local field enhancement of the longitudinal IP excitation between the two adjacent particles can be clearly observed. This is resulted from the charge re-distribution on the Si nanoparticles when the inter-particle distance is small—a direct consequence of the interparticle coupling.

# Bibliography

[1] C.Kittel, Introduction to Solid State Physics, $8^{th}$ edition, Wiley Press, 2005

[2] H. Raether, Excitation of Plamsons and Interband Transitions by Electrons, Springer-Verlag, 1980

[3] H. Raether, Surface plasmons on smooth and rough surfaces and on gratings, Springer-Verlag, 1988

[4] R.F.Egerton, Electron Energy-Loss Spectroscopy in the Electron Microscope, $2^{nd}$ edition, Plenum Press, 1996

[5] R.H.Ritchie, Phys. Rev, 106, 874 (1957)

[6] J.A.Stratton, Electromagnetic Theory, $1^{st}$ edition, McGRAW-Hill, 1941

[7] S.A.Maier, P.G.Kik, H.A.Atwater, etc. Nature, 2, 229 (2003)

[8] Y.N.Xia, N.J.Halas, etc. MRS Bulletin, 30, 338 (2005)

[9] W.L.Barnes, A.Dereux, T.W.Ebbesen, Nature, 424, 824 (2003)

[10] S.A.Maier, H.A.Atwater. J.Appl.Phy. 98, 011101 (2005)

[11] Mie, Ann.Physik, 25, 377 (1908)

[12] Gans. Ann.Physik, 352, 270 (1915)

[13] P.Mulvaney, Langmuir, 12, 788 (1996)

[14] S.Link, M.A.El-Sayed, J.Phys.Chem.B, 103, 8410, (1999)

[15] K.L.Kelly, E.Coronado, L.L.Zhao etc. J.Phys.Chem.B, 107, 668 (2003)

[16] J.E.Rowe, H.Ibach, Phys.Rev.Lett. 31, 102 (1973)

[17] D.Ugarte, C.Colliex, P.Trebbia, Phys.Rev.B. 45,4332 (1992)

[18] B.W.Reed, J.M.Chen, N.C.MacDonald, etc. Phys.Rev.B. 60, 5641 (1999)

[19] J.Kikkawa, S. Takeda, Phys.Rev.B, 75, 245317 (2007)

[20] J.Wang, X.J.Wang, Y.Jiao, etc. Appl.Phys.Lett, 95, 133102 (2009)

[21] Y.Cui, C.M.Lieber, Science, 291,851 (2001)

[22] X.F.Duan, Y.Huang, Y.Cui, etc. Nature, 209, 66 (2001)

[23] T.Stelzner, M.Pietsch, G.Andra, etc. Nanotechnology, 19, 295203 (2008)

[24] D.B.Williams, C.B.Carter, Transmission Electron Microscopy: A Textbook for Material Science, Plenum Press, 1996

[25] Z.L. Wang, Micron, 27, 265 (1996)

[26] L.Yang, C.D.Spataru, S.G.Louie, etc. Phys.Rev.B. 75, 201304, (2007)

[27] J.D.Hlomes, K.P.Johnston, R.C.Doty, etc. Science, 287, 1471 (2000)

[28] J.Lindhard, Dan.Vidensk.Selsk.Mat.Fys.Medd, 28, 1 (1954)

[29] E.D.Palik, Handbook of Optical Constants of Solids, Academic Press, 1985

[30] P.M.Echenique,A. Howie and D.J.Wheatley, Philos.Mag.B 56,335 (1987)

[31] T.L.Ferrel, P.M.Echenique, Phys.Rev.Lett. 55, 1526 (1985)

[32] F.J.Abajo, Phys.Rev.Lett 59,3095 (1999)

[33] F.J.Abajo, Phys. Rev.B 60,6086 (1999)

[34] R.H.Ritchie, A.Howie, Phil.Mag.A. 58,753 (1988)

[35] Z.L.Wang, Elastic and Inelastic Scattering in Electron Diffraction and Imaging, Plenum Press, 1995

[36] K.Kutsuki, T.Ono, K.Hirose, Sci.Tech.Adv.Mat. 8, 204 (2007)

[37] E.Hutter, J.Fendler, adv.mat. 16, 1685, 2004

[38] P.M.Echenique, J.B.Pendry, J.Phys.C 8, 2936 (1975)

[39] J.M.Cowley, Surf.Sci. 114, 587 (1982)

[40] M.Kociak, O.Stephan, Phys.Rev.Lett, 87, 075501, (2001)

[41] M.Kociak, L.Henrard, Phys.Rev.B, 61, 13936 (2000)

[42] O.Stephan, Appl.Phys.A: Mater.Sci.Process. 67,107 (1998)

[43] A.Loiseau. Phys.Rev.Lett 76,4737 (1996)

[44] R.Tenne, L.Margulis, Nature, 360,444 (1992)

[45] M.Couillard, A.Yurtsever, D.A.Muller, Phys.Rev.B, 77, 085318 (2008)

[46] Corrado Spinella, Corrado Bongiorno, Appl.Phys.Lett, 87, 044102 (2005)

[47] F.Neyer, P.Schattschneider, J.Microscopy 187, 184 (1997)

[48] P.E.Batson, Phys.Rrev.Lett, 49, 936, (1982)

[49] P.E.Batson, Surf.Sci. 156, 720 (1985)

[50] P.E.Batson, Ultramicroscopy 9,277 (1982)

[51] T.L.Ferrel, R.J.Warmack, Phys.Rev.B, 35, 7365 (1987)

[52] G.F.Bertsch, H. Esbensen, B.W. Reed, Phys.Rev.B, 58, 14031, (1998)

[53] P.Moreau, N.Brun, C.Colliex, A.Howie, Phys.Rev.B, 56, 6774, (1997)

[54] R.G.Molina, A.G.Marti, A.Howie, R.H.Ritchie, J.Phys.C, 18, 5335 (1985)

[55] F.J.Abajo, Phys.Rev.B, 60, 6103, (1999)

[56] F.J.Abajo, Phys.Rev.L, 80, 5180, (1998)

[57] N.Zabala, A.Rivacoba, P.M.Echenique, Phys.Rev.B, 56, 7623 (1997)

[58] M.Schmeits, Phys.Rev.B, 39, 7567, (1989)

[59] R.Ruppin, Phys.Rev.B, 26, 3440 (1982)

[60] C.K.Malu, F.J.Clares, Nanotechnology, 19, 285713, (2008)

[61] M.Schmeits, L.Dambly, Phys.Rev.B, 44, 12706, (1991)

[62] J.B.Neaton, D.A.Muller, N.W.Ashcroft, Phys.Rev.L, 85, 1298, (2000)

[63] L.Henrard, O.Stephan, etc. J.Elec.Spec.Rela.Phen, 114, 219, (2001)

[64] Fuzi Yang, J.R. sambles, Phys.Rev.L, 64, 559, (1990)

[65] Jeanguillaume, C. Colliex, Ultramicroscopy 28,252(1989)

[66] J.N.Anker, W.P.Hall, O.Lyandres, etc. Nature Materials, 7,442 (2008)

[67] N.Bonnet, N.Brun, C.Colliex, ultramicroscopy, 77, 97(1999)

[68] K.Kimoto,S.Isakozawa, etc. jounal of electron microscopy 50, 523 (2001)

[69] K.Kimoto, T.Sekiguchi, T.Aoyama, J.Electron Microscopy, 46, 369 (1997)

[70] T.Hanrath, B.A.Korgel, Nano Lett, 4,1455 (2004)

[71] A.Howie, R.H.Milne, Ultramicroscopy, 18,427 (1985)

[72] N.Zabala, E.Ogando, A.Rivacoba, etc. Phys.Rev.B. 64,205410 (2001)

[73] A.Rivacoba, P.Apell, N.Zabala, Nucl.Instrum.Methods Phys.Res.B. 96,465 (1995)

[74] C.F.Bohren, D.R.Huffman, Absorption and Scattering of Light by Small Particles, Wiley Press, 1998

[75] A.Ron, I.B.Goldberg, J.Stein, etc. Phys.Rev.A. 50, 1312 (1994)

[76] S.Link, M.B.Mohamed, M.A.El-Sayed, J.Phys.Chem.B, 103, 3073 (1999)

[77] C.Noguez, J.Phys.Chem.C, 111, 3806 (2007)

[78] B.Schaffer, U.Hohenester, A.Trugler, etc. Phys.Rev.B, 79, 041401R (2009)

[79] J.Nelayah, M.Kociak, O.Stephan, etc. Nature Physics, 3, 348 (2007)

[80] S.J.Norton, T.Vo-Dinh, J.Opt.Soc.Am.A, 25, 2767 (2008)

[81] Q.Li, Y.Jiao, Appl.Phys.Lett, 87,261905 (2005)

[82] M.Bosman, V.J.Keast, M.Watanabe, etc. Nanotech, 18, 165505, 2007

[83] J.R.krenn, A.Dereux, J.C.Weeber, etc. Phys.Rev.Lett. 82,2590 (1999)

[84] U.Hohenester, J.R.Krenn, Phys.Rev.B. 72,195429 (2005)

[85] S.A.Maier, Plasmonics :Fundimentals and Applications, Springer, 2007

[86] Garcia-Molina, R. Gras-Marti, A. Howie, Ritchie, R.H, J.Phys.C. Solid State Physics, 18, 5335, 1985

[87] C.Sonnichsen, T.Franzl, T.Wilk, G.Von Plessen, J.Feldmann, Phys.Rev.Lett. 18, 077402 (2002)

[88] C.Sonnichsen, T.Franzl, T.Wilk, G.Von Plessen, J.Feldmann, New Jounal of Phys. 4, 93.1 (2002)

[89] T.Klar, M.Perner, S.Grosse, G.Von Plessen, W.Spirkl, J.Feldmann, Phys.Rev.Lett, 80, 4249 (2998)s

[90] N.Yao, Z.L.Wang, Handbook of Microscopy for Nanotechnology, Volume II, TsingHua Press, 2005

[91] J.Wang, Phd. Dissertation, Application of Valence Electron Energy Loss Spectroscopy in Low dimensional Nanostructured Materials, 2007